Clemson University

TigerPrints

All Dissertations

Dissertations

12-2010

PACKET ERROR RATE PREDICTIVE MODEL FOR SENSOR RADIOS ON FAST ROTATING STRUCTURES

Lei Tang
Clemson University, ltang@clemson.edu

PACKET ERROR RATE PREDICTIVE MODEL
FOR SENSOR RADIOS ON FAST ROTATING STRUCTURES

_____

A Dissertation
Presented to
the Graduate School of
Clemson University

_____

In Partial Fulfillment
of the Requirements for the Degree
Doctor of Philosophy
Mechanical Engineering

_____

by
Lei Tang
December 2010

_____

Accepted by:
Dr. Yong Huang, Committee Co-Chair
Dr. Kuang-Ching Wang, Committee Co-Chair
Dr. L. Wilson Pearson
Dr. Thomas R. Kurfess

Abstract

Wireless sensing technologies have raised widespread interests in the applications for monitoring fast rotating or moving machinery structures in manufacturing environments. Over the past five years, a few wireless sensor systems have been implemented and proven to feasibly work under fast rotation conditions. However, few of these studies evaluated data transmission performance of the wireless communication systems. Although the manufacturing environments are known to be harsh for wireless communication, in many cases, an excellent data throughput is critical for such systems. Conventional statistical methods for studying wireless communication channels are not sufficient in this specific field.

This dissertation presents systematic experiments to understand and characterize the behavior of a 2.4 GHz band wireless channel between a fast rotating transmitter and a stationary data receiver. The experiments prove, in manufacturing machines, multipath propagation induced by metallic objects causes high power attenuation of radio signals during transmitter motion, and the consequence, low received signal power, is recognized as the major cause of transmission errors.

The dissertation proposes a deterministic packet error rate (PER) predictive model for rotating wireless measuring systems using IEEE 802.15.4 sensor radios. The model consists of three sub-models that predict power attenuation, bit error rate (BER), and PER in three stages for given specifications regarding environment, radio transmission, and rotation. The dissertation provides experimental validation of the sub-models and discusses their limitations and prediction errors. By either experiments or simulations, two data transmission protocols, automatic

retransmission request (ARQ) method and online error avoidance algorithm, are proved efficient for a reliable wireless communication of such sensor radios.

As the first effort to characterize and model such radio channels, the dissertation provides in-depth understandings of the channels' fast varying behavior, achieves prediction guidance for the channels' communication performance, and introduces prospective transmission protocols for performance enhancement.

Dedication

To my parents and brother, for their unconditional love and support.

Acknowledgements

I would like to thank my advisors, Dr. Yong Huang and Dr. Kuang-Ching Wang, for their guidance and support throughout my graduate studies at Clemson. In the past few years, I have grown significantly both personally and academically, and I am extremely grateful for their commitment and patience. Their dedication and attention to my dissertation work resulted in profound improvements.

I would like to express my appreciation to Dr. L. Wilson Pearson for not only generously providing instruments and laboratory facilities but also offering guidance and technical support. I would like to thank Dr. Thomas R. Kurfess for his advice and support for this dissertation work. Dr. Fangming Gu at General Motors is also acknowledged for his advice.

Special thanks are given to great technicians in the Department of Mechanical Engineering at Clemson University: Michael Justice, Jamie Cole, and Stephen Bass. Without these gentlemen, my ideas would have never become real experimental equipments.

I also owe gratitude to Jobin Jacob, Dr. Yu Long, Dr. Xiaoyu Wang, Mason D. Morehead, and Kevin Foy for providing research support and sharing life experience. The same gratitude goes to Wei Wang, Yafu Lin, Jun Yin, Leigh Herran, and Changxue Xu for having a good time together.

Finally, I am grateful to my family and friends who stand behind me all the time. Their love and friendship have provided all inspiration, motivation, and direction in life.

Table of Contents

Table of Contents (Continued)

Table of Contents (Continued)

Table of Contents (Continued)

List of Tables

List of Figures

List of Figures (Continued)

List of Figures (Continued)

Chapter 1

Introduction and Research Motivation

1.1 Wireless Sensor Networks in Industrial Applications

As wireless technologies have advanced and succeeded in the past decades, the demands for their applications in modern industrial monitoring and control have arisen for their benefits of facilitating flexible communication [Lessard1988] [Brooks2001] [Ciadiello2005] [Willig2005]. Advances in integrated circuit manufacturing have made it economically efficient to incorporate sensors, controllers, and radios into one tiny sensor node. Integrating functions of sensing, computing, wireless transmission, data storage, and battery-based power supply, such wireless sensors can be placed at almost any location, including those that have been unreachable in the past due to wiring constraints or object mobility. The installation and maintenance costs can also be substantially reduced by avoiding the needs of cable deployment and replacement.

Wireless sensors installed on machines, vehicles, and other facilities in a factory floor act as filed devices and create a wireless sensor network (WSN) that can be seamlessly incorporated into factory monitoring and control infrastructures. Each of the field devices is responsible to monitor the facility's status as well as serve as the first stage of the processing hierarchy. The devices in a mesh network also can work as routers for messages from other devices, which not only extend the range of the network and increase reliability, but also make adding or moving field devices easy. The messages from the field devices are eventually sent into the higher

hierarchical level of the infrastructure through access points and gateways for process control, data storage and management. A few pilot explorations of the applications of wireless sensors on manufacturing process monitoring have been made to assess their feasibilities [Tiwari2004] [Sundararjan2005] [Ota2006] [Wright2008].
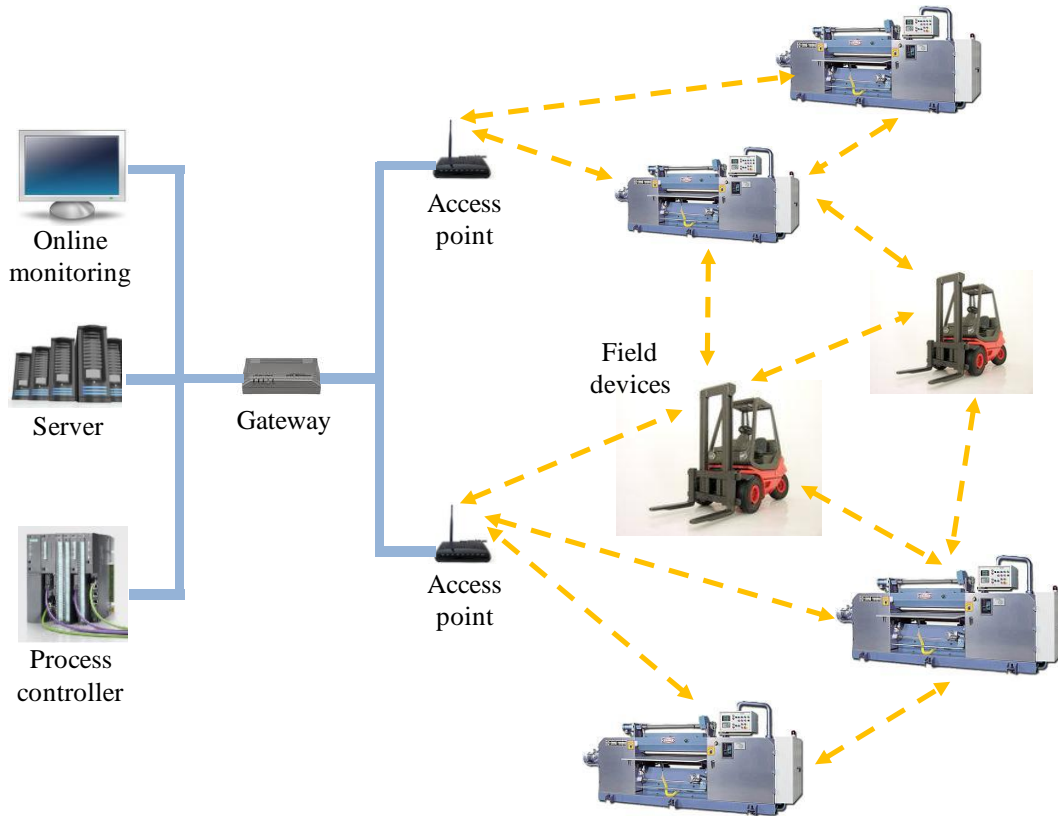
Figure 1.1: Structure of a mesh wireless sensor network for factory monitoring and control

IEEE 802.15.4 is the most widely adopted standard of today's commercial wireless personal area networks (WPANs) for low data rate, low power consumption, low complexity circuitry, and short range transmission. The standard specifies the overall characteristics of the physical (PHY) and medium access control (MAC) layers of WPANs [IEEE802.15.4]. Based on IEEE 802.15.4, a few organizations have released standards and specifications for WSNs, such as ZigBee [ZigBee], ISA100.11a [ISA], and WirelessHART [WirelessHART]. The ZigBee

specification defines application framework, device profile, network layer, and security services for the low-cost, low-power-consumption, two-way wireless communications in the applications of consumer electronics, home and building automation, industrial controls, PC peripherals, and medical sensors [Zigbee]. The ISA100.11a standard defines the protocol suite, system management, gateway, and security specifications; it provides reliable and secure wireless operation for non-critical monitoring, alerting, supervisory control, open loop control, and closed loop control applications [ISA]. The WirelessHART is a self-organizing and self-healing wireless mesh network communications protocol for process automation applications [WirelessHART].

Manufacturers such as *Crossbow* [Crossbow], *MicroStrain* [MicroStrain], *Ember* [Ember], *Dust Networks* [DustNetworks], and *MillenialNet* [MillenialNet] have offered standard-compatible wireless sensor networking platforms for applications of industrial monitoring and automation. Crossbow provides a large variety of wireless modules, sensor boards, gateways, and development kits for general purposes. MicroStain recently released tiny, passive wireless sensors that use an inductive link to receive power from an external coil and completely eliminate batteries for monitoring turbines and other high-speed rotating equipments.

Figure 1.2 illustrates four functional modules of a wireless sensor: sensing and data acquisition, control and processing, wireless communications, and power supply. Two approaches have been adopted for the design of the sensing and data acquisition module [Baronti2007]. The expandable approach, as pioneered by *Crossbow* [Crossbow], consists in developing sensor boards that can be attached to a main microprocessor board through an expansion bus, so that users can design their own sensor boards for specific applications. The other approach is to put sensors directly on the microcontroller board, and the examples are wireless strain node and wireless accelerometer node from *MicroStrain* [MicroStrain]. In many cases, the analog-to-digital converter (ADC) is embedded in the microprocessor, for example, the MICAz module from

Crossbow [MICAz]. In addition to these basic functional modules, wireless sensors may consist of flash memories and Input/Output (I/O) buses.
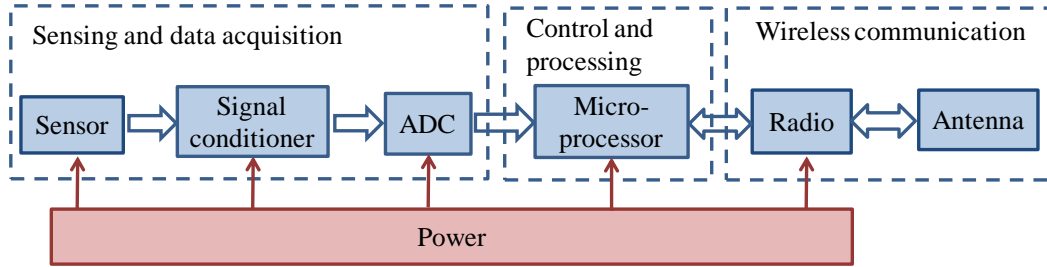
Figure 1.2: Function diagram of a wireless sensor

1.2   Wireless Sensor Systems for Monitoring Rotating Structures

Without the restriction of wires, wireless sensors are naturally advantageous for monitoring rotating structures that are commonly found in turbines, vehicles, and machining machines with substantial monitoring importance. Commercial wireless torque measurement systems have been available on market [Honeywell] [ATI]. In these systems, a rotary transformer is incorporated to transfer power to a loop antenna around the rotating shaft. As conventional transformers, the rotary transformer works on the radio-frequency induction theory [Honeywell]. The power is conditioned and excites the strain gages on the shaft. Then, the loop antenna sends measurement signals back to a stationary antenna through the transformer. However, a disadvantage of these systems is, the stationary antenna installation is highly restricted since the antenna gap is normally less than ¾ inch. In addition, the loop antennas are fixed size and less flexible for the usage on shafts of different diameters.

A few studies have performed pilot exploration to adopt well-developed wireless communication devices that are compatible with well-defined standards in the application. In [Miettien2002], Miettien *et al.* presented an operation monitoring system installed in a laboratory pilot roll for on-line monitoring of roll cover. The system measured the acoustic emission of the

4

rolling contact, the temperature of the polymer cover, and the temperature of the shell of the covered roll. The measurement signal was transferred from the rotating roll to a computer via an IEEE 802.11 wireless local area network (WLAN). Different from the IEEE 802.15.4 standard, the IEEE 802.11 standard was developed for more complex devices that are supported by higher power, for example, laptop computers for higher bandwidth network access.

In [Dzapo2004], a portable wireless measuring system for monitoring motor shaft torque, power and rotational speed was developed and tested on a ship motor. The system employed a *Radiometrix* TX2 module to convert voltage levels to frequency modulated (FM) RF signals [Radiometrix]. The data were transmitted over a low-power digital radio at 19200 bits per second (bps). The measurement uncertainty and errors were analyzed, while transmission errors in experiments have not been mentioned.

In [Sarkimaki2006], the researchers presented their work to determine the applicability of ZigBee technology to electric motor rotor measurements. A ZigBee-compatible wireless torque sensor was mounted and tested on an electric motor spindle. According to test results, data transmission from the rotating sensor worked well; errors in data transmission were small and data transfer speed of 400 bps was achieved.

1.3   Transmission Performance of Rotating Wireless Sensors

The performance of a wireless sensor system that users may concern includes two issues: measurement capability and data transmission capability. The first issue addresses measurement accuracy, precision, dynamic range, etc. The analysis methods for this issue have been well developed in theories of the measurement engineering. The latter issue concerns data reception or error rate of the wireless communication, which is crucial for the data throughput of the wireless

measurement system. This dissertation is focused on the latter issue, i.e., the wireless data transmission performance.

Recent work has been conducted to study data transmission performance of wireless sensors for different radio hardware and environments, such as offices, a tennis court, a parking area, forests, and industrial facilities [Lal2003] [Cerpa2003] [Reijers2004] [Werb2005]. Comprehensive sensor radio measurements have been performed at Clemson University to study transmission performance in the multipath environment of a representative university machine shop, and the measured results are presented in Appendix A. However, very little work has considered the situation of rotating sensor radios. Among the aforementioned applications of wireless sensors for rotating structure monitoring, only [Sarkimaki2006] conducted transmission performance experiments. In the experiments a sensor was rotating at tangential rotation speeds from 1.26 to 6.28 m/s and sending a series of 2-byte probe packets, and the communication performance was measured by counting the number of received probe packets. In the experiments, very few packets were lost, so the paper concluded that the rotation induced no significant communication errors.

These studies, however, have not considered high rotation speeds and high sensing data rates. For example, rotating structures in machines often achieve several thousand revolution per minute (rpm) rotation speed. For a rotor of 10 cm radius rotating at 2000 rpm, the equivalent linear velocity is about 21 m/s. [Wang2007] reported significant transmission errors of ZigBee-compatible wireless communication modules employed on a computer numerically controlled (CNC) lathe. When the rotating radio's tangential speed was tuned up to around 13.6 m/s, the radios observed a packet error rate (PER) above 0.11 in the experiments. This order of transmission error rate is high enough to significantly restrict the efficiency of the measuring system that requires high sensing data throughput. For example, vibration analysis for defect

6

diagnosis of rolling bearings requires measurement of up to 3000 Hz sampling rates [Orhan2006]. Hence, adoption of these wireless measuring systems requires more accurate characterization and assessment of data transmission performance.

1.4   Potential Causes of Rotating Sensor Radio Transmission Error

Rotating mechanical structures are usually located within confined enclosures, with the structures themselves and their surroundings made of metallic materials. To monitor such structures, a wireless measurement system must consist of two parts: a measuring and transmitting radio, which is mounted on or within the rotating structure, and a receiving radio, which is mounted on a stationary part near the rotating structure. Figure 1.3 gives a simplified structure diagram of such a wireless measuring system. To be consistent, throughout the dissertation, the rotating radio is always referred to as transmitter, and the stationary radio is referred to as receiver. We only consider the one-way communication link from the transmitter to the receiver, and the link performs data transmission without acknowledgements or re-transmissions.
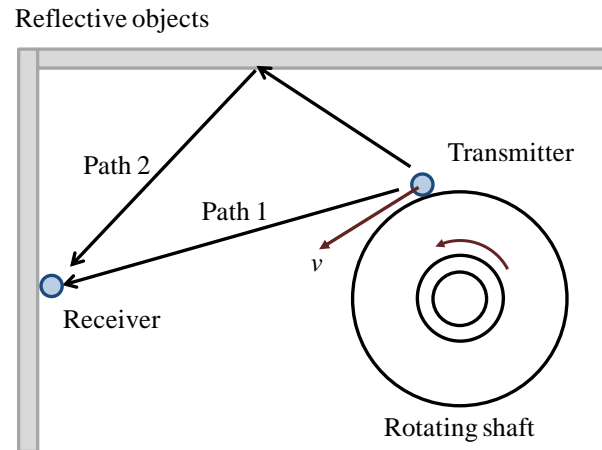
Figure 1.3: Structure of wireless measuring system for monitoring a rotating shaft

In [Willig2005], Willig *et al.* examined fundamental problems for wireless industrial communication systems to achieve reliable transmission and attributed transmission errors to multipath propagation, Doppler shift, interference from collocated wireless communication systems, and thermal and man-made noise. Multipath propagation affects the radio channel in two ways by causing, respectively, small-scale signal attenuation and inter-symbol interference (ISI). Additionally, in a high-speed rotation scenario, hardware reliability of the sensor radios is also a concern.

In this dissertation, signal power attenuation is recognized as the most significant factor for transmission performance of rotating sensor radios; other factors, such as ISI, Doppler shift, machine electro-magnetic noise, and hardware instability, are experimentally verified in Section 2.4 to have insignificant impacts under the dissertation studied conditions and hence will not be included for modeling transmission performance.

1.5 Dissertation Scope and Overview

The dissertation addresses the wireless transmission performance issue that fast rotating sensor radios may face in a machine environment. Specifically, the dissertation aims to provide an approach to model the signal propagation and predict the data transmission performance of such sensor radios. For this purpose, we introduce a PER predictive model.

The dissertation is organized as follows. Chapter 2 reviews related work on radio propagation modeling in industrial environments and data transmission characteristics of wireless sensors in various environments. Additionally, based on preliminary sensor radio experiments, the chapter analyzes the potential transmission error causes of fast rotating sensor radios. After identifying the major error causes, Chapter 3 introduces two hypotheses for the PER predictive model, and then the chapter proposes the model and its three sub-models. Chapter 4 presents the

design of model validation experiments conducted with sensor radios and a vector network analyzer (VNA). Based on these experiment data, the validation of the hypotheses and the sub-models is presented in Chapter 5. In Chapter 6, to enhance communication performance of such sensor radios, two data transmission protocols, automatic repeat request (ARQ)-based transmission method and online error avoidance algorithm, are presented and analyzed. The dissertation summarizes in Chapter 7 with suggestions on future work.

Chapter 2

Background and Related Work

Industrial monitoring and control systems require stringent reliability and timing, which are served well by mature wired fieldbus communication technologies such as Process Field Bus (PROFIBUS), World Factory Instrumentation Protocol (WorldFIP), or Controller Area Network (CAN). Nevertheless, if wireless communications are involved, the reliability and timing requirements become great challenges due to the adverse properties of radio channels in the industrial environments. With numerous mobile and static metal objects as potential radio reflectors and scatters, the environments make the radio propagation more unpredictable and unreliable.

In this chapter, we first review the literatures on radio propagation of sensor radios in industrial environments. Conventional modeling methods of radio propagation and radio channels in a variety of environments are reviewed with focus on path loss, multipath propagation, and Doppler shift. We then review the experimental work in industrial environments to provide specific knowledge of radio channels in such environments. Lastly, a preliminary experimental study on the data transmission performance of a fast rotating sensor radio is summarized.

2.1 Wireless Sensor Radio Communication in Factories

Wireless communication in factories is long known to be difficult ever since cellular radios were used in such environments. Radio signals are prone to blockage, multipath fading due

10

to stationary or moving metallic structures near the communicating devices, and radio interferences from machinery and other sources [Rappaport1989a]. For sensor radios, early field tests have revealed that, in factory settings, multipath propagation, structure obstruction and interferences caused location-dependent, channel-specific, and time-varying communication errors.

In [Werb2005], the authors conducted measurements in a machine room and a compressor house, using six IEEE 802.15.4-compliant radios to measure received signal power and packet loss rate between any two radios. Their results revealed that the received signal power and the packet loss rate were both channel-dependent. They concluded that IEEE 802.15.4 at 2.4 GHz appeared to be a suitable physical layer protocol for use in industrial environments, although much more testing and experience was needed. They summarized that the causes that attribute to link quality into four categories: static multipath, time variant multipath, static interference, and time variant interference. Static multipath is only expected to be found in sections of a facility where there is minimal human activity. Time variant multipath occurs every few seconds with human movements, or every few hours with the movements of objects such as vehicles, equipments, doors, and chairs. Static interference, such as microwave ovens or RFID interrogators, may completely block one or all of the radio channels for a period of time; while time variant interference, such as WiFi and Bluethooth, are usually bursty in nature.

Using IEEE 802.15.4-compliant radios, Tang *et al.* presented an experimental study in a university machine shop to measure radio strength and PER to evaluate potential factors for wireless communications, such as distance, stationary and moving obstacles [Tang2006]. The measurements observed path loss exponent consistent with previously reported observations in other factory environments [Rappaport1989a]; and the degradation of received power and packet reception rate was observed when a forklift crossed across the radio link.

In [Tang2007], the same sensor radios were utilized for extensive measurements following a fine grid of locations in a machine shop to investigate the spatial and temporal characteristics of radio channels. The work confirmed the received power's complex dependency on multipath effects and blocking caused by the surrounding structures. Based on an experiment over a 24-hour period, the quality of a radio link exhibited minimal variation under the condition without mobile objects, persons, and interferences.

Other standardized wireless technologies, such as Wi-Fi/IEEE 802.11 and Bluetooth/IEEE 802.15.1, have also been assessed previously. Willig *et al.* presented measurements in a research facility for machinery engineering over a wireless link with an IEEE 802.11-compliant physical layer, and the measurements observed temporal variability of packet loss rate and mean bit error rate (MBER), which the authors attributed to changing environmental conditions [Willig2002]. On an industrial plant floor, Neelakanta *et al.* found mutual interference between Bluetooth and ZigBee devices even with distinct modulations [Neelakanta2003]. In [Abhay2005], the assessment of ZigBee, Wi-Fi, and Bluetooth radio technologies concluded qualitatively the existence of multipath distortion and inter-technology interferences.

While mature techniques have been developed to relax these issues, the simplistic design philosophy of sensor radios has precluded many such options that involve more complex circuitry and higher costs. For multipath fading, most sensor radios adopt none of the common countermeasures such as the RAKE combining circuitry or hardware forward error correction but only rely on the inherent limited multipath tolerance provided by the spread spectrum technology. Given such constraints, sensor radios may not guarantee network connectivity and error-free communications at all times and locations.

2.2   Radio Propagation Modeling

Radio propagation modeling has been a major field of study accompanying the evolution of cellular radios. The majority of these studies have been based on indoor and outdoor field measurements against different types of buildings, materials, and structures. The vast literature has categorized propagation effects for wireless signals being power attenuation with distance, shadowing, diffraction, and scattering by obstacles, as well as multipath fading and Doppler shift. These studies have produced a small set of propagation models that have been widely adopted for wireless communication and networking research.

2.2.1   Power Attenuation due to Path Loss and Shadowing

Path loss is radio signal power dissipation due to wave propagation, media absorption, reflection and diffraction. Shadowing is power attenuation caused by obstacles between the transmitter and the receiver. Received power variations due to path loss and shadowing occur over relatively large distance, so both are referred to as large-scale fading [Goldsmith2005].

Path loss models, if excluding shadowing effects, assume that path loss is fixed for a given transmitter-receiver distance. To date, the majority of path loss models have been derived from either ray-tracing methods or empirical statistical distributions of path loss measurements. The ray-tracing methods are used to approximate radio wave propagation according to Maxwell's equations. The methods are accurate when the number of multipath components is small and the physical environment can be modeled in detail. Two-ray, ten-ray, and general ray tracing models are summarized in [Goldsmith2005]. However, ray-tracing models are impractical for complex propagation environments, in which case an empirical model is commonly used. Empirical models are mainly based on measurements over given distances in the frequency range of interest at a particular location. [Goldsmith2005] also gives brief descriptions for commonly used

empirical models, such as the Okumura model [Okumura1968], which is applicable in large urban macrocells, and the piecewise linear model, which is applicable in outdoor microcells and indoor channel.

There are also simplified path loss models that have been useful in system designs. In [Goldsmith2005], the simplified model is given as a function of the transmitter-receiver distance, d, as follows:

$$P_r(d) \text{ dBm } = P_t \text{ dBm } + K \text{ dB } - 10\gamma \log_{10}\left(\frac{d}{d_0}\right) \tag{2.1}$$

where $P_r(d)$ and P_t are received and transmitted signal power in decibel units, K is a constant that depends on the antenna characteristics and the average channel attenuation, d_0 is a close-in reference distance in the antenna far field and typically assumed to be 1-10 m indoors and 10-100 m outdoors, and γ is the path loss exponent that depends on the environment. When the model is used to approximate empirical measurements, K is set to the path gain at d_0 in free space.

Shadowing effect refers to power attenuation due to blockage by obstacles between two radios. Because object blockage is random for mobile communication systems, the shadowing effect has been commonly accounted for in the path loss model with a random variable. A combined path loss and shadowing model is the log-normal shading model

$$P_r(d) \text{ dBm } = P_t \text{ dBm } + K \text{ dB } - 10\gamma \log_{10}\left(\frac{d}{d_0}\right) - \psi \text{ dB} \tag{2.2}$$

where Ψ is a Gaussian-distributed random variable with mean zero and variance σ^2, which depend on the location, structure, size, and material of the objects in the environment.

Numerous path loss measurements and analysis have been performed in outdoor and indoor environments, such as urban areas, campus, residential or commercial buildings [Seidel1991] [Hashemi1993]. The path loss models for industrial environments usually adopt the

classical empirical models with empirically identified site-dependent model parameters like γ and Ψ [Rappaport1989b].

Radio signal penetration through buildings and other materials causes more signal power attenuation [Telado1998] [Hoppe1999]. [Rappaport1996] and [Goldsmith2005] both summarized and listed the power attenuation due to penetration through a range of structures and materials.

2.2.2   Multipath Propagation

Multipath propagation is a phenomenon due to the presence of reflecting/scattering objects near the communicating devices, causing multiple reflected/scattered copies of the same signal to arrive at the receiver in different amplitude, phase, and time. Multipath propagation can affect channel characteristics in two ways by causing, respectively, power attenuation variation and ISI.

2.2.2.1   Multipath-induced Power Attenuation Variation

Because of the different path length of these signals, they have different arriving time, phase, and attenuation. Depending on the distribution of the signals' phases, the composite signal is formed constructively or destructively. Different from the large-scale fading, the multipath propagation can make signal power vary within a small range of radio movement, since the phase of each individual signal could vary substantially in a few wavelengths. This phenomenon is called small-scale fading.

As the transmitter or receiver movement is random, conventional methods statistically model the power attenuation as a random variable. Most commonly considered distributions include: 1) the Rayleigh distribution, for channels in absence of a strong signal component; 2) the Rician distribution, for channels with a strong signal component. Other distributions may include the Weibull distribution and the Nakagami distribution, etc. Empirical studies have shown the

Weibull distribution is an effective model in both indoor and outdoor environments. The Nakagami distribution provides a more general fading distribution whose parameters are adjustable to fit a variety of empirical measurements [Goldsmith2005].

The total signal power attenuation from the transmitter to the receiver is a consequence of three phenomena: path loss, shadowing, and multipath propagation. In this dissertation, power attenuation is defined as the difference between the decibel powers of transmitted and received signals, presenting the combined result of the small-scale fading and large-scale fading. The statistical models developed for these phenomena have been useful for cellular mobile communication systems to estimate coverage area and evaluate overall signal strength. For sensor radios deployed in industrial environments with frequent movements of human, vehicles, equipments, and other objects, these statistical models might be helpful too. However, fast rotating structures of modern machining machines are usually confined in relatively static space, and the movement paths of the sensor radios rotating with these structures are deterministic once deployed. The statistical models are not correct in this case.

2.2.2.2   Multipath-induced ISI

Multipath propagation results in signal dispersion in time domain. Previous transmitted symbols through a long signal path may have large delay and interfere for the current received symbol. Channel impulse response (CIR) is used to quantitatively assess the extent of signal temporal dispersion caused by the multipath propagation. A time-variant radio channel for an un-modulated signal at carrier frequency f_c is characterized by [Proakis2000]

$$c(\tau;t) = \sum_{i=1}^{N(t)} \alpha_i(t) e^{-j2\pi f_c \tau_i(t)} \delta[\tau - \tau_i(t)] \qquad (2.3)$$

where $N(t)$ is the number of resolvable signal components at t; $\tau_i(t)$ and $\alpha_i(t)$ are the time delay and magnitude gain of the ith signal component. The expression has two time dimensions: t and τ.

t is the time for the channel to observe the transmission of a signal; τ is a relative time to specify the delays of the signal's components.

For a static radio channel, the CIR reduces to

$$c(\tau) = \sum_{i=1}^{N} \alpha_i e^{-j2\pi f_c \tau_i} \delta(\tau - \tau_i) \qquad (2.4)$$

Commonly used measurement approaches of characterizing CIR are the direct method and the swept frequency method. In the direct method, a pulse is launched into the channel, and the channel output is the CIR. The pulse should be short enough so that the highest frequency component of interest is included. In the swept frequency method, the channel input is a continuous sinusoidal wave, which sweeps a large band of frequencies, and the output is the channel's frequency response (FR), which is further used to calculate the CIR by applying the inverse discrete Fourier transform (IDFT).

Figure 2.1 gives an example of the time-variant channel's response to two impulses launched into the channel at t_1 and t_2. The response to the first impulse consists of three signal copies, among which the last one is delayed long enough to arrive later than the first copy of the second impulse. Therefore, for this radio channel, a symbol transmitted at t_1 can interfere with the symbol transmitted at t_2, potentially causing transmission errors.
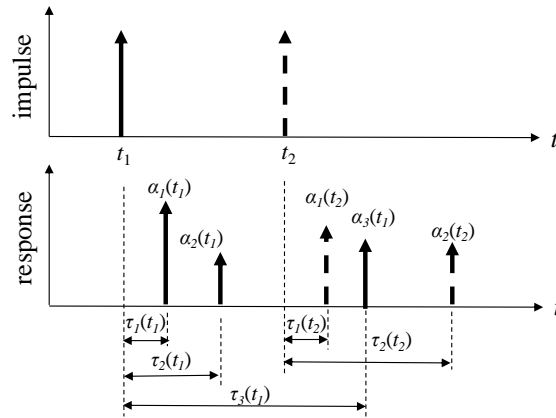
Figure 2.1: Impulse response of a multipath channel with possible ISI

ISI-induced errors cannot be eliminated by simply increasing transmit power, because although the power of the currently transmitted symbol is increased, the interference symbols are intensified by the same ratio as well. In other words, these errors are irreducible if the channel suffers from ISI. Simulation have related the irreducible bit error rate (BER) to the root-mean-square (RMS) delay spread, which is the square root of the second-order central moment of CIR [Chuang1987].

According to [Abouraddy1998], the RMS delay spread, τ_{rms}, is calculated as

$$\tau_{rms} = \sqrt{\frac{\sum_{i=1}^{N} (\tau_i - \tau_f - \tau_m)^2 \alpha_i^2}{\sum_{i=1}^{N} \alpha_i^2}} \tag{2.5}$$

where τ_f is the delay of the first arriving signal component, and

$$\tau_m = \frac{\sum_{i=1}^{N} (\tau_i - \tau_f) \alpha_i^2}{\sum_{i=1}^{N} \alpha_i^2} \tag{2.6}$$

For a given digital radio with symbol duration T_s, the normalized RMS delay spread is calculated by

$$d = \frac{\tau_{rms}}{T_s} \tag{2.7}$$

The simulation in [Chuang1987] provides a relationship between the normalized RMS delay and the ISI-induced irreducible BER for a number of different radio modulation/detection schemes.

Deployed in multipath-rich environments like factories, especially closed space confined by metal enclosures, sensor radios are likely to see substantial ISI-induced transmission errors unless advanced interference mitigation technologies are employed. Systematic experiments and

analysis are required for an assessment of the typical RMS delay spread level during the design and planning of wireless sensor systems.

2.2.3 Doppler Shift

Doppler shift describes the frequency and phase shifting effect of the received signal due to relative motion between the transmitter and receiver. [Goldsmith2005] gives the equation of the Doppler frequency shift for a line-of-sight (LOS) signal path to a moving receiver. The receiver movement over a short time interval Δt causes a slight change in the signal path length. The length change is

$$\Delta d = v \Delta t \cos \theta \tag{2.8}$$

where v is the receiver velocity relative to the transmitter, θ is the arrival angle of the received signal relative to the direction of motion.

The corresponding phase change due to this path length change is

$$\Delta \phi = 2 \pi v \Delta t \cos \frac{\theta}{\lambda} \tag{2.9}$$

where λ is the signal wavelength.

The Doppler frequency shift, which is often called Doppler frequency, is then obtained as

$$f_D = \frac{v}{\lambda} \cos \theta \tag{2.10}$$

If the receiver is moving toward the transmitter (i.e., if $-\frac{\pi}{2} \leq \theta \leq \frac{\pi}{2}$), then the Doppler frequency is positive; otherwise, it's negative.

In a typical multipath environment, the signals on different reflected paths are associated with different angles of arrival, and the Doppler shift of each arriving path is generally different from that of another path. As the composite of these frequency-shifted signals, the received signal

shows power spreading over a range of frequency, rather than a single frequency shift. In this case, the Doppler effects can be analyzed with the Doppler power spectral density, $S_C(\rho)$, where ρ is the frequency shift relative to the carrier frequency [Goldsmith2005]. The spectral density describes how a signal broadens or shifts its energy over a range of frequencies. The maximum ρ-value for which $|S_C(\rho)|$ is greater than zero is called the Doppler spread of the channel, denoted by B_D. And B_D is limited by [Goldsmith2005]

$$\left| B_D \right| \le \frac{v}{\lambda} \tag{2.11}$$

In time domain, channel coherence time, denoted as T_C, is a measure of the expected time duration over which the channel's response is essentially invariant. The approximate relationship between B_D and T_C is given as [Goldsmith2005]

$$T_C \approx \frac{1}{B_D} \tag{2.12}$$

The Doppler shift causes irreducible errors that cannot be overcome by simply increasing signal power. For digital communications, if the duration of a symbol is smaller than the channel's coherence time, the temporal distortion in a received symbol due to the Doppler shift is insignificant to affect correct symbol reception [Rappaport1996]. A more precise method has been summarized with respect to the Doppler spread in [Sklar1997]: to avoid the Doppler-induced irreducible error rate, the symbol rate should exceed the Doppler spread by a factor of 100-200, while the exact factor depends on the signal modulation, receiver design, and required error rate.

For the channels of fast rotating sensor radios, the Doppler shift may or may not take significant adverse effects on data transmission. The actual influence need to be analyzed case by case. However, in many cases, it's very difficult to know the Doppler spread, and the worst-case

scenario is considered in which the Doppler spread is the largest possible value based on Equation (2.11).

2.3   Radio Propagation in Industrial Environments

Late 1980's researchers started to characterize radio propagations in industrial environments as wireless communication technologies were increasingly adopted into modern factory monitoring and control systems [Rappaport1988] [Rappaport1989b] [Rappaport1989c] [Yegani1989] [Yegani1991].

In [Rappaport1989c], extensive wide-band propagation measurements at 1300 MHz were made in five operational factories. The experiment data revealed that path loss was highly correlated with transmit-receiver separation and the average path loss was a function of distance to the 2.2 power (γ in Equation (2.1)). The RMS delay spread were found to range from 30 ns to 300 ns and appeared to be unrelated to path distance and path loss. The studies also showed in factory buildings, building age, inventory, wall locations and ceiling height were key factors in determining the shape and extent of the multipath profile; topographical descriptions about the factory provided insight into the shapes of impulse responses, but cannot be used to distinguish delay spread. It also suggested that radio propagation in factory buildings may be suitably described by a hybrid geometric/statistical model that accounted for both specular reflections from walls and ceilings and random scattering from inventory and equipment.

Based on wide-band multipath measurements at 1300 MHz in several factories, Yegani *et al.* developed a mathematical model for factory radio channels to statistically describe channel parameters such as path gain coefficients (α_i's in CIR in Equation (2.4)), path interarrival times (intervals between τ_i's in CIR), and number of paths (N in CIR). Both LOS channel and obstructed (OBS) channel had been considered. The path gain coefficients were represented using

21

Rayleigh, Rician, or lognormal distribution. The interarrival times of the signals were modeled by the Weibull distribution, and the shape and scale parameters of the distribution were dependent on the factory environments and the channel types. Using the modified beta distribution, a model was presented for the distribution of the number of signals. The parameters of the Beta distribution were also different for different sites and types of the radio channel. For the OBS channels, the number of signals was found mostly between 25 and 40, while for the LOS channels, the number was below 30.

Another multipath propagation measurement at about 2.45 GHz in industrial sites was conducted on a petrochemical processing plant, an electricity distribution transformer station, and a parking area amongst multi-story offices [Kemp2005]. For each site, several locations were chosen for transmitter and receiver placement. For each transmitter-receiver location, CIR and BER measurements were performed. On the petrochemical plant, the RMS delay spread was in the range from 20 ns to 70 ns with most scattering around 35 ns to 45 ns; on the transformer station, it was in the range from 30 ns to 140 ns with most between 90 ns and 100 ns. By plotting a scatter plot of normalized-RMS delay spread and measured BER, the researchers confirmed Chuang's rule-of-thumb about the ISI-induced irreducible error rate [Chuang1987]: a normalized-RMS delay spread of a tenth leads to an irreducible BER of 10^{-3}.

Hampicke *et al.* conducted wide-band propagation measurements at 5.2 GHz for LOS and non-LOS (NLOS) channels in a car manufacturing hall and measured Doppler frequency shifts by moving the transmitter [Hampicke1999]. For the NLOS channel an almost ideal classical Jakes Doppler spectrum was observed, although there were higher Doppler frequencies than expected based on the transmitter speed and the typical velocities of the objects in the hall. Further inspection suggested it was caused by fluorescent tubes mounted along an aisle.

2.4   Transmission Performance of Rotating Sensor Radios and Potential Error Causes

Few works have been reported on data transmission performance of fast rotating sensor radios. In [Sarkimaki2006], Sarkimaki claimed that no significant transmission errors were observed in the experiments with their rotating ZigBee wireless torque system and, based on the coherence time check, Doppler effects were negligible.

In [Wang2007] and [Tang2009], a series of experiments was performed in a *HARDINGE*® TALENT™ 6/45 CNC lathe. The sensor radios were *Crossbow* MICAz wireless modules, which are IEEE 802.15.4-compatible. In the experiment a transmitter was rotating on the lathe's spindle with speeds up to 2000 rpm equivalent to a tangential speed up to 13.6 m/s. As the transmitter was continuously sending packets, a stationary receiver nearby counted the correctly received packets. The experiments were repeated at two 3-cm-apart receiver locations: location 1 and location 2, as shown in Figure 2.2.
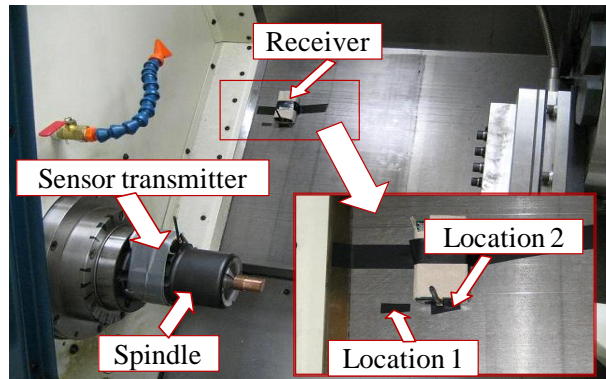
Figure 2.2: Transmitter and receiver placement in the CNC lathe

As a metric of data transmission performance in this dissertation, PER is defined as the ratio of the number of packets lost or containing bit errors to the number of all transmitted packets. It's been observed that, at location 1, the PER proportionally increased with the speed, as shown in Figure 2.3. Further analysis showed the errors were bursty and the majority of error

bursts occurred near a same transmitter location. While at location 2, the PER was between 0.001 and 0.01 with no relationship with the speed.
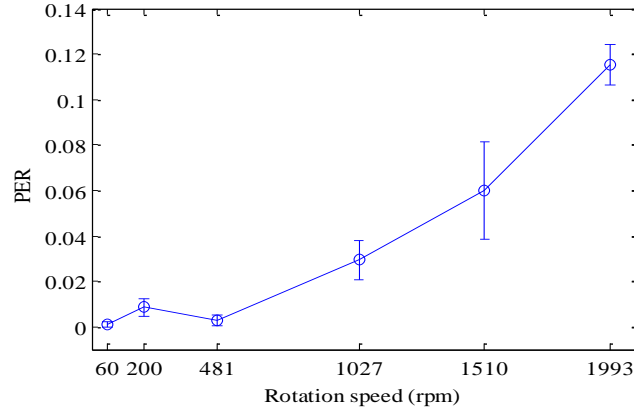
Figure 2.3: Proportional increase of PER with rotation speed

In addition to the sensor radio experiments described above, additional experiments were conducted with an *HP* 8714 ES VNA and an *HP* 8560 spectrum analyzer to characterize channel properties and background noise in the lathe. Based on all these experiments, the potential causes of the sensor radio transmission errors are examined as follows.

2.4.1   Received Power and Power Attenuation

In the sensor radio experiments, with the stationary transmitter being placed on different locations on the spindle's periphery, PER and received signal power were measured. At most locations, PERs were near or at zero, while at certain locations, PERs suddenly jumped to nearly 1, and in the meantime their associated received power dropped radically. The phenomenon suggests the data transmission performance is highly related to the received power.

According to the IEEE 802.15.4 standard, BER can be estimated from signal-to-noise ratio (*SNR*) as [IEEE802.15.4]

$$\frac{8}{15} \times \frac{1}{16} \times \sum_{k=2}^{16} (-1)^k \binom{16}{k} e^{\left(20 \times SNR \times \left(\frac{1}{k}-1\right)\right)}$$

(2.13)

where *SNR* is determined by the received power P_r and the noise P_N as

$$SNR = \frac{P_r}{P_N} \tag{2.14}$$

In practice, BER can substantially deviate from this estimate, especially when the received signal power approaches the radio's receiving sensitivity as commonly observed in many wireless sensor studies [Zhao2003] [Reijers2004] [Srinivasan2006] [Tang2009]. For any radio, the receiving sensitivity is a specific power level below which the BER quickly deteriorates. Hence, our BER sub-model will incorporate this effect.

Most commercial radios provide in their specification the sensitivity power level. The IEEE 802.15.4 standard mandates all compatible radios to report their receiving sensitivity as the threshold input signal power that yields PER of 1% for a 20-octet long physical layer service data unit (PSDU, i.e., a transmitted packet) [IEEE802.15.4]. Each manufactured radio, even of the same vendor and model, can have different sensitivity thresholds; hence, the manufacture reported sensitivity only serves as a typical value for an inaccurate reference. The measurement of the sensitivity according to such a definition requires specialized instruments and expertise [Atmel2008].

When the received signal power falls within a specific power area near the radio sensitivity, the observed BER typically fluctuates vibrantly. This power area is called a grey area. Figure 2.4 gives an example of observed BER using the MICAz motes. When the received power is above -93 dBm, the BER is fairly low down to 0. When the received power is below -94 dBm, the BER is as high as 1. When the received power is between -93 dBm and -94 dBm, the BER fluctuates with a general declining trend with increasing received power. In this case, the grey area is approximately between -94 and -93 dBm. In [Srinivasan2006], such variations were attributed to local noise perceived by the receiving radio.
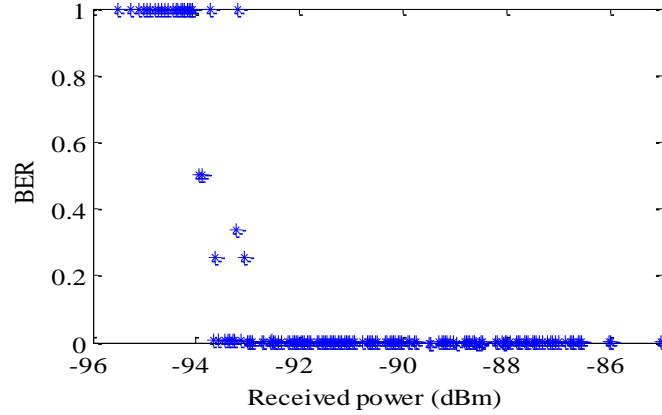
Figure 2.4: Measured BER vs. received power

2.4.2 Multipath-induced ISI

To evaluate ISI in the lathe, experiments with an *HP* 8714 ES VNA were conducted to measure frequency response of radio channel in the lathe. In the experiments, with the transmitter sequentially placed on the spindle's periphery, the frequency response was measured for each transmitter location to further obtain CIR. The normalized-RMS delay spread was computed based on Equations (2.5) – (2.7), in which the symbol duration T_s was 16 μs for the MICAz motes. The normalized-RMS delay spread in the CNC lathe was on the order of 10^{-3}. According to the simulation results in [Chuang1987], this can cause ISI-induced irreducible BER as low as 10^{-6} for the offset quadrature phase-shift keying (OQPSK)-modulated radios of the MICAz motes.

Equipment to record the CIR of a rotating transmitter was not available, and, hence, evaluating RMS delay spread was not possible. Nevertheless, since the multipath propagation pattern depends on the environment and the radios' locations, the RMS delay spread is expected to be consistent despite the rotation. Based on this assumption, it may be concluded that ISI is negligible for the rotating sensor radios in the CNC lathe.

2.4.3 Doppler Shift

The maximum rotation speed of the transmitter was set at around 2000 rpm in our experiments, and the diameter of the transmitter's rotation route was around 13 cm. So, the equivalent maximum velocity was 13.5 m/s. Meanwhile, the frequency of the sensor radios on MICAz motes was set to 2.48 GHz, so the wavelength was 0.121 m. According to Equation (2.11), the Doppler spread was upper bounded by 112 Hz. The symbol duration of the radios was 16 μs; equivalently, the symbol rate was 62.5 kHz, which exceeded the largest possible Doppler spread by a factor of 558. As mentioned in Section 2.2.3, this order of Doppler spread was negligible to cause Doppler-induced irreducible error rate.

Since the tangential velocity of around 10 m/s is considered a high speed for machining processes [Haber2005], in common machining-monitoring situations, Doppler-induced error rate is even smaller than the error level in our case. By limiting our research scope to this velocity level and this sensor radio hardware (or other radios with similar configurations), Doppler effects will not be considered in the PER predictive model.

2.4.4 Machine Electromagnetic Noise

Machine electromagnetic noise is a result of stray radio emissions caused by electric field variations during machine operation. Previous studies found such stray radio emissions mostly in frequencies below 1.5 GHz [Jabbar1989] [Staub1997] and claimed that such noise would not severely affect most radio systems at Ultra High Frequencies (UHF, 300MHz-3GHz) and above [Rappaport1989a]. The claim, however, has not been verified for wireless sensors. Given the low transmit power and receiver simplicity of wireless sensors, the potential impacts of machine noise must be re-evaluated.

Machine electromagnetic noise can be dependent on speed, and such noise effects are not expected to have sensitive dependency on small receiver location changes. From the rotating sensor radio experiments, the vastly different PERs acquired from two close receiver locations suggest that the machine noise, even if present, is not a significant factor of data transmission performances.

As an additional visual verification, an *HP* 8560 spectrum analyzer was used to record the electromagnetic spectrum at the 2.4~2.5 GHz band with the machine turned off as well as with the machine running at 2000 rpm. A directional horn antenna was used for the measurement. Under each condition, the spectrum analyzer recorded the maximum power on each point of the frequency band in a period of 10 minutes. From the two obtained spectrums, the power differences between on and off states for IEEE 802.15.4-defined channel 26, i.e., 2478.5 ~ 2481.5 MHz, where the sensor operated, were calculated to be all less than 1 dB, an insignificant level to affect radio reception.

2.4.5   Hardware Instability

Sensor radio hardware can be less reliable during fast motion if the antenna connection loosens. The MICAz mote is implemented as a fully integrated printed circuit board (PCB) with its antenna being the only screw-attached component, e.g., via a micro-miniature coaxial (MMCX) connector [MICAz]. The battery pack soldered on board can also loosen under vibration and an intermittent contact would cause intermittent radio operation.

The consistently good transmission performance at receiver location 2 provided sufficient evidence that the speed-dependent errors observed at location 1 were not due to unstable hardware on the transmitter during high speed rotation. For further verification of the antenna stability, the experiments were repeated using the TelosB mote [TelosB], which has a printed

circuit board antenna. No pronounced differences in the PER acquired at locations 1 and 2 were observed, suggesting that the MMCX-connected antenna had similar integrity as a printed antenna up to 2000 rpm, and that antenna instability had insignificant effects on data transmission performance in this study.

In summary, low received signal power is identified as a main error cause of fast rotating sensor radios, and ISI for a rotating sensor radio situation needs further evaluation. Doppler shift, machine noise, and hardware instability are proved to have insignificant impacts under the dissertation studied conditions and will not be included for modeling transmission performance.

2.5   Challenges

In this dissertation, the following challenges will be addressed towards the derivation and the validation of the transmission performance model.

- Define a deterministic model that predicts signal power attenuation for given channel multipath propagation.

- Define a BER model that counts in the radio receiving sensitivity effect to predict BER.

- Discover the intrinsic relationship between rotation speed and data transmission performance.

- Measure instantaneous channel properties of a particular transmitter location during rotation. A new rotating structure equipped with a positioning mechanism needs to be designed so that the location of the rotating transmitter can be detected to activate an instant channel measurement.

Chapter 3

PER Predictive Model

A predictive model for PER of sensor radio transmission in fast rotating machines is derived according to communication principles. Given the model inputs of channel multipath profile, radio signal frequency, transmit power, rotation speed, packet length, BER grey area thresholds and data rate, the model predicts power attenuation, BER and PER of the wireless transmission in three stages. The model enables the prediction of radio data transmission reliability and capacity in a rotating machine environment. The model is experimentally validated in Chapter 5. Section 3.1 defines two important hypotheses to infer a fundamental assumption of the model. Section 3.2 describes the model structure and defines three sub-models in detail.

3.1   Model Hypotheses

Two hypotheses are proposed as basic assumptions for the PER predictive model:

Hypothesis 1: *Within the speed range attainable in the study, RMS delay spreads of all transmitter locations are small and cause no significant ISI-induced errors despite transmitter rotation.*

Hypothesis 2: *Within the speed range attainable in the study, power attenuation of each transmitter location is not affected by transmitter rotation.*

The hypotheses will be experimentally validated in Chapter 5.

As discussed in Section 2.4, for the stationary transmitter in the CNC lathe, RMS delay spread is too small to cause transmission errors. If Hypothesis 1 is true, it's valid to assume ISI-induced BER is insignificant in both stationary and rotating transmitter scenarios; hence, received power is the main error cause in both scenarios. With Hypothesis 2, it can be inferred that BER of any particular transmitter location is also consistent despite transmitter rotation. Further, when the transmitter rotates on a fixed circular route, the BER profile is fixed regardless of rotation speed. This inference is the critical foundation for the PER predictive model.

3.2 Model Structure

3.2.1 Overview

Figure 3.1 illustrates the model structure. The model consists of a signal power attenuation sub-model, a BER sub-model, and a PER sub-model. The signal power attenuation sub-model derives the power attenuation profile over the 360 ° transmitter rotation route; the BER sub-model derives the corresponding BER profile; the PER sub-model derives the cycle PER, which is defined as the average error rates of packets transmitted at any locations during the transmitter rotation.
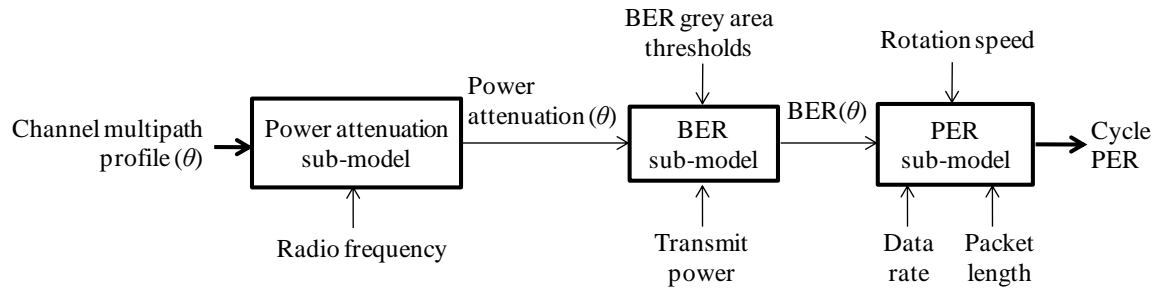
Figure 3.1 Structure of the PER predictive model (θ: transmitter location from 0 ° to 360 °)

Input parameters of the model are summarized under three categories:

- Radio location and surrounding environment

    The multipath profile of the communication channel is determined by the environment surrounding the transmitter and receiver radios. In the proposed model, the channel multipath profile is parameterized by $\Pi = \{N, \tau_i, \alpha_i; i = 1, \ldots, N\}$, where N is the number of resolvable signal propagation paths, τ_i is the time delay of the ith signal path, and α_i is the amplitude gain of the ith signal path. In a rotating machine with a moving transmitter, a stationary receiver and no other moving parts, the profile completely depends on the transmitter location on the rotation route. For a given spindle and a transmitter attached to it, the transmitter location can be expressed using the spindle rotated angle θ with respect to a pre-determined location. For the entire rotation route, a set of θ dependent channel multipath profiles is defined as $\Pi(\theta)$.
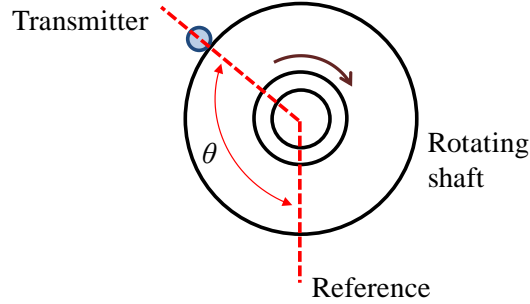
Figure 3.2: Transmitter angular location θ referring to the reference

- Rotation parameter

    The spindle rotation speed ω determines the angle that a transmitter traverses during the transmission time of a packet and, as a result, the extent of channel multipath profile variation it experiences.

- Radio and transmission protocol parameters

The carrier frequency f_c, transmit power P_t, data rate d, and packet length n of a transmission are key parameters in the model. The carrier frequency affects the multipath signals' power attenuation and hence the first sub-model, the transmit power affects the received power and hence the BER sub-model, while the data rate and packet length affect the transmission duration and hence the PER sub-model. In addition, any radio is expected to have its respective BER grey area thresholds, P_{GL} and P_{GH} such that transmissions received with power between the two thresholds exhibit unpredictable BER fluctuations. The BER grey area, as discussed in Section 2.4 must be experimentally measured for each different radio receiver.

The model depends on a number of other radio and transmission protocol factors that are not explicitly modeled in this dissertation. For example, the transmission protocol, such as its modulation and forward error correction (FEC) schemes, will also affect the BER. In this dissertation, we focus on IEEE 802.15.4 radios that have only one modulation scheme and no FEC; hence, these factors are not included in the model.

In addition to predicting the cycle PER, the three-stage model also exposes intermediate properties of the radio link that are useful for providing a physical understanding of the radio channel effects and performances. Table 3.1 summarizes all used variables and parameters in the study.

Table 3.1: Summary of parameters and variables

	Notation	*Description*
Power attenuation sub-model	$\Pi = \{N, \tau_i, \alpha_i; i = 1, \dots, N\}$	Channel multipath profile
	f_c	Radio frequency
	θ	Transmitter location
	$PA_L(\theta)$	Local power attenuation
BER sub-model	P_t	Transmit power
	$[P_{GL}, P_{GH}]$	BER grey area
	$BER(\theta)$	BER
PER sub-model	d	Data rate
	n	Packet length
	ω	Rotation speed
	$PER_C(\omega)$	Cycle PER
Intermediate parameters	P_r	Received power
	P_N	Noise
	SNR	Signal-to-noise ratio
	$PA_L(\theta, \omega)$	Local power attenuation
	$FR(\theta, \omega)$	Frequency response
	$PER_L(\theta, \omega)$	Local PER

3.2.2   Signal Power Attenuation Sub-model

The power attenuation sub-model derives the power attenuation caused by a given channel multipath profile. The power attenuation is expressed as the ratio between the transmitted and the received signal power as

$$PA = \frac{P_t}{P_r} \tag{3.1}$$

An amplitude modulated signal produced by a transmitting radio is written as [Sklar2001]

34

$$s(t) = \text{Re}\{ g(t)e^{j2\pi f_c t} \} \tag{3.2}$$

where $g(t)$ is the baseband waveform over time t and f_c is the carrier frequency. Other modulation techniques, such as the phase modulation, are also adopted in modern radio systems; for our modeling purpose, only amplitude modulation is considered in this dissertation.

For the transmitted signal in Equation (3.2), the received signal can be written as

$$r(t) = \text{Re}\left\{ \left(\sum_i^N \alpha_i e^{-j2\pi f_c \tau_i} g(t - \tau_i) \right) e^{j2\pi f_c t} \right\} \tag{3.3}$$

where N and $\{\tau_i, \alpha_i; i=1\ldots N\}$ are the parameters in Π.

For a spread spectrum communication system that covers a relatively small frequency band such as the IEEE 802.15.4 radio with a 3 MHz wide channel bandwidth considered in this dissertation, the signal power attenuation α_i can be considered as constant throughout the band.

To simplify the analysis, the following derivations consider only an unmodulated carrier signal that can be reduced from Equation (3.2) as

$$s(t) = \text{Re}\{ e^{j2\pi f_c t} \} = \cos(2\pi f_c t) . \tag{3.4}$$

The corresponding received signal becomes

$$r(t) = \text{Re}\left\{ \left(\sum_{i=1}^N \alpha_i e^{-j2\pi f_c \tau_i} \right) e^{j2\pi f_c t} \right\} . \tag{3.5}$$

$\sum_{i=1}^N \alpha_i e^{-j2\pi f_c \tau_i}$ can be expressed in a concise form as $\alpha e^{-j2\pi f_c \tau}$, where α is

$$\alpha = \left| \sum_{i=1}^N \alpha_i e^{-j2\pi f_c \tau_i} \right| . \tag{3.6}$$

Hence, the received signal is a cosine signal as

$$r(t) = \text{Re}\left\{ \left(\alpha e^{-j2\pi f_c \tau} \right) e^{j2\pi f_c t} \right\} = \alpha \cos(2\pi f_c (t - \tau)) . \tag{3.7}$$

From Equation (3.4) and (3.7), the power attenuation as defined in Equation (3.1) is

$$PA = \frac{P_t}{P_r} = \frac{\frac{1}{T} \int_0^T (\cos(2\pi f_c t))^2 \, dt}{\frac{1}{T} \int_0^T (\alpha \cos(2\pi f_c (t - \tau)))^2 \, dt} = \frac{1}{\alpha^2} \quad (3.8)$$

where T is the signal's period, i.e., $1/f_c$.

Decibel units are commonly used when analyzing communication systems. For example, any signal power of P watts can be expressed in decibel units in reference to 1 mW as

$$10 \log_{10} \frac{P}{1 \text{ mW}} \text{ (dBm)} . \quad (3.9)$$

Accordingly, Equations (3.1) and (3.8) can be rewritten in decibel units as

$$PA \text{ (dB)} = P_t \text{ (dBm)} - P_r \text{ (dBm)} \quad (3.10)$$

$$PA \text{ dB} = -20 \log \alpha . \quad (3.11)$$

Throughout the dissertation, variables explicitly labeled with dB or dBm are in decibel units; otherwise, the variables are in linear units.

3.2.3   BER Sub-model

The BER sub-model derives the BER, given power attenuation, transmit power, and the radio's BER grey area thresholds. With the power attenuation and the transmit power, the received power is calculated based on Equation (3.1).

As reviewed in Chapter 2, according to the IEEE 802.15.4 standard, BER is analytically estimated by Equation (2.13); however, the practical sensor radio measurements suggest the equation is inapplicable when the received power is less than P_{GH}. Also, further measurements suggest, in the environments studied in this dissertation, the predicted BER closely approaches 0 when the received power is larger than P_{GH}, because the noise is so low that the SNR is high enough to result in a nearly zero BER. For example, the measured noise at the interested frequency was -110 dBm in the CNC lathe and -115 dBm in an anechoic chamber, and the radio's

36

P_{GH} was -93 dBm. When the received power is larger than -93 dBm, the calculated BER by Equation (2.13) is always nearly 0.

Instead of an analytical estimation method, an empirical BER sub-model is proposed for this type of environments: BER is 1 for the received power below P_{GL} or 0 for the received power above P_{GH}; for the received power between P_{GL} and P_{GH}, BER is a linear transition from 1 to 0. The sub-model is expressed as

$$BER = \begin{cases} 1 & P_r < P_{\text{GL}} \\ \dfrac{P_{\text{GH}}(\text{dBm}) - P_r(\text{dBm})}{P_{\text{GH}}(\text{dBm}) - P_{\text{GL}}(\text{dBm})} & P_{\text{GL}} \le P_r < P_{\text{GH}} \\ 0 & P_r \ge P_{\text{GH}} \end{cases} \qquad (3.12)$$

Despite the potential inaccuracies due to the BER estimation in the grey area, for the fast varying radio channel of a rotating transmitter, the grey area occurs only for a small fraction of the rotation route, and hence the resulting errors seen throughout the rotation route are small, as will be shown in Chapter 5.

3.2.4 PER Sub-model

The PER sub-model derives the cycle PER as a function of rotation speed, BER profile, radio data rate and packet length. The BER profile is a set of individual BER for each location around the transmitter's circular route. During the transmitter rotation at the speed of ω, each bit of a transmitted packet may experience a different BER, as illustrated in Figure 3.3.
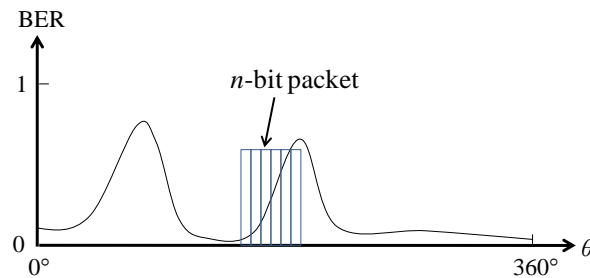
Figure 3.3: An n-bit packet transmission experiencing varying BER

Thus, the PER of a packet transmitted at location θ is expressed as

$$PER_L(\theta, \omega) = 1 - \prod_{i=0}^{n-1}\left[1 - BER\left(\theta + i\frac{\omega}{m}\right)\right] \qquad (3.13)$$

where ω is in $\%s$ and m is the radio's data rate in bits/s.

Assuming packet transmissions begin at uniformly random locations around the circular route, the cycle PER is

$$PER_C(\omega) = \sum_{i=1}^{\frac{360}{\Delta\theta}} \frac{\Delta\theta}{360} PER_L((i-1)\Delta\theta, \omega) \qquad (3.14)$$

where $\Delta\theta$ is the angular resolution of BER(θ).

For infinitesimal $\Delta\theta$, the continuous form of Equation (3.14) is

$$PER_C(\omega) = \int_0^{360} PER_L(\theta, \omega)\frac{1}{360}d\theta \qquad (3.15)$$

In fact, $PER_C(\omega)$ is the arithmetic average of $PER_L(\theta, \omega)$ over the transmitter's entire circular route.

3.3   Summary

This chapter presented the PER predictive model for sensor radios on fast rotating machines. The BER consistency assumption was inferred from two hypotheses as foundation of the model. The PER predictive model consists of three sub-models, i.e., the signal power attenuation sub-model, the BER sub-model, and the PER sub-model. For given model inputs, the sub-models predict power attenuation, BER and PER of the wireless transmission respectively. The following chapter will present the design of experiments to validate the hypotheses and the sub-models.

Chapter 4

Experiment Design

In order to validate the PER predictive model proposed in Chapter 3, a series of experiments was designed and performed in a CNC lathe and a rotating apparatus, respectively. The rotating apparatus was equipped with a photo sensor to detect the location of the rotating transmitter, so that instantaneous channel properties, such as local PERs and local power attenuations, can be measured at particular transmitter locations. The experiments on the rotating apparatus were conducted in an anechoic chamber to reduce uncontrolled multipath effects and interferences. To measure different channel properties, two measurement setups were built: measuring PER required a sensor radio-based setup and deriving channel multipath profile required a VNA-based setup. Section 4.1 introduces the key components of rotation equipments and measurement setups. Section 4.2 gives an overview of measurement procedures. Section 4.3 provides the details of measurement setups, execution, and data processing methods. Section 4.4 summarizes the measurement setups and design.

4.1 Hardware Overview

4.1.1 Sensor Radio

The sensor radios used in the experiments were wireless communication modules provided by *Crossbow* [MICAz]. The radios are called MICAz motes. Figure 4.1(a) shows a

photo of the mote. The mote size is 5.8 cm long, 3.2 cm wide and 2.2 cm high. The mote's antenna is a quarter-wavelength monopole antenna (about 4.2 cm long).

(a) MICAz mote   (b)   MIB 510
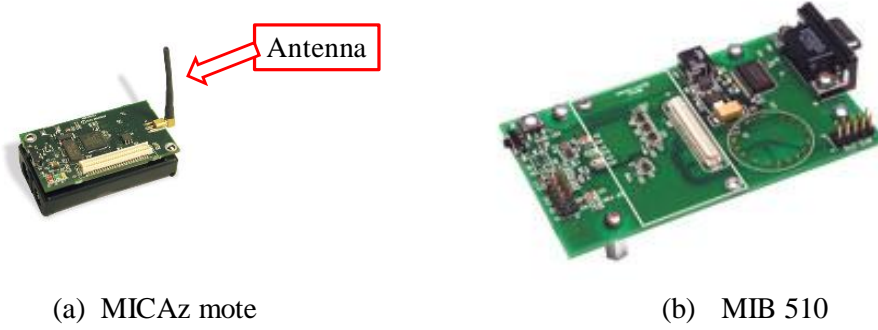
Figure 4.1: Photos of MICAz mote and MIB 510

The mote uses a *Texas Instrument* CC2420 radio chip which is an IEEE 802.15.4-compliant and ZigBee-ready RF transceiver. The radio supports 250 kbps data rate, -25~0 dBm controllable transmit power, and 16 channels in the 2.4 GHz band [CC2420]. The typical receiving sensitivity is -94 dBm. The modulation scheme of the radio is offset quadrature phase-shift keying (OQPSK). For each received packet, the radio provides a received signal strength indication (RSSI) based on the first 8 symbols of the packet and a cyclic redundancy check (CRC) bit produced by an error-detecting circuit. The RSSI is a 8-bit digital value and linear transformable into the received power in dBm unit by

$$\text{Received power (dBm)} = \text{RSSI\_VAL} + \text{RSSI\_OFFSE T} \tag{4.1}$$

where RSSI_VAL is the RSSI value and RSSI_OFFSET is approximately -45 dBm. The CRC bit indicates the correctness of the received packet: if CRC is 1, the packet is validated by the check algorithm; if it's 0, the packet contains bit errors. The mote's oscillator provides a time stamp which can be recorded at events such as a packet receiving or an interrupt stimulated by an external signal.

A *Crossbow* Mote Interface Board (MIB510) was used in the setup. The board works as an interface between a MICAz mote and a computer for data transfer, using a universal asynchronous receiver-transmitter (UART) port. Figure 4.1(b) shows a photo of the MIB510.

4.1.2 VNA

The VNA used in the experiments was an *HP* VNA 8714ES with the frequency band from 300 kHz to 3 GHz [HP8714]. Figure 4.2 (a) shows the VNA front panel. The VNA can transmit or receives RF signals through Port 1 or Port 2 depending on user's setting. The VNA's trigger port is a female BNC connector on the rear panel. A General Purpose Interface Bus (GPIB) port on the rear panel provides a data communication connection between the VNA and a PC. An *Agilent* 82357A GPIB - universal serial bus (USB) adapter was used for the connection. Figure 4.2 give the photos of the VNA and the adapter.
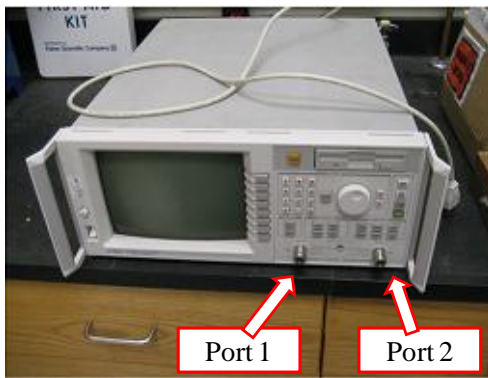
(a) VNA   (b) GPIB-USB adapter

Figure 4.2: Photos of the VNA and the GPIB-USB adapter

Two types of antennas were used with the VNA in the experiments. On the receiving side, a balun was used to make the receiving antenna's propagation pattern consistent and uniform. The balun was provided by *Picosecond* and the model was 5100. The receiving antenna was a dipole antenna connected to the balun as shown in Figure 4.3. However, no balun was used on the

transmitting side for safety concerns, because the transmitting antenna would be fast rotating in the experiments. To create a channel similar to the sensor radio channel, the transmitting antenna was a monopole antenna as same as the one on a MICAz mote.
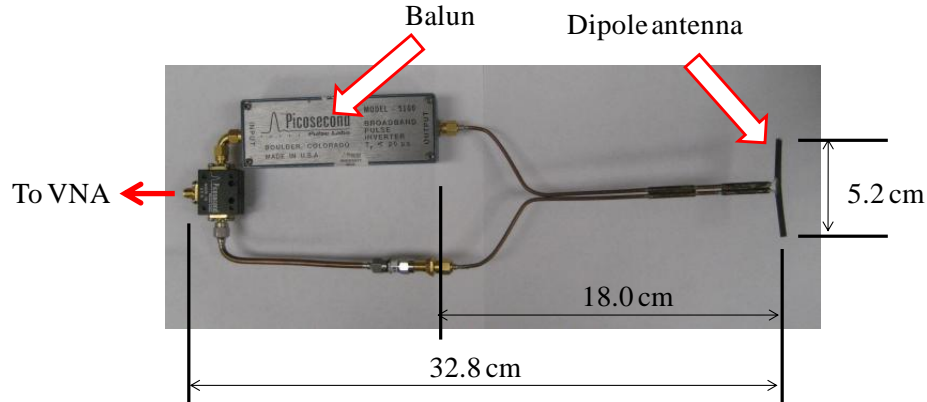
Figure 4.3: Balun and dipole antenna as the receiver

A LabVIEW program was developed on the PC for measurement control, data retrieval and storage. Figure 4.4 shows the user interface of the program.
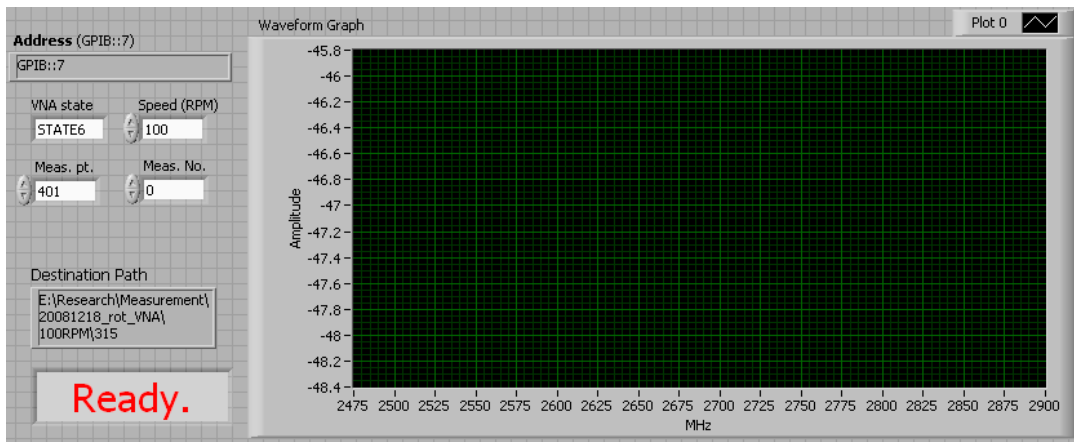
Figure 4.4: LabVIEW-based VNA control program

4.1.3 Rotating Systems

Two rotating systems were used in this study: 1) a CNC lathe and 2) an assembled rotating apparatus. The CNC lathe represents an actual production machine, while the rotating

apparatus is custom made to enable sensor positioning for measuring the channel at specific locations during rotation. The experiments on the apparatus were conducted in an anechoic chamber to avoid uncontrolled environmental multipath effects.

4.1.3.1 Rotating Spindle in CNC Lathe

The CNC lathe used in the experiments was a Talent 6/45 CNC lathe provide by *Hardinge* Inc. The lathe exterior is shown in Figure 4.5(a). The lathe is equipped with a 60~6000 rpm speed-controllable spindle in a metallic enclosure space and can display the speed on its front panel.

(a) CNC lathe   (b) Paper-made encoder on the spindle
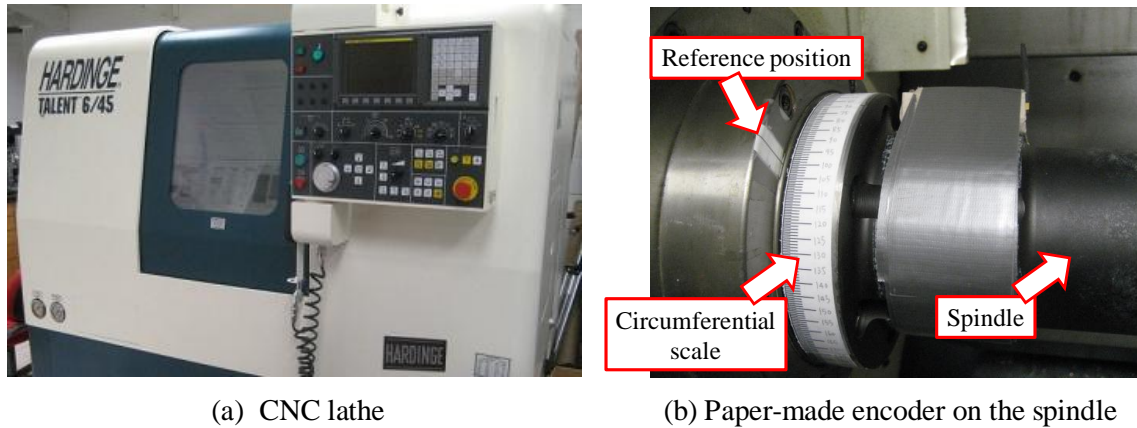
Figure 4.5: CNC lathe and encoder

To determine the transmitter location on the lathe spindle, a paper-made encoder was attached to the spindle. A close view of the spindle and the encoder is shown in Figure 4.5(b). A line marker was attached on the stationary part right next to the spindle to serve as reference position. The circumferential scale around the spindle evenly divided the circumference into 720 units resulting in a resolution of $0.5°$. However, the encoder cannot determine the transmitter location during rotation.

4.1.3.2 Rotating Apparatus in Anechoic Chamber

The rotating apparatus used in the experiments in the chamber consisted of a permanent magnet DC motor and a rotating plate. The motor was *DAYTON* 1F800 with the nameplate speed at 1750 rpm. A controller was equipped with the motor to tune rotation speed and switch rotation direction. The motor and the rotating plate were supported by brackets on a bench. Figure 4.6 shows the rotating apparatus setup for sensor radios, and Figure 4.7 shows the setup for the VNA. To work with the VNA, the system used a rotary joint, MI-10-3 from *MI Technologies*, on the rotating plate to avoid cable twist. The rotary joint supported DC - 8 GHz frequency band and 500 rpm rotation speed.
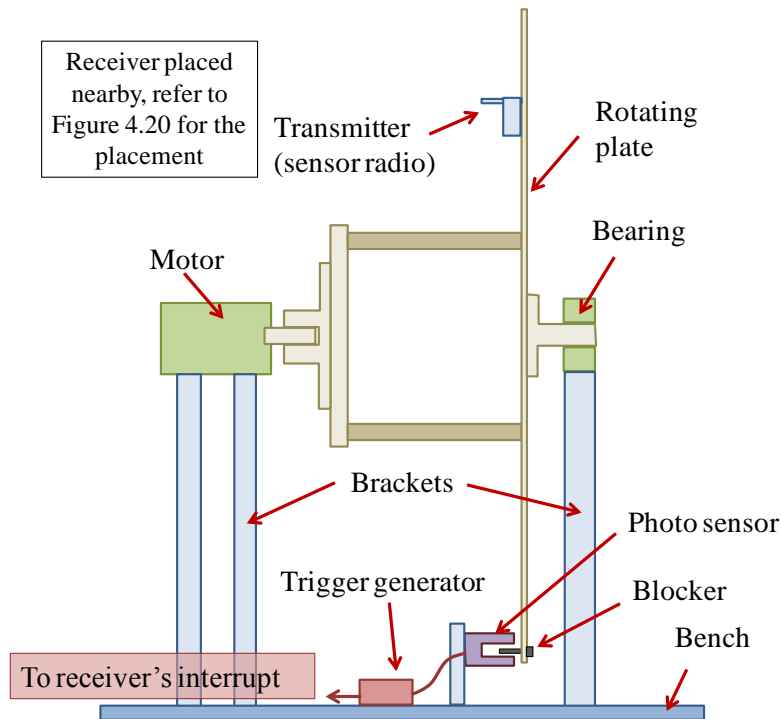
Figure 4.6: Rotating apparatus setup for the sensor radios
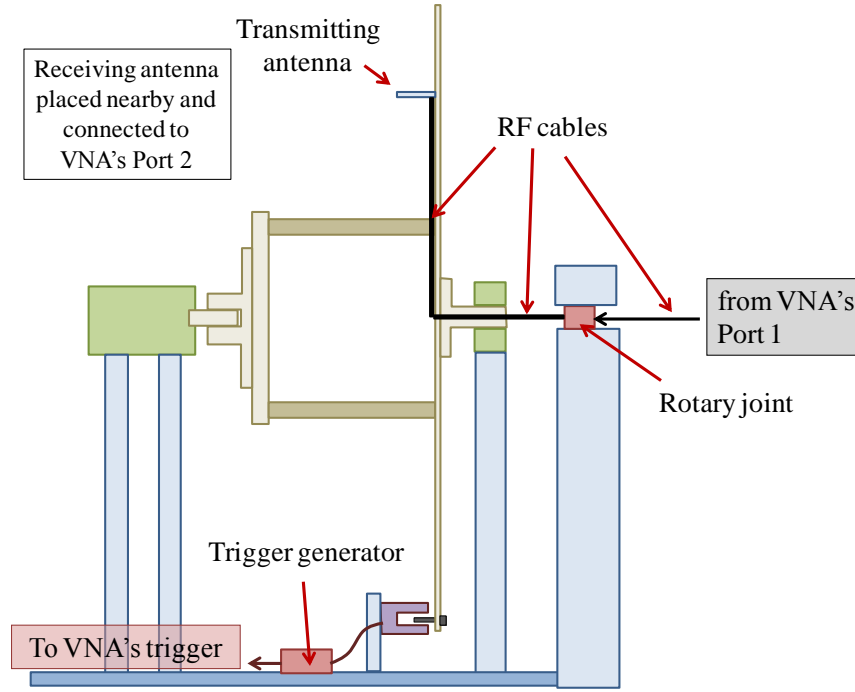
Figure 4.7: Rotating apparatus setup for the VNA

The rotating apparatus was also integrated with an infrared photo-micro sensor, *OMRON EE-SX770*. As shown in Figure 4.6 and 4.7, the photo sensor stood beside the bottom of the rotating plate. A small photo sensor blocker was mounted through one of 360 evenly-distributed holes on a circle near the plate edge, as seen in Figure 8(b). When the blocker passed through the sensor slot and blocked the infrared light, the sensor output was a high voltage (i.e., 12 V); otherwise, the output was a low voltage (i.e., 0 V).

The photo sensor was able to help identify the transmitter location during rotation. Figure 4.8 illustrates how it worked. The photo sensor's location served as an angular reference. After the transmitter and the screw were placed on the rotating plate, their angular distance, θ, was known. The detection of the screw by the photo sensor indicated the screw was on the reference and the transmitter was on θ. At this moment, the photo sensor sent a trigger signal to the VNA or the sensor radio. Upon the trigger, the VNA initiated a measurement, while the sensor radio

recorded the system time specified by the radio's oscillator. The transmitter was fixed on the plate in the experiments, while the blocker can be placed in any of the 360 holes, so that θ was adjustable. In this way, the rotating apparatus was able to locate the rotating transmitter with a 1 ° resolution.

(a) Positioning holes and blocker   (b) Transmitter angular location
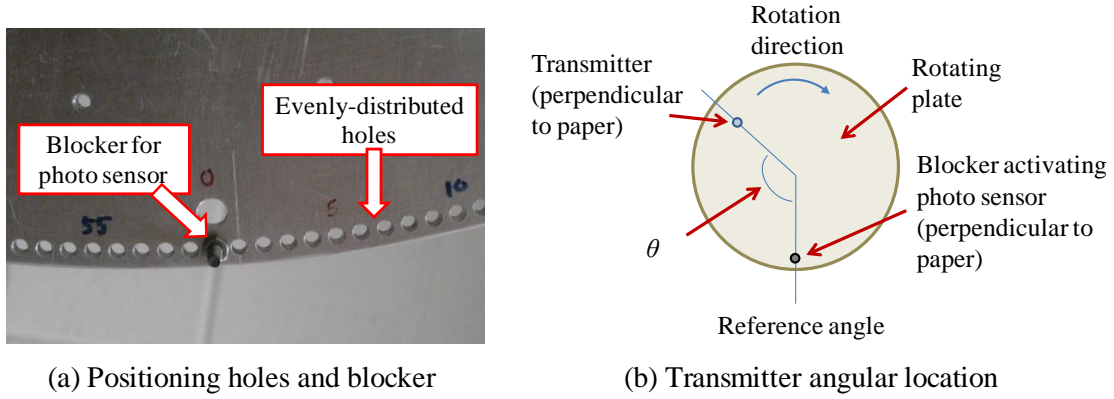
Figure 4.8: Transmitter positioning mechanism

The photo sensor output was a high-to-low (12 V-to-0 V) voltage edge upon the blockage. Additional circuits were needed to generate the appropriate trigger for the VNA and the sensor radio.

The VNA can be triggered by shortening the two ends of the trigger port; hence, the trigger circuit needs to transform the high-to-low voltage edge into an open-to-short status change for the trigger port. As shown in Figure 4.9, an analog switch (MC74HC4066AN of *ON Semiconductor*) was used to implement this function. Additional buffer (CD4049UBCN of *Fairchild Semiconductor*) was added to provide enough current for the analog switch without affecting voltage.

The sensor radio can be triggered by an interrupt which is a falling voltage edge from 3 V to 0 V. It was achieved by simply lowering down the photo sensor output by a voltage divider. Figure 4.10 shows the trigger circuit for the sensor radio.
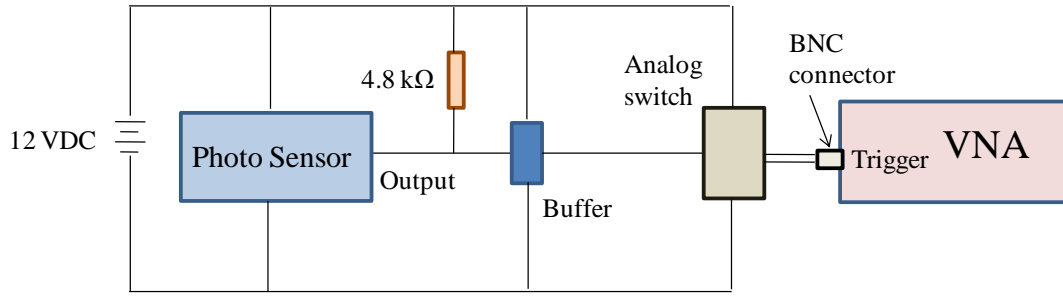
Figure 4.9: Trigger generator for the VNA
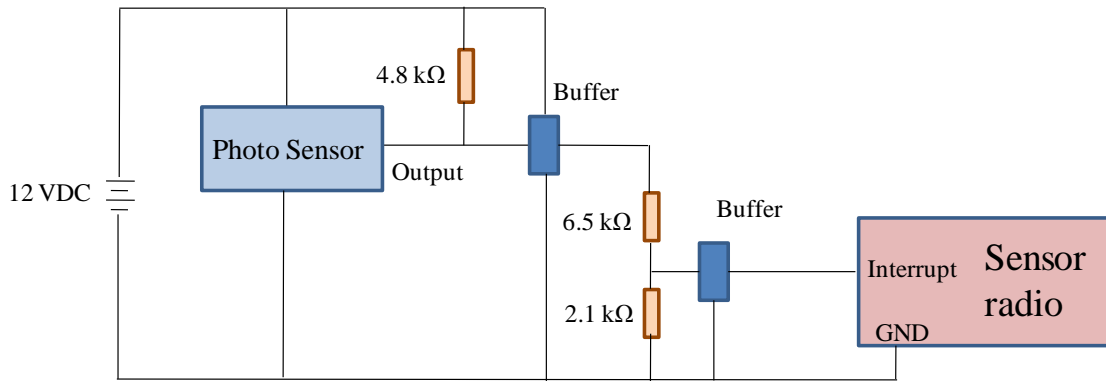
Figure 4.10: Trigger generator for the sensor radio

4.2 Procedure Overview

The PER predictive model consists of three sub-models, and the model validation is performed by individually validating each sub-model. The experimental validation procedure for each sub-model is described as follows:

1. measure the input and output parameters of the sub-model;

2. calculate the predicted output based on the measured inputs and the proposed sub-model;

3. assess the difference between the predicted output and the measured output.

Table 4.1 presents the sub-models, their inputs and outputs and the measurement setups used to validate them.

Table 4.1: Measurement setups to validate individual sub-models in Chapter 3

No.	*Sub-model*	*Measurement setup*
1	Channel multipath profile → Power attenuation sub-model → Power attenuation; Radio frequency ↑	VNA-based setup
2	BER grey area thresholds ↓; Power attenuation → BER sub-model → BER; Transmit power ↑	Sensor radios-based setup
3	Rotation speed ↓; BER(θ) → PER sub-model → PER$_C$; Data rate ↑ Packet length ↑	Sensor radios-based setup

Among the parameters listed in Table 4.1, the data rate of the MICAz motes is fixed to 250 kb/s [MICAz]. Radio frequency, transmit power, and packet length were configured by programming on the sensor radio and will be shown in Table 4.3 in Section 4.3. The following describes the methods for measuring other parameters.

Rotation speed

For the CNC lathe, the spindle rotation speed could be read from the display panel of the lathe. For the rotating apparatus in the chamber, a digital tachometer (*NEIKO* 20713A) was used to measure the speed. The tachometer resolution was 0.1 rpm.

Noise level

The average noise level was measured by a portable spectrum measurement device, *Wi-Spy 2.4x*, from *MetaGeek*. The device is able to measure RF signal power spectrum over the frequency range from 2.400 GHz to 2.495 GHz.

Channel multipath profile

To determine the parameters in Π of a radio channel, the CIR needs to be derived first by measurements. Due to the unavailability of high frequency band pulse generators, the swept frequency method using a VNA was adopted in this study for this purpose. Then, to determine the parameters in Π, the channel's power delay profile (PDP) is derived by transferring the amplitude of the CIR profile into power as

$$p(\tau) = \left| c(\tau) \right|^2 \tag{4.2}$$

The PDP indicates the temporal-distribution of the signal components' powers. The signal components with power above a specified threshold are considered as dominant components, and their time delays and amplitude gains are τ_i's and α_i's in Π.

Power attenuation

Power attenuation was measured by either the VNA or the sensor radios. The VNA can measure channel amplitude gain in dB, the inverse of which gives the power attenuation. With MICAz motes, power attenuation is measured by finding the ratio of transmitted and received power of a transmitted packet, as seen in Equation (3.10).

PER

PER is the fraction of packets lost or containing bit errors among all transmitted packets. Only sensor radios can be used to measure PER. During a measurement, the receiver counts the

successfully received packets among a known number of transmitted packets, and then PER is given by

$$\text{PER} = 1 - \frac{\text{Number of packets successful ly received}}{\text{Number of packets transmitt ed}} \qquad (4.3)$$

Referring to Table 3.1, two types of PER need to be measured in the study:

- $PER_C(\omega)$ is calculated by counting in all packets transmitted during rotation despite their transmission locations.

- $PER_L(\theta, \omega)$ is calculated by only counting in packets transmitted at location θ. For a stationary transmitter, measurements can be performed by simply moving the transmitter to θ. For a rotating transmitter, packets' transmission locations are determined first, and then the packets are grouped based on their locations such that $PER_L(\theta, \omega)$ can be calculated for each θ. The method is detailed in Section 4.3.2.2.

BER

BER is the fraction of bits lost or incorrect among all transmitted bits. However, it cannot be directly measured since some packets with only part of their bits in error may be dropped entirely by the receiver, leaving no information about the number of bits that are truly in error. If the radio channel is static, an alternative way is to calculate BER from its corresponding PER. In this case, the error rate of any bit in one packet is identical, and, therefore,

$$\text{PER} = 1 - (1 - \text{BER})^n \qquad (4.4)$$

where n is the number of bits in the packet. Thus

$$\text{BER} = 1 - (1 - \text{PER})^{\frac{1}{n}} \qquad (4.5)$$

This method is not applicable to derive BERs for a rotating transmitter, since the channel continuously changes and each bit has an individual error rate.

In Table 3.1, $BER(\theta)$ refers to the BER of the stationary transmitter at θ and is calculated from $PER_L(\theta,0)$ by Equation (4.5). According to the BER consistency assumption described in Section 3.1, the BER is valid for the same location for rotating transmitter scenarios.

BER grey area thresholds

As defined in Section 3.2.3, the BER grey area refers to the range of received power which causes BER to vary radically. The grey area is around radio's receiving sensitivity. The typical sensitivity level is usually provided by radio manufacturers; yet, the BER grey area thresholds P_{GH} and P_{GL} are radio-dependent. For each radio, the thresholds can be experimentally identified. Without loss of generality, this dissertation considers this range as the maximum power range in which BERs at the same received power may have a variation larger than 0.001.

4.3   Experiment Design

Table 4.2 lists the experiment scenarios in terms of the environments, the measurement setups, the transmitter motion status, and their main purposes. The rest of this section presents each scenario in detail.

Table 4.2: Experiment scenarios and their main purposes

Environment	Measurement setup	Transmitter status	Main Purpose
CNC lathe	Sensor radios	Stationary and rotating	Validate the PER sub-model (sub-model 3).
	VNA	Stationary	Validate the signal power attenuation sub-model (sub-model 1).
Anechoic chamber	Sensor radios	Stationary and rotating	Validate the BER sub-model (sub-model 2) and the PER sub-model (sub-model 3).
	VNA	Stationary and rotating	Validate the model hypotheses.

4.3.1 Experiments using CNC Lathe Spindle

4.3.1.1 Sensor Radio Experiments

Figure 4.11 illustrates the functional structure of the sensor radio-based setup in the CNC lathe. The system utilized three MICAz motes and a MIB510. Two motes served as a transmitter and a receiver for the link of interest, which was evaluated by transmitting probes with known data pattern. The third mote, functioning as a base station, was responsible for transmitting commands and receiving records. Via MIB510, the base station was connected with a PC through a UART–USB adaptor. A MATLAB program on the PC performed measurement control, data analysis and data storage.
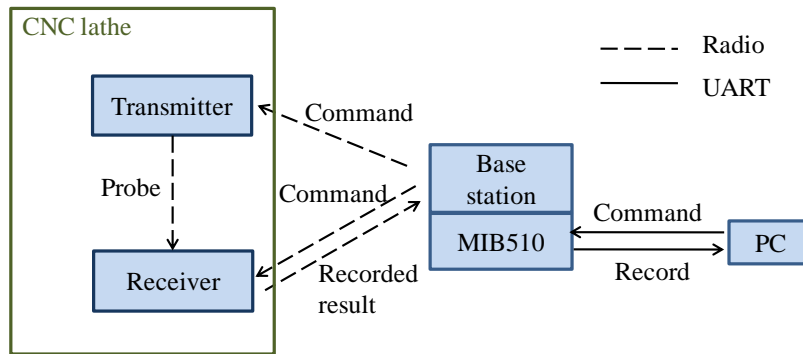
Figure 4.11: Structure of the sensor radio-based setup in the CNC lathe

Figures 4.12 illustrate the dimension of the CNC lathe and the placement of the sensor radios. The transmitter was safely mounted on the lathe spindle by duct tape, and the receiver was deployed on the inner-wall of the lathe. During the experiments, the machine window was closed, and no people or other objects were allowed in the room.
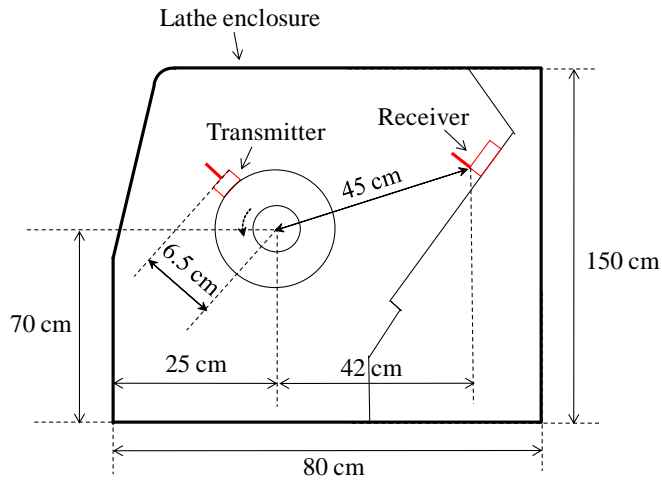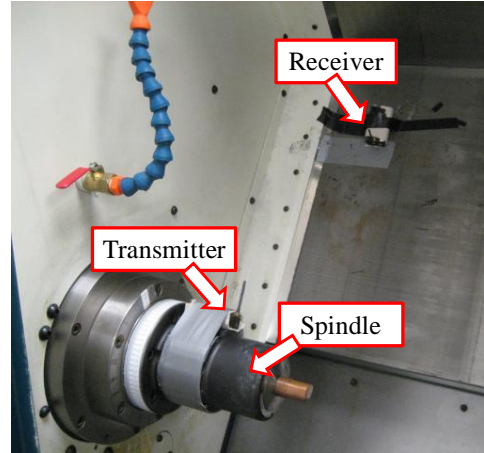
(a) Dimension schematic   (b) Photo of sensor radios in CNC lathe

Figure 4.12: Placement of the sensor radio-based setup in the CNC lathe

Table 4.3 lists the key settings on the MICAz motes. Channel 26 was chosen because previous measurements showed the power of noise and interferences was consistently low at this frequency range in the CNC lathe. Two transmit power (0 dBm and -25 dBm) were used, respectively. In the stationary transmitter experiments, the number of probe packets for one transmitter location was at least 2000; if the PER was larger than 0.1, 15000 packets were transmitted for extra measurements to have a more precise result.

Table 4.3: Major configurations on the sensor radio-based setup

Configuration	*Setting*	
Frequency	2478.5 ~ 2481.5 MHz (i.e., Channel 26)	
Transmit power	0 dBm and -25 dBm	
Packet length	90 bytes	
Number of probe packets	Stationary transmitter	2000 or 15000
	Rotating transmitter	5000 per round, 3 rounds

Table 4.4 lists the parameters that can be measured by the sensor radio-based setup in the CNC lathe. For the sensor radio's security, the highest speed was 1993 rpm, of which the equivalent linear speed is 13.5 m/s.

Table 4.4: Parameters measured by the sensor radio-based setup in the CNC lathe

Measured parameter	Transmitter status	Note
$PER_C(\omega)$	Rotating	Speeds: 60, 302, 544, 786, 1027, 1208, 1510, 1752, and 1993 rpm.
$PER_L(\theta, 0)$	Stationary	$0° \leq \theta < 360°$, resolution: $1°$
$PA_L(\theta)$	Stationary	$0° \leq \theta < 360°$, resolution: $1°$

Figure 4.13 depicts the experiment steps. At the beginning, the base station sent a command to both the transmitter and the receiver to set transmission parameters such as the transmit power, the size and number of probe packets, the interval between two successive transmissions, and the measurement delay if needed. The acknowledgement function on the transmitter and the receiver was disabled during the experiment. After a preset delay for the CNC lathe to reach steady speed, the transmitter starts transmitting probe packets to the receiver with incrementing identification (ID) numbers. For each received probe packet, the receiver stored CRC check byte, RSSI, and receiving time in its flash memory. If the packet passed the CRC check, the receiver also stored its ID number. After the experiment, the stored information in the receiver was sent to the base station and relayed to the PC for analysis and permanent storage.
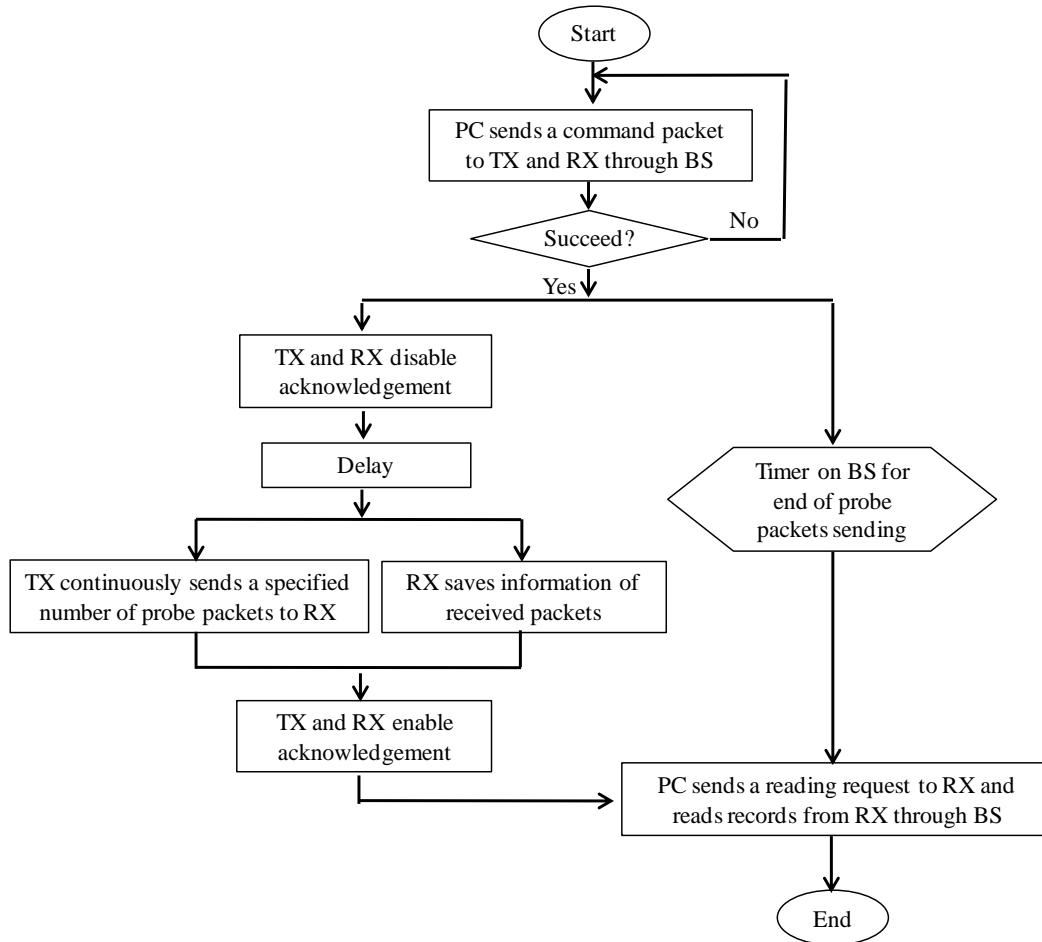
Figure 4.13: Flowchart of sensor radio measurements in the CNC lathe

(TX: transmitter, RX: receiver, BS: base station)

4.3.1.2 VNA Experiments

Figure 4.14 illustrates the structure of the VNA-based measurement setup in the CNC lathe. The transmitting antenna and the receiving antenna were connected to Port 1 and Port 2 of the VNA respectively through RF cables without radios involved. By setting the measured S-parameter to S_{21}, Port 1 exports signal, (which is called incident signal), into the channel; Port 2 imports signal, (which is called transmitted signal), from the channel. S_{21} is the complex transmission coefficient describing the amplitude and the phase of the transmitted signal relative to the incident signal [VNABasics].
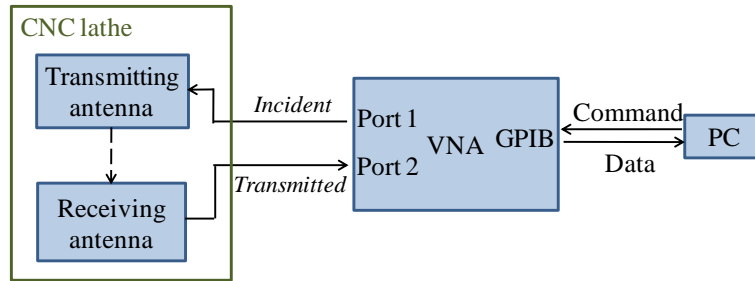
Figure 4.14: Structure of the VNA-based setup in the CNC lathe

To correct systematic errors, the VNA was calibrated after the measurement parameters were chosen and the RF cables were setup but before the two antennas were connected [HP8714]. The calibration procedure consisted of two steps: 1) used a "through" connector in a HP VNA calibration kit (model 85052B) to connect the cables such that a signal loop from Port 1 to Port 2 was generated; 2) pressed the "calibration" button on the VNA panel and then selected "response" on the VNA screen to start the automatic calibration. The VNA could prompt a message to indicate the calibration completeness. Then, the "through" connector was replaced with the two antennas, and the setup was ready for measurements. If any measurement parameter or RF cable changed, the calibration needed to be performed again.

The locations of the transmitting antenna and the receiving antenna in the CNC lathe were the same as shown in Figure 4.12(a). Figure 4.15 is a photo showing their placement.
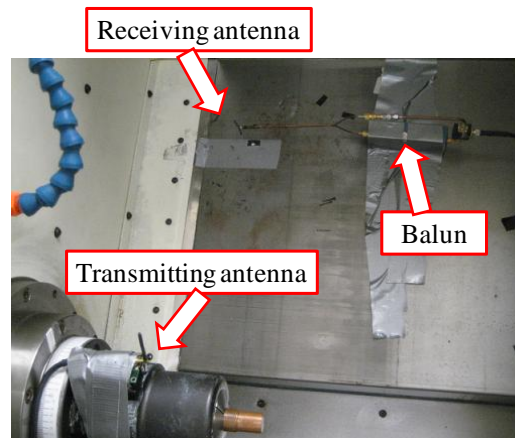
Figure 4.15: Antenna placement of the VNA-based setup in the CNC lathe

56

The VNA can measure the frequency response in a broadband or at a single frequency. The broadband frequency response was used to calculate CIR, and the single frequency response was to calculate power attenuation. Table 4.5 summarizes the parameters that were measured by the VNA-based setup in the CNC lathe.

Table 4.5: Parameters measured by the VNA-based setup in the CNC lathe

Measured parameter	Note
$FR(\theta, 0)$	The transmitter was stationary.
$PA_L(\theta, 0)$	$0\,° \leq \theta < 360\,°$, and its resolution was $1\,°$

The key settings of the VNA are listed in Table 4.6. For the broadband frequency response measurements, the number of measurement points refers to the number of frequencies the VNA scans; for the single frequency measurements, it refers to the number of repeated measurement samples.

Table 4.6: Major configurations on the VNA-based setup in the CNC lathe

Configuration	Setting	
Frequency	Broadband	300 kHz ~ 3 GHz
	Single	2.48 GHz
Number of measurement points	801	
Transmit power	7 dBm	
Measured S-parameter	S_{21}	
Trigger source	Internal	
Trigger mode	Single	
Intermediate frequency (IF) bandwidth	Fine (i.e., 15 Hz)	

The minimum received power level a VNA can measure is set by the VNA's noise floor. A general rule is the received power is at least around 10 dB above the noise floor. It can be achieved by increasing the transmit power or reducing the noise floor. For a given VNA, the

noise floor can be reduced by narrowing the IF bandwidth [VNADynamic]. For our measurement setup in the CNC lathe, the highest transmit power and the narrowest IF bandwidth were chosen so that the received power was at least 20 dB above the noise floor.

When calculating the CIR from a frequency response, the frequency band and the number of points determine CIR's time resolution and time span. To achieve the finest time resolution, the largest frequency band (300 kHz ~ 3 GHz) was chosen. The detailed calculation of the time resolution will be presented later. The time span is the reciprocal of the frequency resolution. Given the point number and the frequency band in Table 4.6, the frequency resolution is 3749.625 kHz, resulting in the CIR's time span of about 267 µs. Preliminary test had proved the received signals had attenuated to a very low power level in this time span, so it's assumed that all strong signals were present in the calculated CIR.

After the VNA calibration, the following figure shows the experiment steps for the stationary transmitter at each location. The steps were repeated for different locations on the spindle periphery.

Step 1	Place the transmitter to the location of interest by manually rotating the spindle.
Step 2	Close the CNC window.
Step 3	Run the LabVIEW program, which sequentially: 1. starts a single measurement by setting VNA's trigger source to "Internal" and trigger mode to "Single". *If measuring broadband, VNA continuously measures the response over all frequencies.* *If measuring single frequency, VNA continuously measures the response at the frequency.* 2. sets a timer to report when the measurement is over. 3. reads measurement data from VNA back to PC, once the time is out.

Figure 4.16: VNA measurement steps for the stationary transmitter in the CNC lathe

CIR time resolution and Π derivation

CIR is calculated from measured frequency response. To generate a real-number impulse response after the IDFT calculation, a conjugate symmetric series is created by taking the conjugate mirror of the frequency response about 0 Hz, and then the IDFT is applied on the new series to derive the CIR.

The time resolution of an impulse response is defined as the minimum time duration in which a signal value can be recognized. For the impulse response derived by IDFT, the time resolution is computed by

$$t_r = c \times \frac{1}{F} \tag{4.6}$$

where t_r is the time resolution, F is the bandwidth of the frequency response, and c depends on the type of the window function applied to the frequency response. For a rectangular window function, c is 1. The advantage of using a rectangular window is it can achieve the best possible time resolution, since for any other window function, c is greater than 1. In this study, the frequency response was measured from 300 kHz to 3 GHz, and the window function was the rectangular window, resulting in that t_r is 0.3334 ns.

The time interval is defined as the interval between two consecutive points of an impulse response. Its calculation is expressed by

$$\Delta t = \frac{T}{N_t} \tag{4.7}$$

where N_t is the point number of the impulse response, and T is the response's duration, which is determined as the following equation in which f_r is the frequency resolution of the measured frequency response.

$$T = \frac{1}{f_r} \tag{4.8}$$

The point number of the conjugate symmetric series is as twice as that of the original measured frequency response, denoted as N_f. So is the point number of the impulse response after it goes through the IDFT, i.e., $N_t = 2N_f$. Meanwhile, since $F = f_r \times N_f$, we have

$$\Delta t = \frac{T}{f_r \times 2N_f} = \frac{1}{2F} = 0.5 t_r \qquad (4.9)$$

This means there are two data points in one time resolution duration. To conform to the time resolution, the impulse response series is down-sampled by skipping one every two points. This step results in the final impulse response.

Given an impulse response, the PDP is obtained as in Equation (4.2). Multipath components are identified from the PDP. In this process, the PDP data are screened using a specified threshold, which is H dB below the highest peak, and any data point higher than the threshold is considered as an individual multipath component. H is an empirical parameter and usually set to 5, 10, 15, or 20 dB. [Abouraddy1998] concluded a threshold more than 10 dB had little effect on RMS delay spread, suggesting it is a good tradeoff between ruling out noise and correctly identifying strong components. 15 dB was selected in this study. Figure 4.17 gives an example of a PDP in the CNC lathe and the identified multipath components.
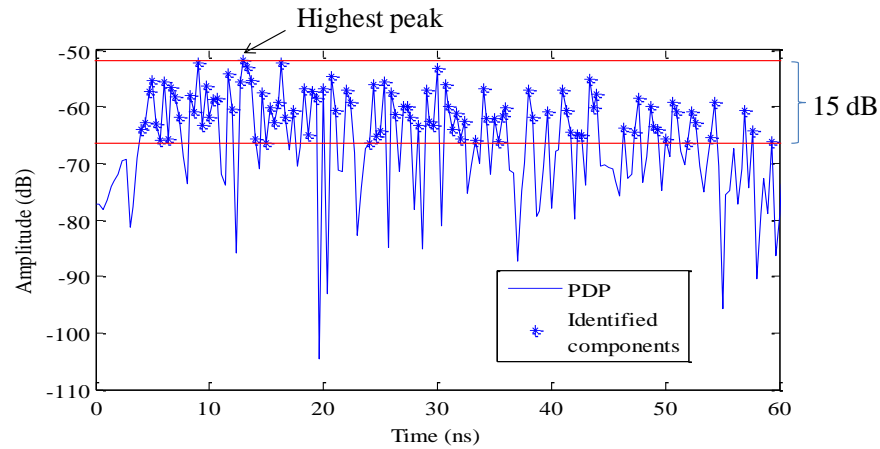
Figure 4.17: A PDP in the CNC lathe and the identified multipath components

60

4.3.2 Experiments using Rotating Apparatus in Anechoic Chamber

4.3.2.1 Anechoic Chamber

The anechoic chamber is located at the Clemson University Ravenel Research Park. Figure 4.18 is a photo of the chamber interior. The inner wall is covered with microwave absorbers, EHP-18PCL from *ETS Lindgren*. The absorber's typical reflectivity in the 2~4 GHz band is -50 dB [ETS-LINDGREN]. The rotating apparatus was placed on the walkway. A metallic antenna positioner for other measurement purposes was in the middle of the chamber; to eliminate its effects on radio signals, it was covered with absorbers too.
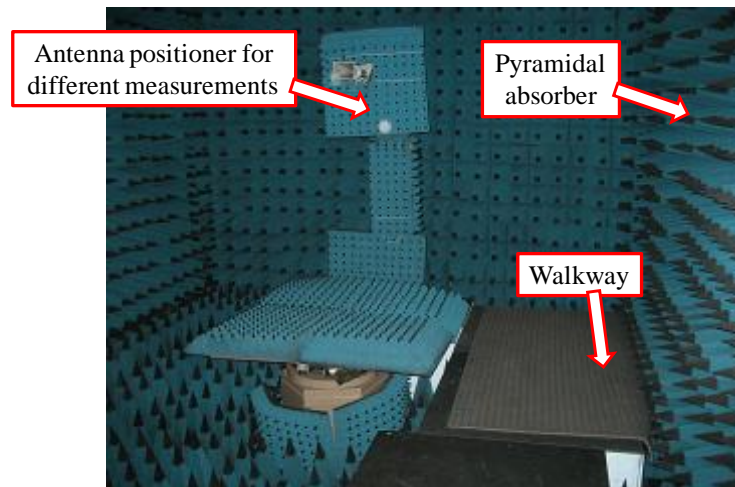
Figure 4.18: Photo of the anechoic chamber interior

The purpose of performing the rotating apparatus experiments in the chamber was to avoid unpredictable and uncontrollable multipath effects and interferences. Since the apparatus was made of metallic parts, the multipath effects were still present. However, as long as the transmitter and receiver placement was fixed, the channel multipath profiles were repeating during the transmitter rotation.

4.3.2.2 Sensor Radio Experiments

As shown in Figure 4.19, the setup only utilized two MICAz motes as the transmitter and the receiver without the base station. The transmitter was placed on the rotating plate. The receiver was plugged on the MIB510, which was further connected to the PC by the UART-USB adaptor through a port on the chamber wall, such that the receiver can directly transfer measured data to the PC during probe packet transmission. This was due to additional sensor position data requiring storage space larger than the receiver's on-board memory. The experimenter stayed outside and controlled the measurements by the PC.
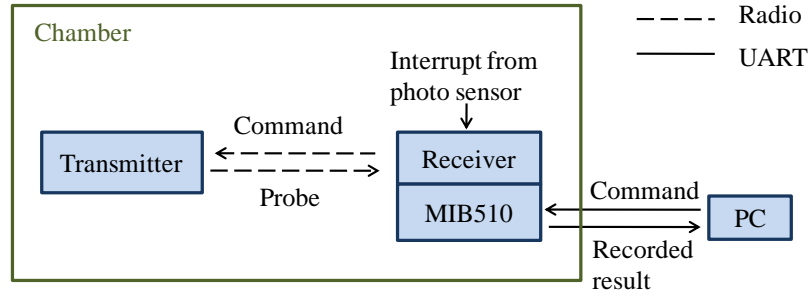
Figure 4.19: Structure of the sensor radio-based setup in the chamber

Figure 4.20(a) shows the dimension of the transmitter and receiver placement on the rotating apparatus in the chamber. The transmitter was safely mounted on the rotating plate by duct tapes, and the receiver was placed on an absorber nearby. Figure 4.20(b) shows a photo of the setup in the chamber.

The sensor radio configuration was the same as listed in Table 4.3. Table 4.7 lists the parameters that can be measured or derived from the experiment results. For the stationary transmitter experiments, the transmitter location resolution of $PER_L(\theta, \omega)$ and $PA_L(\theta, \omega)$ was 5 °in the regions where PERs were below 0.1 and 1 °in the regions where PERs were above 0.1. For the rotating transmitter experiments, $PER_L(\theta, \omega)$ and $PA_L(\theta, \omega)$ were calculated and the method will be presented later.
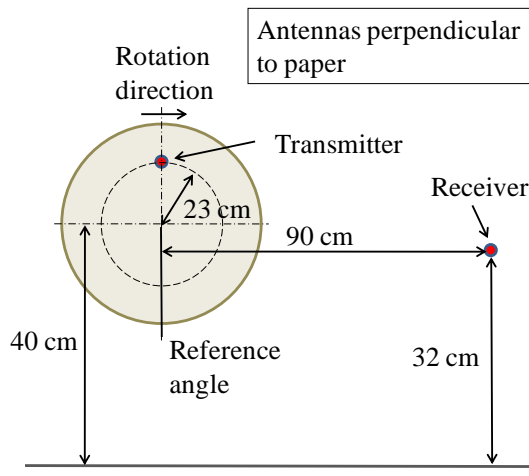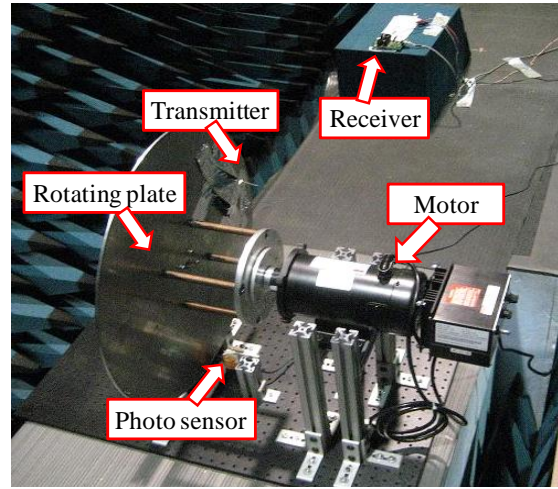
(a) Dimension schematic   (b) Photo of the setup

Figure 4.20: Placement of the sensor radio-based setup in the chamber

Table 4.7: Parameters measured or derived from the sensor radio-based setup in the chamber

Measured parameter	Transmitter status	Note
$PER_C(\omega)$	Rotating	Speeds: 50, 97, 150, 202, 252, 302, and 360 rpm.
$PER_L(\theta, \omega)$	Stationary	$0\,° \leq \theta < 360\,°$ resolution: 5 ° or 1 °
	Rotating	Same speeds as above.
$PA_L(\theta, \omega)$	Stationary	$0\,° \leq \theta < 360\,°$; resolution: 5 ° or 1 °
	Rotating	Same speeds as above.

Figure 4.21 depicts the experiment procedure, which is generally the same as the experiments in the CNC lathe. The major difference is that a memory buffer was used in the receiver to temporarily save the information of received probe packets. Whenever the buffer was full the receiver sent the data to the PC, even when the probe packet transmission was still ongoing.
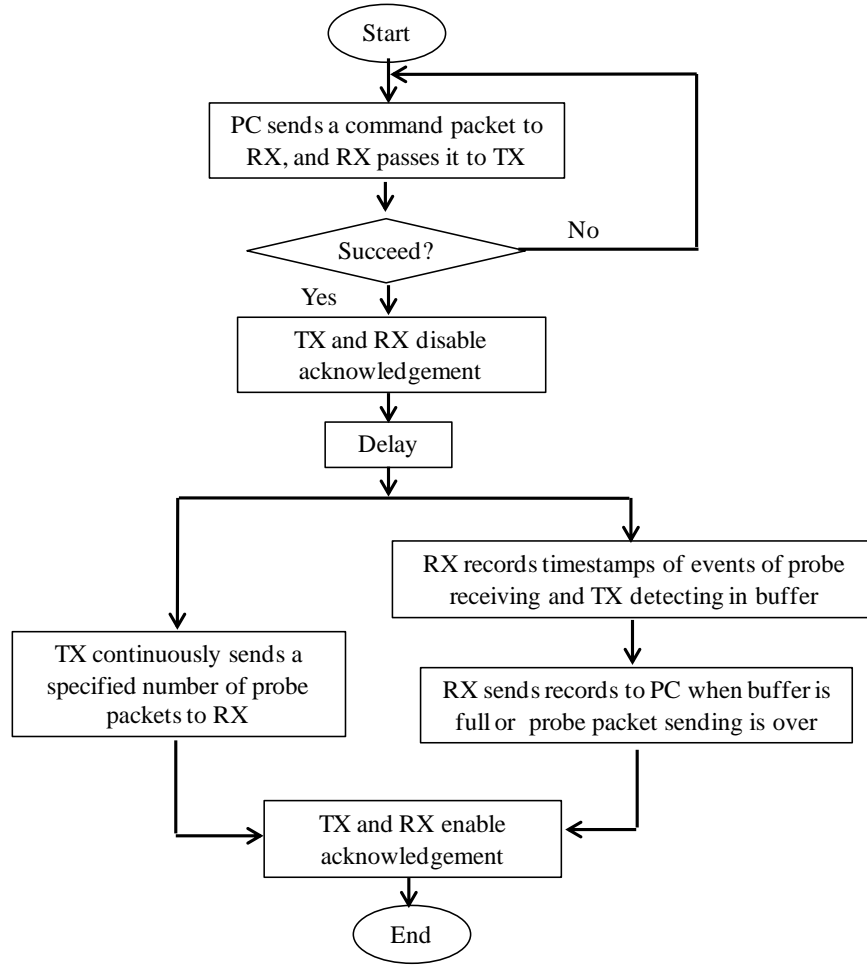
Figure 4.21: Flowchart of the sensor radio measurement in the chamber

(TX: transmitter, RX: receiver)

Calculation of $PA_L(\theta, \omega)$ and $PER_L(\theta, \omega)$

In the rotating transmitter experiments, the timestamps of received probe packets have been recorded. Because of the extremely fast propagation speed of radio signals and small distance between the transmitter and the receiver, the packets' receiving times are close to their transmitting times. Since the received packets' IDs were known, it could be determined whether or not there were lost packets between two consecutively received packets, and, if any, how many were lost. The transmitting times of the lost packets were estimated assuming them as evenly

distributed between two received packets right before and after them. Therefore, the transmitting time of any packet is derived.

Meanwhile, the times of the transmitter passing the reference location have been recorded as well. With this timing information and the rotation speed of ω, the transmitter location of each probe packet was calculated. The packets were grouped into 2°-wide spatial bins. Based on packets in each bin, $PA_L(\theta, \omega)$ and $PER_L(\theta, \omega)$ are able to be calculated.

4.3.2.3 VNA Experiments

Figure 4.22 illustrates the VNA-based setup in the chamber. The transmitter and receiver placement was the same as shown in Figure 4.20.
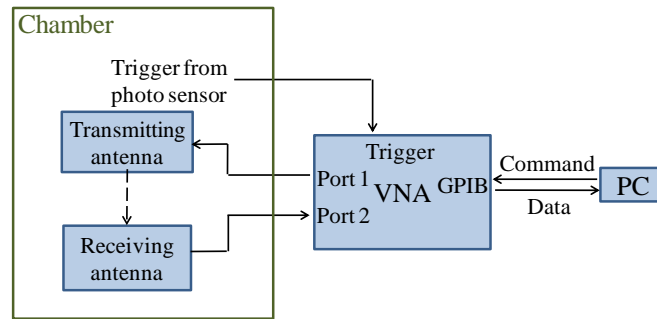
Figure 4.22: Structure of the VNA-based setup in the chamber

Frequency responses and signal power attenuations could be measured for both stationary and rotating transmitter scenarios. To avoid damaging the photo sensor and the transmitter, the highest rotation speed was set to 300 rpm, and the equivalent linear speed was 7.2 m/s. Table 4.8 summarizes the parameters that were measured by the VNA-based setup in the CNC lathe.

Table 4.8: Parameters measured by the VNA-based setup in the chamber

Measured parameter	Note
$FR(\theta, \omega)$	The transmitter was stationary or rotating at 100 rpm, 200 rpm, or 300 rpm. $0° \leq \theta < 360°$; and the resolution was 5°.
$PA_L(\theta, \omega)$	

In rotating transmitter experiments, to measure instantaneous channel properties when the transmitter passed by an interested location, the VNA swept frequencies in a point-wise way. In this method, only one frequency was measured upon one transmitter's passing, and all frequencies were measured one by one. Figure 4.23 demonstrates the procedure. To achieve this measurement, the VNA's trigger source and trigger mode were set to "External" and "Point."
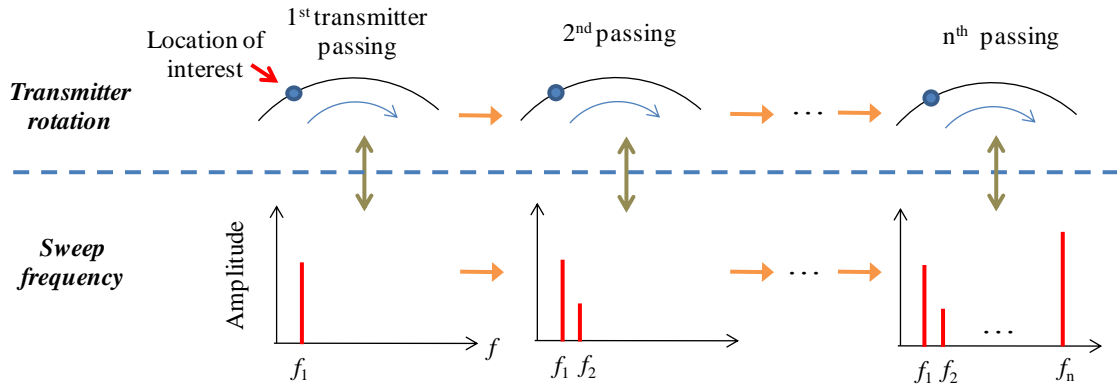
Figure 4.23: VNA sweep frequency method for the rotating transmitter scenario

The period in which the VNA measures one frequency is called data taking time. In rotating transmitter experiments, the data taking time must be as short as possible such that the channel has insignificant change. On one hand, the data taking time is approximately the reciprocal of the IF bandwidth, so a broad IF bandwidth is preferred; on the other hand, a broader IF bandwidth leads to a higher noise floor. Choosing the IF bandwidth is a tradeoff between the data taking time and the noise floor.

For our measurement setup in the chamber, the transmit power was the highest (7 dBm) and the IF bandwidth was carefully chosen to be "Medium Narrow" so that the noise floor was about 10 dB lower than the received power. The corresponding data taking time was 0.8333 ms, and the transmitter travelling ranges in this duration were indicated in Figure 4.24 for the three rotation speeds. Consequently, measured frequency responses or power attenuations were integrated results with the transmitter travelling in the ranges.

66
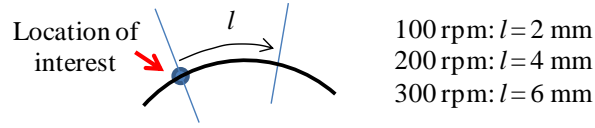
Figure 4.24: Transmitter travelling range in a data taking time

Table 4.9 lists the settings for major VNA configurations. Due to the limited time of chamber access, the number of measurement points was set to 401 to save time. The corresponding frequency interval was 7499.25 kHz and the CIR time span was about 133 μs. Preliminary test in the chamber had proved no strong signals arrived at the receiver after the span.

Table 4.9: Major configurations on the VNA-based setup in the chamber

Configuration	*Setting*		
Frequency	Broadband		300 kHz ~ 3 GHz
	Single		2.48 GHz
Number of measurement points	401		
Transmit power	7 dBm		
Measured S-parameter	S_{21}		
Trigger source	Stationary transmitter		Internal
	Rotating transmitter		External
Trigger mode	Stationary transmitter		Single
	Rotating transmitter		Point
IF bandwidth	Medium narrow (i.e., 1200 Hz)		

After the VNA calibration, Figure 4.25 demonstrates the experiment steps in the stationary transmitter experiment for one particular location. The same steps are repeated for all other transmitter locations. Figure 4.26 demonstrates the experiment steps in the rotating transmitter experiment for one particular transmitter location and one particular rotation speed. The same steps are repeated for other locations and speeds. All measurement results will be presented in Chapter 5.

| Step 1 | Place the photo sensor blocker in a hole to make the angle between the blocker and the transmitter be the interested. |

⬇

| Step 2 | Manually rotate the plate until the screw is in the photo sensor slot. |

⬇

| Step 3 | Close the chamber door. |

⬇

| Step 4 | Run the LabVIEW program, which sequentially:

1. starts a measurement by setting VNA's trigger source to "Internal" and trigger mode to "Single".

2. sets a timer to report when the measurement is over.

3. reads measurement data from VNA back to PC, once the time is out. |

Figure 4.25: VNA measurement steps for the stationary transmitter in the chamber

| Step 1 | Place the photo sensor blocker in a hole to make the angle between the blocker and the transmitter location be the interested. |

⬇

| Step 2 | Run the motor and tune it to the speed of interest. |

⬇

| Step 3 | Close the chamber door. |

⬇

| Step 4 | Run the LabVIEW program, which sequentially:

1. starts a measurement by setting VNA's trigger source to "External" and trigger mode to "Point".

If measuring FR, VNA measures the response for one frequency upon one triggering and measures for next frequency upon next triggering until all frequencies are scanned.

If measuring PA at a single frequency, VNA repeats measure for the same frequency upon triggering until the repeat time is achieved.

2. sets a timer to report when the measurement is over.

3. reads measurement data from VNA back to PC, once the time is out. |

Figure 4.26: VNA measurement steps for the rotating transmitter in the chamber

4.4   Summary

This chapter presented the details of the experiments for model validation. Two measurement setups were designed: a sensor radio-based setup for measuring PER and a VNA-based setup for deriving channel multipath profile. Two rotating structures were introduced: a CNC lathe spindle and a rotating apparatus, which can help measure instantaneous channel properties. The chapter also described experiment steps and data processing methods. Based on collected experimental data, the sub-model validation are ready to be performed in the following chapter.

Chapter 5

PER Predictive Model Validation

In this chapter, the PER predictive model is validated with the measurement experiments presented in Chapter 4. The difference between predicted and measured outcomes of each sub-model is examined. Each sub-model's sensitivity to key inputs is discussed. The implications of the VNA's limited time accuracy on the power attenuation sub-model are discussed. The calculation of the uncertainty for a predicted PER_C is also presented.

5.1   Validation of Model Hypotheses

The validation of the model hypotheses described in Chapter 3 requires the rotating transmitter's channel frequency response and power attenuation. The VNA measurements in the chamber provide data for the validation. The measurement procedures and the data processing methods were presented in Section 4.3.2.3.

Hypothesis 1: *Within the speed range attainable in the study, RMS delay spreads of all transmitter locations are small and cause no significant ISI-induced errors despite transmitter rotation.*

Figure 5.1 shows the RMS delay spreads on the circular route for the stationary and rotating transmitter scenarios. The equivalent linear speeds of 100 rpm, 200 rpm, and 300 rpm are 2.4 m/s, 4.8 m/s, and 7.2 m/s respectively. The figure shows the RMS delay spreads were from

70

0.5 ns to 3.5 ns, and, according to Equation (2.7), the normalized-RMS delay spreads were on the level of 10^{-4} for the CC2420 radios. Based on the simulation in [Chuang1987], for the OQPSK-modulated CC2420 radios, the ISI-induced BER is approximately on the level of 10^{-8}. This proves the ISI-induced BER in the chamber was extremely small to cause significant errors with the speed below 7.2 m/s.
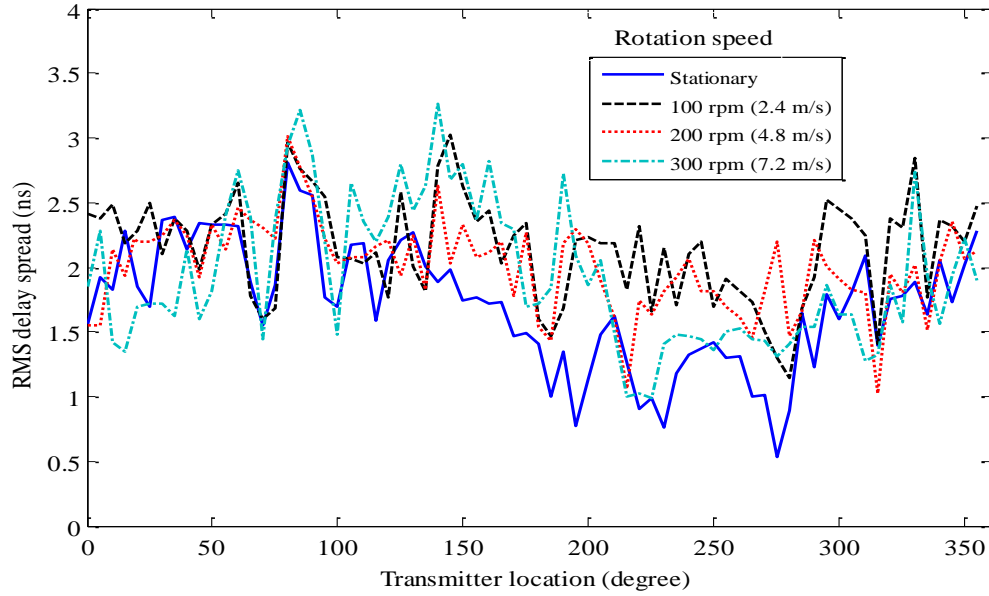
Figure 5.1: RMS delay spread in the chamber

With the stationary scenario as the reference, Table 5.1 lists the averages and the standard deviations of the differences from other speeds' RMS delay spread profiles, as well as the maxima of the absolute differences. With the CIR time resolution of 0.3334 ns, the average differences at 200 rpm and 300 rpm could be considered as zero, and the average at 100 rpm is extremely small too. One concludes that the transmitter rotation has little effects on RMS delay spreads in this speed range.

Table 5.1: Statistics of RMS delay spread differences

Speed	Average of differences	Standard deviation of differences	Maximum of absolute differences
100 rpm (2.4 m/s)	0.4372 ns	0.4157 ns	1.43 ns
200 rpm (4.8 m/s)	0.2953 ns	0.4255 ns	1.67 ns
300 rpm (7.2 m/s)	0.2362 ns	0.4980 ns	1.38 ns

In the CNC lathe, the RMS delay spreads for the stationary transmitter were measured between 13 ns and 25 ns, and the corresponding ISI-induced BER was approximately on the level of 10^{-6}. Although it's impossible to measure RMS delay spreads for the rotating transmitter in the CNC lathe, based on the observations in the chamber, they have little changes for the speed below 7.2 m/s (equivalently 1061 rpm for the CNC lathe); hence, the hypothesis is valid for this speed range.

For the speed from 7.2 m/s to 13.5 m/s (equivalently 1993 rpm), it's expected that the hypothesis is still true, without a full validation though. This will be indirectly proved by testing the BER consistency assumption, which was inferred from the hypotheses in Section 3.1, during the PER sub-model validation in Section 5.2.3.

Hypothesis 2: *Within the speed range attainable in the study, power attenuation of each transmitter location is not affected by transmitter rotation.*

Figure 5.2 plots the VNA-measured 2.48 GHz signal power attenuation on the measured transmitter locations for the stationary and rotating transmitter scenarios. The four profiles have good match with each other.

With the stationary scenario as the reference, Table 5.2 lists the averages and the standard deviations of the differences from other speeds' power attenuation profiles, as well as the maxima of the absolution differences. The small differences prove the hypothesis is true for the speed

72

below 7.2 m/s. Similar to Hypothesis 1, this hypothesis is expected to be true for the speed from 7.2 m/s to 13.5 m/s and will be indirectly proved in Section 5.2.3.
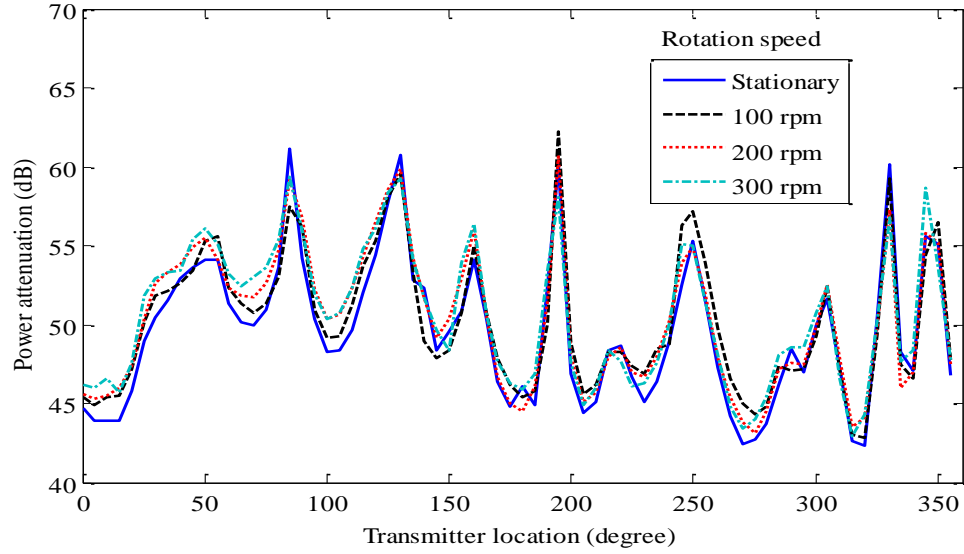
Figure 5.2: Power attenuation in the chamber

Table 5.2: Statistics of power attenuation differences

Speed	Average of differences	Standard deviation of differences	Maximum of absolute differences
100 rpm (2.4 m/s)	0.60 dB	1.32 dB	3.75 dB
200 rpm (4.8 m/s)	0.78 dB	1.12 dB	2.89 dB
300 rpm (7.2 m/s)	1.02 dB	1.33 dB	3.35 dB

5.2 Validation of Sub-models

5.2.1 Signal Power Attenuation Sub-model

5.2.1.1 Validation

Given a radio channel multipath propagation profile and the signal carrier frequency as inputs, this sub-model predicts the resulting power attenuation of the signal received on the other

end of the channel. While the model can be used for different frequencies, this dissertation only considers 2.48 GHz, which is one of the supported carrier frequencies for IEEE 802.15.4 radios.

In the CNC lathe as well as the chamber, the VNA experiments measured both the channel multipath profile and the corresponding power attenuation for different transmitter locations on the rotation route. With these measurements, the following validation procedure leads to three conclusions:

- The adopted VNA's time resolution for channel profile measurement (0.3334 ns) is too coarse for accurate power attenuation prediction.

- However, given the VNA resolution, it is shown the difference between the predicted and measured power attenuation lies within a range dictated by the VNA time resolution, though the range can be quite large for the resolution of 0.3334 ns.

- The above observations suggest that while predicting power attenuation from multipath profile is possible and its accuracy potentially improves with VNA's time resolution, practical systems may choose to bypass this prediction stage and measure the power attenuation using the sensor radios directly.

Since radio channel changes when the transmitter moves (the receiver is at a fixed location), the prediction is done and validated with the transmitter at each of the 360 different locations. Figure 5.3 shows the measured and predicted power attenuation for all transmitter locations. The key difference between Figure 5.3(a) and (b) is that, (a) is the prediction based on τ_i's extracted directly from VNA measured CIR, while (b) is the prediction with τ_i's post-processed as follows.

Larger than the half period of a 2.48 GHz signal (0.2016 ns), the CIR time resolution (0.3334 ns) is too coarse to accurately identify τ_i's. Hence, such τ_i's cannot accurately predict power attenuation profile. To prove that, accurate prediction is possible if τ_i's are accurate, a

sequential quadratic programming method was used to fine tune τ_i's such that the power attenuation profile best matches the measured one. Figure 5.3(b) shows a close match with maximum difference of 0.001 dB achieved with τ_i adjustments within the VNA time resolution. The following discusses the adjustment procedure.
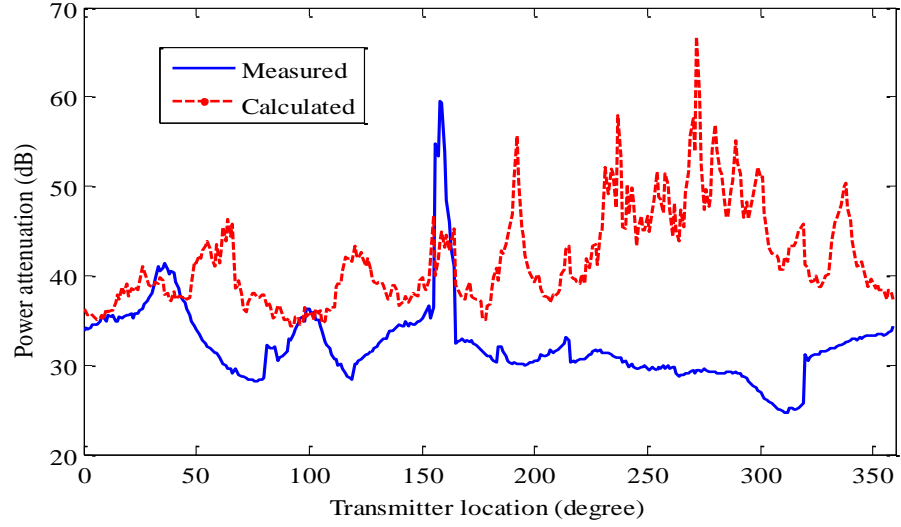
(a) without τ_i adjustment
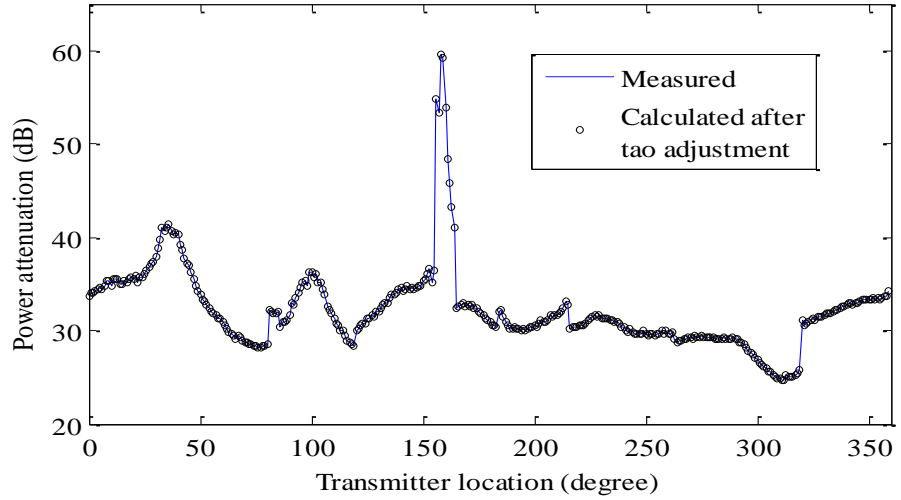
(b) with τ_i adjustment

Figure 5.3: Measured and calculated $PA_L(\theta)$

5.2.1.2 Effect of τ Inaccuracy on Calculated Power Attenuation and τ Adjustment Procedure

Based on the fact that the VNA-measured τ_i's are inaccurate due to its time resolution limit, the true τ_i's should each lie within the range of $\left[\tau_i - \dfrac{t_r}{2} \quad \tau_i + \dfrac{t_r}{2} \right]$, where $t_r = 0.3334$ ns is the VNA time resolution. The true τ_i's should then derive a corresponding power attenuation profile that closely matches the actual one. A multi-variable constrained optimization problem was defined to find such set of τ_i's that minimizes the difference between the measured and predicted power attenuation. In constrained optimization, the aim is to transform the problem into an easier subproblem that can be solved and used as the basis of an iterative process. In this dissertation, a MATLAB function, *fmincon*, was used with the active-set algorithm to solve the problem [ActiveSet]. The function uses an active set strategy to generate subproblem and uses a sequential quadratic programming method to solve the subproblem. The detailed description of the function and the algorithm is available on [ActiveSet].

The analysis shows that the power attenuation depends sensitively on τ_i's. According to Equations (3.6) and (3.7), in a multipath environment the resultant signal highly depends on the phase difference between the multiple signal components. Within a half period, the phase difference could change the resultant signal destructively or constructively.

The bounds of power attenuation prediction error for a given VNA time resolution can also be identified using the same sequential quadratic programming method with an objective that maximizes the difference. Figure 5.4 shows the upper and lower bounds of predicted power attenuation at all transmitter locations; the bounds are mostly between 60~80 dB. The range of uncertainty will improve with better VNA time resolution. The state-of-the-art VNAs can achieve a time resolution up to 0.05 ns [Anritsu], with which the range will be reduced to 5~10 dB.
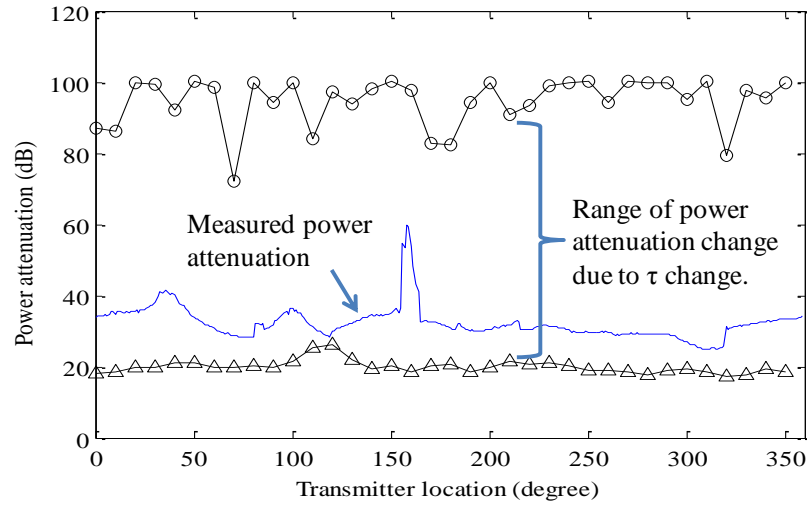
Figure 5.4: Potential ranges of $PA_L(\theta)$ change due to τ change

5.2.1.3 Effect of τ Inaccuracy on Calculated RMS Delay Spread

As RMS delay spread is also a commonly used indicator for the impact of the multipath propagation channel on transmission performance, it's also useful to understand its relationship to τ_i's. The following analysis serves two purposes: a) the τ_i inaccuracies have minor effect on the RMS delay spread, and b) RMS delay spread is not an accurate error indicator for transmission in rotating machines due to such insensitivity to τ_i differences and thereby power attenuation differences.

As defined in Equations (2.5) and (2.6), the RMS delay spread indicates the delay of the multipath components' energy center with respect to the first component's arrival time. Figure 5.5 shows the differences in RMS delay spreads before and after the τ adjustments, showing the largest difference only below 0.05 ns.
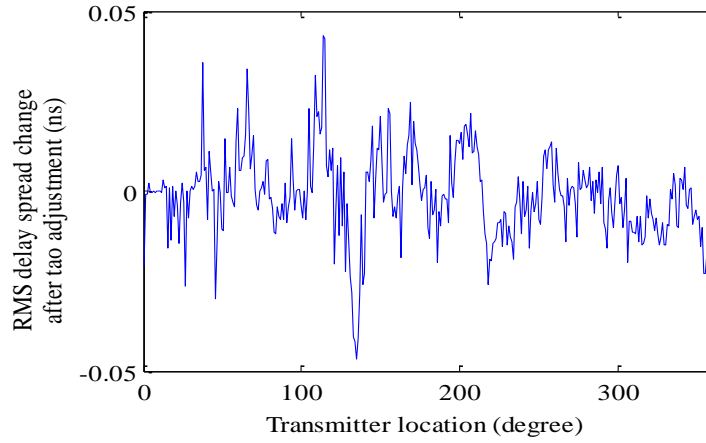
Figure 5.5: RMS delay spread change after τ adjustment

5.2.2 BER Sub-model

5.2.2.1 Validation

Given the transmit power, the power attenuation, the noise level, and the BER grey area thresholds, this sub-model predicts the BER of the data received on the other end of the channel. The sub-model is defined by Equation (3.12). In the CNC lathe as well as the chamber, sensor radio experiments were conducted to measure the received power and BER for different transmitter locations on the rotation route. With these measurements, the following validation procedure leads to three conclusions:

- The BER grey area thresholds of a same sensor radio do not change with the operation environment.

- BER predictions are accurate when the received power is outside the BER grey area.

- BER predictions are inaccurate when the received power is within the area, though such areas occur for a very small fraction of time in our settings.

78

The sub-model validation involved two phases: 1) identify the grey area thresholds to determine the BER sub-model, and then 2) validate the derived sub-model using measurement data from a different environment.

The sensor radio experiments in the chamber observed a larger range of received power and were used to identify the grey area. Totally 739 pairs of received power and PER_L were measured under stationary transmitter conditions. First, these PER_L's are transformed to BERs following Equation (4.5); then, the BERs are grouped into a series of received power bins, the width of which is 0.05 dBm. The average and the one-standard-deviation bar of BER for each bin are shown in Figure 5.6. When the received power is in the range of -94 ~ -93 dBm, the BER standard deviations are mostly as large as 0.5; out of this range, the standard deviations are consistently nearly zero. Hence, the BER grey area of this sensor radio is from -94 dBm to -93 dBm. Based on Equation (3.12), the mapping relationship between received power and BER is shown as a line in Figure 5.4.
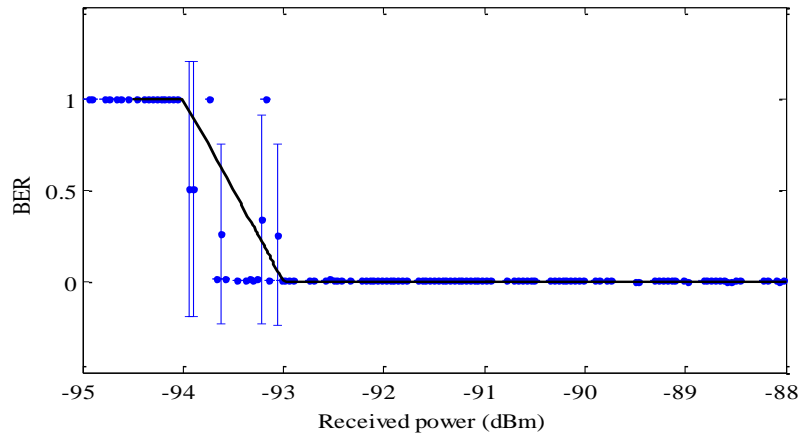
Figure 5.6: Measured received power and BER in the chamber

The second set of received power and BER was collected in an office using the same sensor radios. In the experiment, the transmitter was stationary while the receiver was randomly moved to adjust the received power. Totally 137 pairs of received power and BER were collected

and plotted in Figure 5.7. The dots radically vary when the received power is between -94 dBm and -93 dBm but concentrate at 0 or 1 out of the range, confirming the sensor radio's BER grey area was consistent despite of the environment.
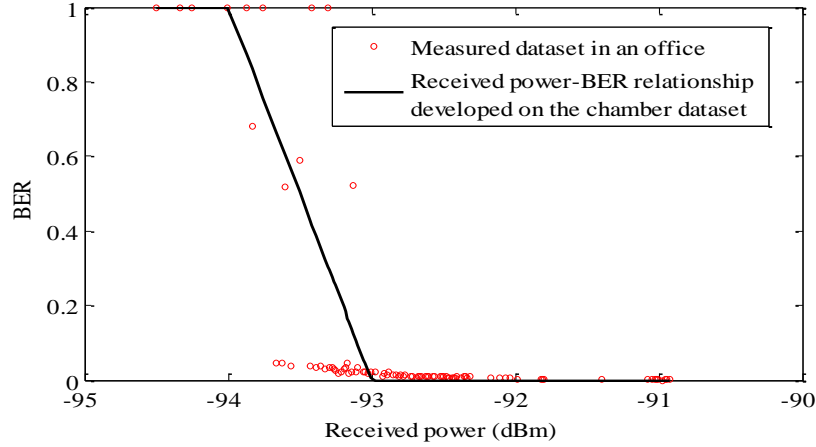
Figure 5.7: Measured received power and BER in the office

Table 5.3 gives the mean square error (MSE) between the predicted BERs and the measured BERs, showing the BER predictions are accurate outside the BER grey area and have large errors within the grey area.

Table 5.3: MSE of BER predictions

Received power	*MSE of BER predictions*
Less than -94 dBm	0
Between -94 dBm and -93 dBm	0.0933
Larger than -93 dBm	8.42×10^{-5}

Despite the prediction inaccuracy in the grey area, the BER sub-model is acceptable, since the grey area usually takes a small portion over the rotation route and the inaccuracy has no significant impact on the PER_C prediction. For example, the grey area on the CNC lathe spindle was found to be around 1 ° when the transmit power is 0 dBm or less than 1 ° when the power is

-25 dBm. With 99.7% of the predictions on the BER profile being accurate, the PER_C prediction error will be proved acceptable.

5.2.2.2 Sensitivity of Predicted BER to Received Power

The sub-model robustness is tested in terms of the sensitivity of the predicted BER to the received power. For example, the resolution of a MICAz-measured received power (P_r) is 1 dBm, so the true received power is in fact within $[P_r - 0.5 \quad P_r + 0.5]$. Consequently, the true BER is within a BER interval corresponding to the power interval. Figure 5.8 shows the BERs predicted based on the received powers from -98 dBm to -88 dBm, as well as the upper and lower boundaries of their BER prediction intervals. The figure also gives a sample of the predicted BER and its prediction interval.
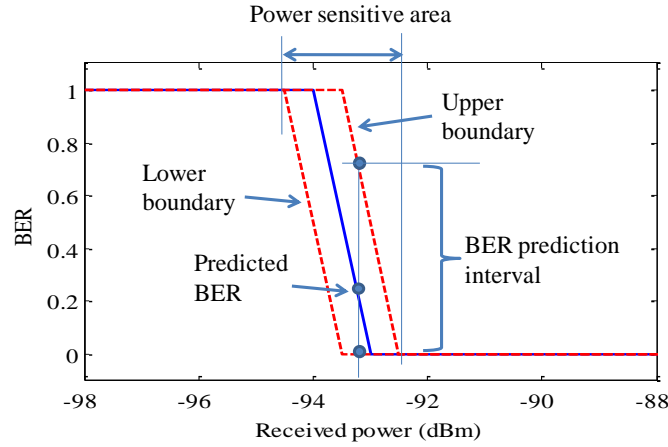
Figure 5.8: Power sensitive area and BER prediction interval due to received power errors

A large BER prediction interval is observed when the power is within the area from -94.5 dBm to -92.5 dBm. This power sensitive area is highly related to the BER grey area, because, due to the quick BER transition in the grey area, a small power variation can lead to dramatic BER change if the power is near the grey area. Given the received power uncertainty interval, ΔP_r, the

power sensitive area is $\left[P_{GL} - \dfrac{\Delta P_r}{2} \quad P_{GH} + \dfrac{\Delta P_r}{2} \right]$. If ΔP_r is small, the power sensitive area has

about the same range as the BER grey area. For example, with $\Delta P_r = 1$ dBm for the MCIAz

motes, the power sensitive area on the CNC lathe spindle was then same as the BER grey area

identified earlier. Therefore, as discussed before, the received power errors have no significant

impact on the PER_C predictions.

5.2.3 PER Sub-model

5.2.3.1 Validation

Given BER profile on the transmitter rotation circular route, packet length, radio data rate,

and rotation speed, this sub-model predicts the cycle PER. Sensor radio experiments conducted in

the CNC lathe and the chamber were measured $PER_L(\theta, 0)$ and $PER_C(\omega)$ with two transmit

powers. Based on these four sets of data, the following procedure validates the sub-model.

To implement the sub-model, the measured $PER_L(\theta, 0)$ profiles were first transformed

into BER profiles by Equation (4.5), and the results are shown as bar charts in Figure 5.9 and 5.10.

(a) 0 dBm transmit power   (b) -25 dBm transmit power
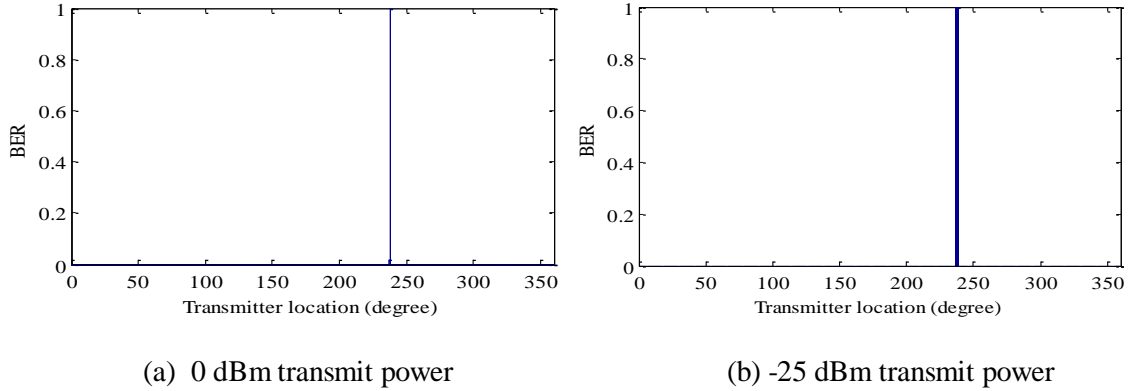
Figure 5.9: *BER* profiles in the CNC lathe
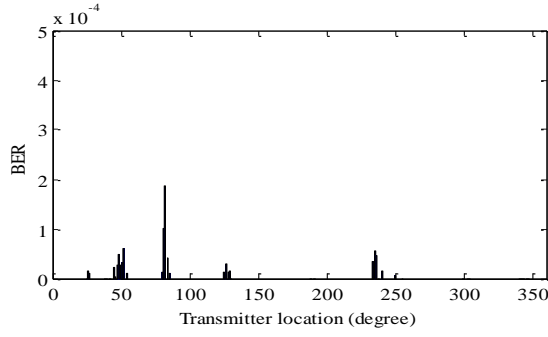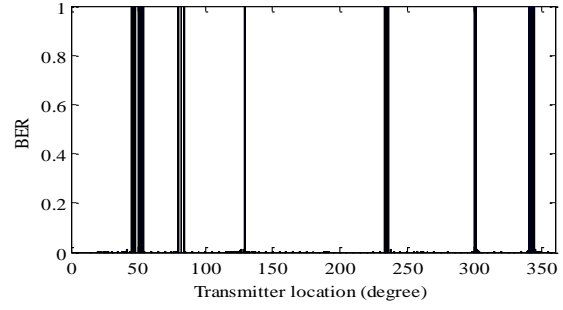
(a) 0 dBm transmit power   (b) -25 dBm transmit power

Figure 5.10: *BER* profile in the chamber

During the *PER_C* calculation, BERs at non-measured locations are required in Equation (3.13). The linear interpolation method is used to estimate these BERs using their neighboring BERs.

Figure 5.11 plots the measured and calculated *PER_C*'s for the CNC lathe measurements. In both cases, the absolute differences between the measured and the calculated are consistently less than 0.007, proving the efficiency of the sub-model. Meanwhile, the accurate predictions adequately prove the assumption of a fixed BER profile for the speed from 1061 rpm (7.2 m/s) to 1993 rpm (13.5 m/s).
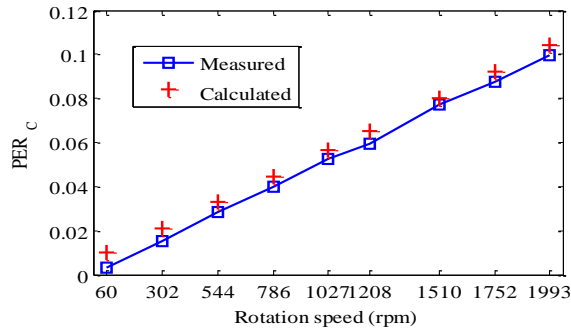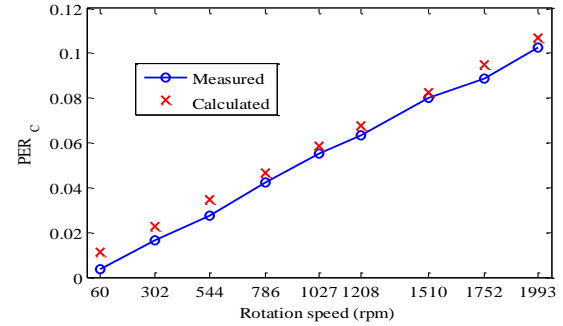
(a) 0 dBm transmit power   (b) -25 dBm transmit power

Figure 5.11: Measured and calculated *PER_C* in the CNC lathe

Figure 5.12 plots the results for the chamber measurements. For the 0 dBm transmit power, the absolute differences are less than 0.007, while, for the -25 dBm, the maximum absolute difference is 0.018, which occurs at 252 rpm. Nevertheless, compared to the measured PER_C of 0.19 at that speed, the relative difference is 9%, which is on an acceptable prediction error level.

(a) 0 dBm transmit power   (b)   -25 dBm transmit power
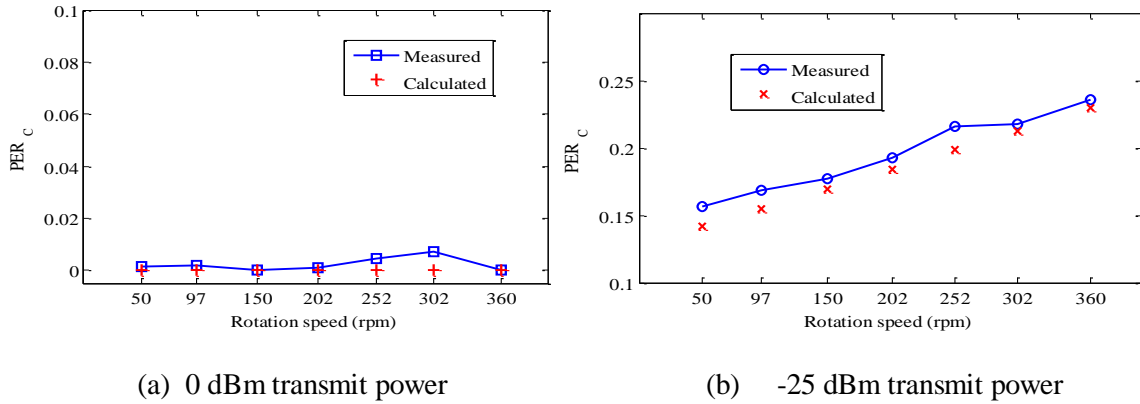
Figure 5.12: Measured and calculated PER_C in the chamber

5.2.3.2 Sensitivity of Predicted PER_C to BER Profile

The analysis on the predicted PER_C sensitivity to BER profile will prove that, BER errors in a small fraction of the BER profile have little impact on predicted PER_C. This will validate the BER sub-model's applicability even with prediction errors in the grey area.

For example, with the 0 dBm transmit power, around $1°$ of transmitter locations on the lathe spindle were within the BER grey area. A PER_C prediction interval is determined by considering two special cases: a) these BERs are all 0, or b) these BERs are all 1. In each case, a new BER profile is generated, and a PER_C corresponding to the new profile is calculated. The true PER_C must lie within the interval bounded by the two predicted PER_C's.

Figure 5.13 gives the PER_C prediction interval over the speed range measured in the experiment as well as the predicted PER_C's based on the measured BER profile. The width of the

PER$_C$ prediction interval is consistently as low as around 0.003, suggesting the predicted *PER$_C$* is not sensitive to the BER errors in the grey area.
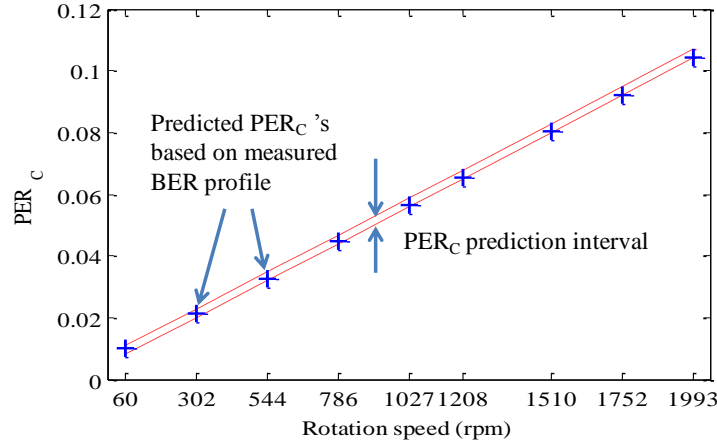
Figure 5.13: *PER$_C$* prediction interval corresponding to BER errors in the grey area

5.2.3.3 *PER$_C$* Prediction Uncertainty

Defined as the width of the *PER$_C$* prediction interval, the prediction uncertainty is provided as supplementary information for the outcome of the PER predictive model. The smaller the uncertainty is, the more possible that the prediction is accurate. Model users choose to accept or reject the prediction result based on their requirement for the uncertainty.

Figure 5.14 illustrates the steps of the uncertainty calculation. As an intermediate parameter of the BER sub-model, the received power profile has been derived, so that the grey-area transmitter locations are able to be found. Then, the *PER$_C$* prediction interval's upper boundary *PER$_{CU}$* and lower boundary *PER$_{CL}$* are calculated by the PER sub-model respectively by the special case method described in Section 5.2.3.2. The difference between the boundaries is the prediction uncertainty.
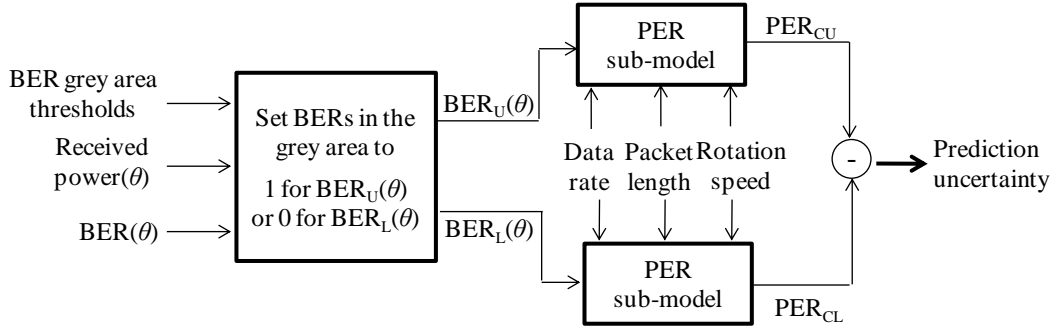
Figure 5.14: Calculation of PER_C prediction uncertainty

The PER_C prediction uncertainty is highly related to the range of the grey-area transmitter locations. A large range means a large portion of the BER profile may contain prediction errors and further results in a large PER_C prediction uncertainty.

5.3 Summary

In this chapter, the three sub-models of the proposed PER predictive model were individually assessed with the experiments. The conclusions are summarized as follows.

- Due to the VNA limitation, the time resolution of channel multipath profiles is too coarse for accurate power attenuation prediction. However, the difference between the predicted and measured power attenuation lies within a range dictated by the VNA time resolution. The observations suggest that predicting power attenuation from multipath profile is possible and its accuracy potentially improves with VNA's time resolution.

- The BER sub-model provides accurate BER predictions when the received power is outside the BER grey area, but the predictions are inaccurate when the power is within the area. However, it's been proved that, in the practical lathe environment, the grey-area BER prediction errors have little impacts on PER_C prediction.

- The PER sub-model successfully predicts PER_C's with small uncertainties. The PER_C prediction uncertainty can be estimated in the model implementation and serves as prediction accuracy metric.

The experiments have observed a location-dependent error distribution on the transmitter rotation route. The following chapter introduces two data transmission protocols to enhance communication performance of radio channels with such a feature.

Chapter 6

Implementation and Analysis of Reliable Protocol Transmission Performance

Analysis of rotating sensor radios' bit error pattern reveals that the errors are concentrated in bursts which correspond to certain fixed locations. In this chapter, two radio transmission protocols are presented to achieve reliable communication for such radio channels: ARQ-based transmission method and online error avoidance algorithm. As a channel capacity metric, throughput is defined as the rate of successfully transmitted bits over a communication channel. To start with, Section 6.1 presents the analysis of bit error burst pattern. Section 6.2 introduces the ARQ-based transmission method and provides experimental evaluation results. Section 6.3 presents the error avoidance algorithm and discusses its simulated performance. The protocols are summarized in Section 6.4. Figure 6.1 gives the chapter structure.
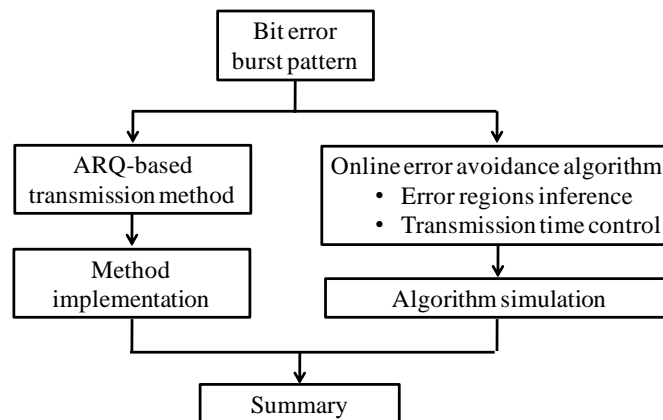
Figure 6.1: Structure of Chapter 6

6.1   Bit Error Burst Pattern

To understand the pattern of transmission errors occurred in the rotating sensor transmitter on the CNC lathe spindle, the bit errors of all packets received with errors were analyzed. The analysis revealed that the bit errors occurred in bursts. An error burst is defined, for each error packet, as the minimum interval that contains a specified fraction H of all error bits. $H = 1$ was considered in this study. An analysis of the inter-arrival times T_i between the $(i)^{th}$ and $(i+1)^{th}$ error bursts suggested that the error occurrences closely coincided with certain location(s) around the rotation circular route. This conclusion was a result from mapping the inter-arrival times to the corresponding angular distances traveled by the rotating transmitter, defined as the normalized error burst distance, D_i, as $D_i = \dfrac{T_i \text{ modulo } T_R}{T_R}$, where T_R is the spindle rotation period.

Figure 6.2 shows the normalized error burst distances observed from packets transmitted during 2054 rpm rotations. As seen, the error burst distances concentrated near 0 and 1 cycle, suggesting the majority of error bursts occurring near the same location around the circular route. In the experiment, 13473 packets were transmitted at constant 15 m intervals; out of them 1457 packets were received with bit errors, and the PER was 0.118 (including lost packets and packets with errors). Similar patterns were observed for other rotation speeds as well.
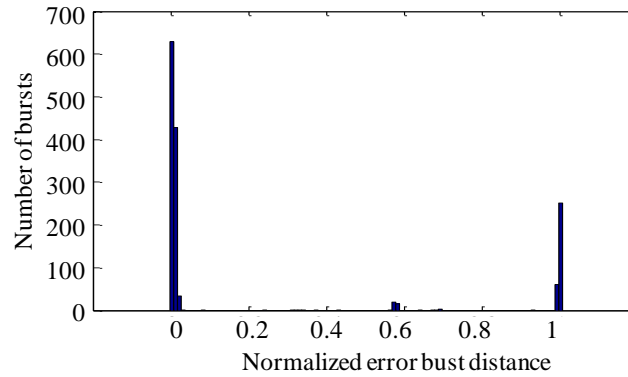
Figure 6.2: Error burst distance distribution at 2054 rpm

The finding suggested that at a certain rotation speed, one or a few "error-prone regions" could be identified, and among them would be interleaving "low-error" regions. If these regions can be identified, a reliable transmission scheme can most effectively maximize its reliable throughput.

6.2   ARQ-based Reliable Transmission Method

The ARQ-based reliable transmission method is built on the IEEE 802.15.4 acknowledgement option. With the option enabled, the transmitting radio is notified of a failed transmission when an acknowledgement packet is not received after a data packet transmission. Upon each failed transmission, the ARQ function schedules an immediate retransmission, i.e., to retransmit the packet after the IEEE 802.15.4 random back-off interval. A failed transmission could have begun and ended at anywhere within an error-prone region, and its retransmission may not necessarily take place within a low-error region. The probability of a successful retransmission depends on the width of the error-prone and low-error regions with respect to the chosen packet length.

The ARQ experiments were conducted in the CNC lathe at 2054 rpm with the setup as shown in Figure 4.12(b). In each experiment, packets of a chosen packet length (30, 60, 92 bytes, 10 byte header size included) were generated at a chosen constant interval (0, 100, 150, and 250 ms). The 0 ms interval experiment refers to a link saturating operation where the transmitter has an infinite backlog and sends a new packet for transmission whenever the previous packet has been transmitted/retransmitted successfully or the maximum limit of 9 retries is reached. The throughput thus achieved is referred to as the saturated reliable throughput.

Table 6.1 summarizes the key experiment results, including the first transmission error rate and the average retransmissions per error packet with respect to different packet lengths and

packet generation intervals. With the 0 ms interval experiment, the saturated reliable throughput was found to be 25.8, 50, and 70.6 kbps with 30, 60, and 92 byte packet lengths.

Table 6.1: Experimental results with the ARQ transmission method

Packet generation interval	Packet length	1st transmission error rate	Retransmission count mean /standard deviation
0 ms	30 bytes	0.098	1.026/0.159
	60 bytes	0.137	1.253/0.435
	92 bytes	0.151	1.191/0.424
100 ms	30 bytes	0.067	1.000/0.000
	60 bytes	0.136	1.000/0.000
	92 bytes	0.171	1.140/0.365
150 ms	30 bytes	0.059	1.000/0.000
	60 bytes	0.143	1.000/0.000
	92 bytes	0.181	1.042/0.202
200 ms	30 bytes	0.067	1.000/0.000
	60 bytes	0.087	1.046/0.209
	92 bytes	0.220	1.112/0.316

The observed high error rate of the first transmissions and high success rate of the following retransmissions suggest that the retransmissions have most probably taken place in the low-error regions due to the rotation. The transmission and retransmission success rates both increased as the packet length decreased. The saturated reliable throughput is an upper bound for packet generation rate at which all packets can be expected to be delivered successfully. The 100, 150, and 200 ms packet generation intervals were far below the limit and all had reliably delivered all generated packets. Additional experiments were conducted with higher transmit powers and higher rotation speeds and showed no clear correlation with the radio performance.

The maximum reliable throughput achieved by the ARQ approach was 70.6 kbps (92 byte packet length), which is only about 28% of the nominal IEEE 802.15.4 data rate of 250 kbps. Whether further enhancement is possible depends on the actual error-prone region pattern and the ability of a transmitter to identify such regions for determining error-free transmission timings. Further experiments with more precise transmitter location tracking and transmission time control will be necessary to explore such capacity.

6.3 Online Error Avoidance Algorithm

In order to reduce PER and increase data transmission throughput, the online error avoidance algorithm is proposed for sensor radios to infer the error region distribution based on observed transmissions and control the packet transmission times.

6.3.1 Online Error Region Distribution Inference

To enable error avoidance, the error region distribution must be identified. Without positioning support, the absolute locations of the error regions cannot be determined; instead, sensor radios can utilize time stamps to calculate the relative location with respect to a reference location (i.e., starting location in this case) to infer whether it is inside or outside an error region each time it transmits. For error region localization, the error burst location distribution is proposed as follows:

Given the beginning timestamps of a set of consecutive error bursts, let the normalized distance between the ith and $i+1^{th}$ error bursts be D_i, the first error burst's beginning location as the reference origin, the normalized error burst location, L_i, for the ith error burst is defined as

$$L_i = \left(\sum_{j=1}^{i} D_{j-1} \right) \bmod T_R \tag{6.1}$$

where T_R is the spindle rotation period.

Clock drift of sensor radios is the main challenge when obtaining the location distribution. As the machine does not provide digital clock output, a visual assessment found the sensor clock to lead approximately 15 seconds ahead the machine clock every 12 minutes. Clock drift renders the recorded timestamps and calculated error burst locations to drift from their actual location. In fact, this was the main reason that in [Tang2009] discernible error regions can only be found using the error burst distance distribution instead of location distribution.

To compensate for the drift impact, accumulated error in the estimated error burst locations must be calibrated periodically. Without external synchronization, the calibration is done by analyzing the location distribution in small time windows and aligning the resulting distributions. The clock drift problem and potential rotation speed inaccuracies also make it difficult for the rotating sensor to track its location with respect to the error burst location distribution's origin.

To address this limitation, the proposed transmission error avoidance method operates in two phases: the training phase and the operational phase.

- In the training phase, the sensor transmits probe packets to collect sufficient transmission history to establish the error burst location distribution. Given the distribution, the centre and width of each error region with PER above a chosen threshold is identified.

- In the operational phase, the sensor begins with data transmission. Initially, transmissions can occur at any time when data are present until a number of transmissions are received with errors in a predefined time window. The sensor analyses the error packets' timestamps to logically deduce its present location with respect to (i.e. synchronies with) its error burst location distribution. Once it successfully synchronizes, it starts to control the times of its data transmissions. Prior

to each transmission, the expected transmission interval is estimated based on the IEEE 802.15.4 medium access control procedure and parameters; a data transmission is permissible when its expected duration does not overlap with any error region; otherwise, the transmission will be delayed until the end of an earliest error region with a following low-error duration that is sufficient for the transmission to complete.

To determine the exact time an error burst has occurred within a received data packet during the operational phase is more difficult than that in probe transmissions during the training phase. Since the data contents are not known previously, the location where bit errors have occurred cannot be directly determined. There are methods to explore this information without substantial overheads. For example, since ARQ is adopted, packets are retransmitted until they complete successfully. By caching and comparing packets in error with their successful retransmissions, the error burst occurrence times can be found. For another example, transmitted data can be encoded with known bit patterns at predetermined intervals in each packet, such that error burst occurrence times can be identified in each packet at a granularity equal to the encoding interval.

Since the purpose for an error avoidance approach is to improve energy efficiency and data throughput, it is beneficial only when the following conditions are true:

- The PER for uncontrolled transmissions is found to be unacceptably high.

- The training phase identifies distinguishable error regions.

- Intervals between error regions have very low PER and are longer than one data transmission time.

The last condition suggests the importance of specifying an appropriate packet length. When none of the above conditions are met, error avoidance should not be applied.

6.3.2 Transmission Time Control for Error Avoidance

In the operational phase, the receiver first synchronizes with a given error burst location distribution by observing the timing of multiple error bursts, it then proceeds with transmission time control. To achieve synchronization, the receiver calculates the error burst distances $\{D_i\}$ for the observed error burst sequence and performs the error location synchronization as follows:

Given $\{D_i\}$ of N consecutive error bursts, an error burst location distribution $\{L_j\}$ of M identified error regions of width δ, miss rate threshold E, the receiver performs error location synchronization as follows. For $j = 1$ to M,

1. Let the current location $C = L_j$, miss count $s = 0$, error burst distance index $i = 1$ and $k = j$.
2. If $(C + D_i) \in L_k+1 \pm \delta$, $C = L_k + 1$, $k = k + 1$; otherwise, $C = C + D_i$, $s = s + 1$. Increment i and repeat step 2 until $i > N$.
3. If $s/N \leqslant E$, synchronization completes successfully; otherwise, algorithm continues.

Once the synchronization completes successfully, the receiver informs the transmitting sensor of the last error burst timestamp and its corresponding synchronized location C. If the algorithm ends unsuccessfully, the algorithm must be repeated at a later time.

Assuming the transmitting sensor and the receiver have synchronized local clocks, the transmitting sensor can determine at any time: its location, the duration until beginning of the next error region and the beginning of the next low-error region that is no shorter than the estimated transmission time of the next packet.

6.3.3 Simulation Studies

A rotating sensor radio simulator models the transmitting radio's instantaneous position given the rotation speed, error burst location distribution and BER in each error region and low-error region, based on which bit errors are randomly generated for each bit of a transmission.

Radios are assumed to have synchronized with the error distribution. Results for a number of representative scenarios are presented in the following sub-sections.

100% BER in error regions, 0% BER outside error regions

This is an idealized setting that illustrates the typical benefit of the scheme. Figure 6.3 shows the PER and data throughput achieved when there was one error region (4-degree wide and BER is 1) with and without error avoidance, with different packet lengths and packet generation intervals. In Figure 6.3(a), it is seen that larger packets had higher PERs on average; PERs remained consistent with different packet generation intervals, reaching about 10% with 92 byte packets. With error avoidance, errors were completely avoided, while a slight decrease in throughput was seen.
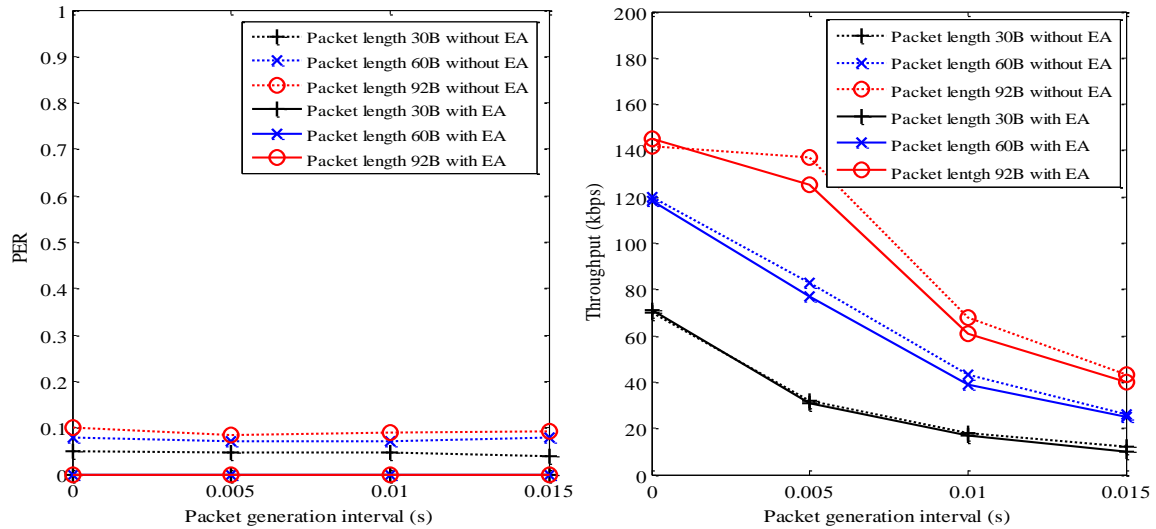
(a) PER vs. packet interval and length   (b) Throughput vs. packet interval and length

Figure 6.3: PER and data throughput achieved for one error region (EA: error avoidance)

A more challenging scenario was studied with four error regions each 4-degree wide and centered at 0, 90, 180 and 270 degree. Figure 6.4 shows the PER and throughput. Interestingly, with scattered error regions, PERs increased as packets are generated faster, reaching 50% with

92 byte packets. With error avoidance, throughputs were substantially increased (50~75% for continuous transmissions). Also interesting was that with- and without-error-avoidance throughput curves came close as the packet interval increased; they merged eventually, and the merging point depended on the packet lengths – the larger the size, the later the merge, the more throughput gain achievable with error avoidance.

(a) PER vs. packet interval and length   (b) Throughput vs. packet interval and length
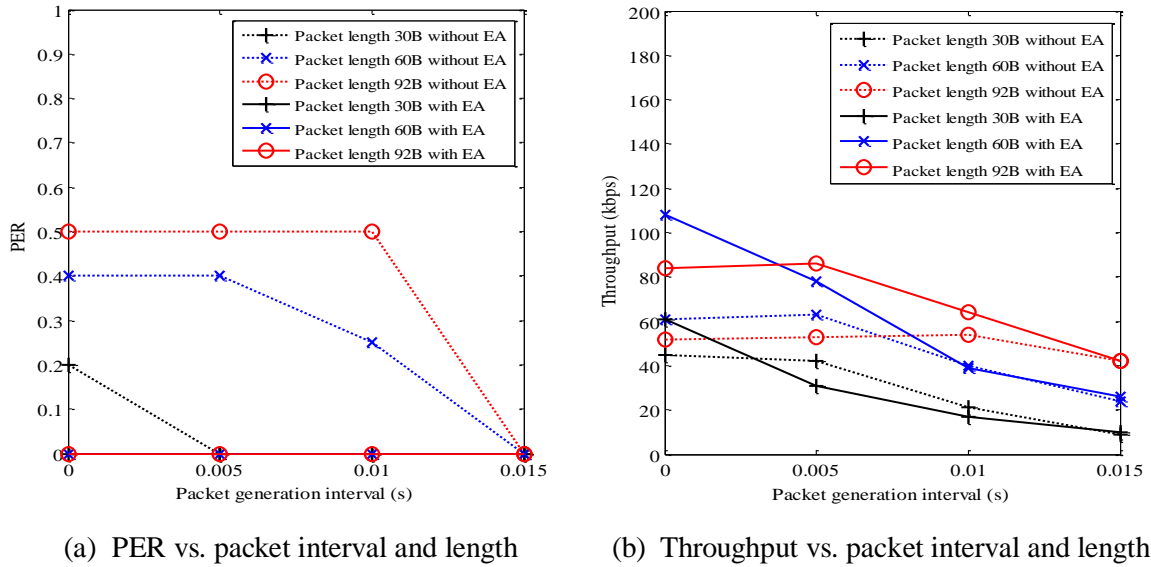
Figure 6.4: PER and data throughput achieved for four error regions (EA: error avoidance)

Less than 100% BER in error regions, nonzero BER outside error regions

In practice, BERs inside and outside error regions may not be 1 and 0, respectively. Figure 6.4 shows the achieved throughput with different BERs outside the error region. When BERs were 0.01 or less, error avoidance increased achievable throughput by nearly 40% when data rate was very high. Once the BER approached 0.1, substantial errors occurred even outside the error region, therefore, error avoidance was no longer beneficial. The Figure presents throughput results for BER up to only 0.1, as the significance of throughput degradation has been evidently demonstrated.
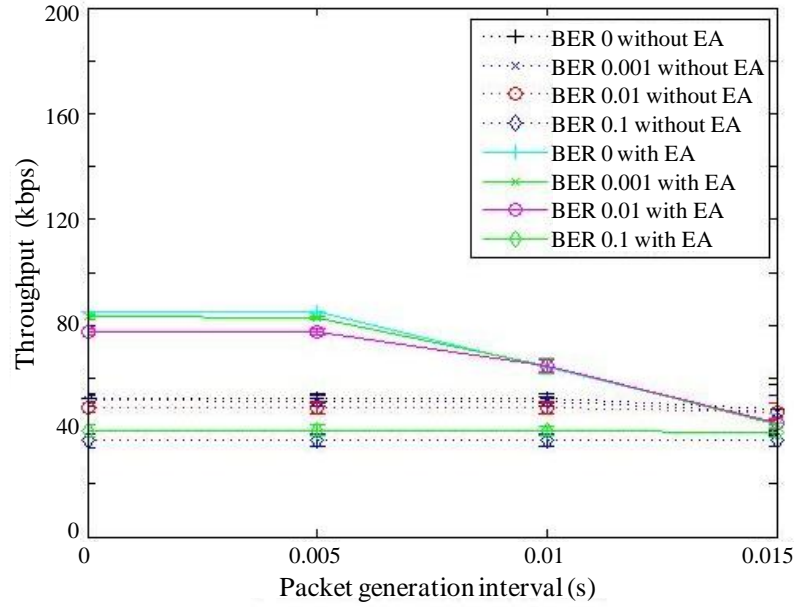
Figure 6.5: Throughput vs. BER outside error regions (four 4-degree error regions, 92 byte packets, BER in error region is irrelevant since transmissions are entirely avoided)

6.4 Summary

The bit error pattern analysis revealed that the errors were concentrated in bursts that correspond to certain fixed positions during the rotation, revealing an opportunity to transmit data reliably by avoiding the error regions. The ARQ-based reliable transmission scheme was then implemented to evaluate the potential of performance enhancement with more intelligent data transmission methods. The ARQ approach effectively assured a reliable data transmission during rotation with little retransmission overheads, and the reliable transmission throughput varied with different packet lengths and packet generation intervals.

The chapter presented an online error inference and error-avoidant transmission method for sensors with low accuracy clocks. With simulation, the method was shown particularly effective when required data transmission rates are high and error regions are scattered around the rotation circular route. The simulation studies showed a 50% error reduction and up to 75%

throughput increase; higher throughput gains are expected for applications with more frequent and larger size data transmissions.

Chapter 7

Contributions and Future Work

7.1 Contributions

As the first attempt to systematically understand data transmission performance of sensor radio on a rotating mechanical structure (spindle), this study aims to ignite more researches in the area of wireless data transmission evaluation for reliable and effective structural health or machine condition monitoring applications. It is especially of great importance for rotating structural monitoring such as monitoring of roll contact, grinding wheel, engine blade, and motor shaft using wireless sensors. The main contributions of the dissertation are summarized as follows.

7.1.1 Multipath Propagation Assessment in Machine Tools

Systematic experiments were performed to assess the multipath propagation in a modern CNC lathe as the first research effort in machine tools. The experiments show the lathe's inner space has different properties than other industrial sites. Two important phenomena are summarized.

- The number of multipath signal components in the lathe is more remarkable, indicating the existence of severe multipath propagation. In the small and closed space, radio signals are subject to multiple reflections by the lathe's metal enclosure, creating more signal paths between the transmitter and the receiver.

- The RMS delay spread in the lathe is small, which means the signal components' arrivals concentrate in a short time duration. The energy of the components arriving after this duration significantly attenuates.

7.1.2 Transmission Error Cause Analysis for Rotating Sensor Radios

Signal power attenuation, ISI and Doppler shift had been considered as three possible causes of data transmission errors of rotating sensor radios. The research work in this dissertation provides experimental and theoretical investigation on each cause, and the conclusions are summarized as follows.

- Multipath-induced power attenuation is the prominent cause for data transmission errors. The severe multipath propagation raises the possibility of small-scale fading of radio signals in the lathe. Signal power attenuation could substantially vary with a small transmitter movement on its rotation route, which has been proved in both the sensor radio measurements and the VNA measurements.

- ISI is not a significant transmission error cause for the sensor radio platform we used and the CNC lathe environment we studied. The conclusion should be true for other similar sensor radio platforms and environments.

- Doppler shift is not a significant transmission error cause in our case either. Based on the estimation of the highest possible Doppler spread, the Doppler spread in the multipath-rich lathe environment is far below the symbol rate of the sensor radios for the transmitter speed as high as 13.6 m/s (equivalent to 2000 rpm in our sensor radio setup).

7.1.3 PER Predictive Model for Rotating Sensor Radios

The key contribution of this dissertation is the PER predictive model for such radio channels with fast rotating sensor radios. The model provides a method to predict the overall data

transmission performance in terms of the cycle PER. The model consists of three sub-models, each of which functions independently for a specific purpose. By the systematic experiments in the CNC lathe and the anechoic chamber using the sensor radio-based setup and the VNA-based setup, these sub-models were evaluated and their robustness and prediction errors were discussed too.

- The signal power attenuation sub-model provides an analytical estimation of power attenuation from given channel multipath profile and signal frequency. The power attenuation is highly sensitive to the time delays of the signal components. Due to the frequency band limitation of the VNA, the time resolution of CIR is not sufficient for the accurate estimations of power attenuation. However, it is shown that the difference between the predicted and measured power attenuation lies within a range dictated by the VNA time resolution, and predicting power attenuation from multipath profile is possible and its accuracy potentially improves with VNA's time resolution.

- The core of the BER sub-model is the relationship between received power and BER. A simple mathematical model is proposed for environments with low background noise. If the received power is out of sensor radios' BER grey area, the prediction is accurate and the sub-model is robust. If the received power is within the grey area, the sub-model inherently introduces prediction error, which is, however, insignificant for entire BER profile, since in many situations, the majority portion of the received power profile on the rotation route is out of the area. This has been proved by the measurements in the CNC lathe and in the chamber.

- As a last part of the model, the PER sub-model derives cycle PER, defined as the average of PERs at all transmitter locations during rotation. The sub-model's key is assigning an individual BER to each bit of a transmitted packet according to the bit's transmission

102

location. Based on the experiments in the CNC lathe and in the chamber, the sub-model demonstrated a satisfactory prediction performance. With worst case analysis, BER errors on a small portion of the BER profile was proved to have insignificant effects on predicted cycle PER.

7.1.4 Reliable Transmission Protocols

The analysis of bit error pattern of rotating sensor radio in the CNC lathe revealed a busrty bit error patter. For radio channels with such error patterns, the dissertation presented two data transmission methods for reliable communication performance. With experiments, the ARQ-based transmission scheme was proved to effectively assure a reliable data transmission during rotation with little retransmission overheads. With simulation, the online error inference and error-avoidant transmission method was shown particularly effective when required data transmission rates are high and error regions are scattered around the rotation circular route. The simulation studies showed a 50% error reduction and up to 75% throughput increase.

7.2   Future Work

7.2.1   PER Threshold for Error Region Distribution Inference

When identifying error region distribution in the training phase of the error avoidance method as described in Section 6.3.1, the assumed PER threshold can determine the centers and widths of error regions. An optimal PER threshold is critical for a tradeoff between energy efficiency and data throughput. The higher the assumed PER, the narrower the error regions' widths, and the more chances an error could occur outside the identified error regions, which

limits data transmission enhancement by the error avoidance method. The lower the assumed PER, the wider the widths, and the more computation cost spent on data transmission time control.

A self-adaptive search algorithm can be designed for determining the optimal PER threshold based on the user-defined priorities for data throughput and energy saving. An advanced algorithm may be able to intelligently adjust the priorities to meet short-time requirements, such a higher throughput for the quick transmission of a vibration shock signal.

7.2.2 Adjustable Transmit Power Mechanism for Reliable Transmission

An adaptive power control and management mechanism can significantly save the power consumption of transmitters and extend their life time. In many sensor radio applications on manufacturing machines, the physical distance between the transmitter and the receiver is not necessarily large. This type of radio placement ensures, at the majority of the transmitter locations on the rotation circular route, the radio channel enjoys low power attenuation with occasional high power attenuation occurrences. Given the precise information of the time-varying power attenuation, the transmitter is able to intelligently adjust the transmit power to achieve an optimum tradeoff between power saving and transmission success.

7.2.3 Online Channel Assessment

Adaptive strategies are based on a precondition that the local properties of power attenuation or PER are known. In the implementation, this information could be stored in memories of the transmitter. However, environments in manufacturing machines frequently change. The transmitter needs to update the information periodically. An online channel assessment algorithm is required for this purpose.

The algorithm could be implemented on the transmitter or the receiver, while the results must be reported to the transmitter. The basic idea is to find the periodic temporal features of

packet errors and losses so that the transmitter can determine next transmission time to avoid the high error rate durations. The finding procedure could be performed in an exclusive period of trial transmissions or a period of real sensor data transmissions. With the online channel assessment algorithm, the intelligent transmission protocols become flexible and powerful and highly expand wireless sensor systems' applicable applications.

7.2.4　High Bandwidth VNA Measurements

The limitation of the VNA bandwidth restricted the power attenuation sub-model validation. A higher bandwidth VNA provides a finer time resolution for CIR measurements and decreases power attenuation uncertainty range due to the inaccuracy of τ's. In the future, the sub-model validation result can be refined by using a higher frequency bandwidth VNA.

Appendices

Appendix A

Channel Characterization of Sensor Radios in Machine Shop

A.1   Machine Shop Environment

Channel characterization measurements were conducted in the machine shop at the Engineering Innovation Building of Clemson University, South Carolina. The shop was 16 m in length, 10.5 m in width, and 5 m in height. Its ceiling was covered by heating, ventilating and air-conditioning (HVAC) pipes. The walls were made of concrete, and there were two 0.6 m-by-0.6 m concrete pillars supporting the roof. As shown in Figure A.1, the machine shop housed typical machine tools and miscellaneous inventories whose detailed information is listed in Table A.1.
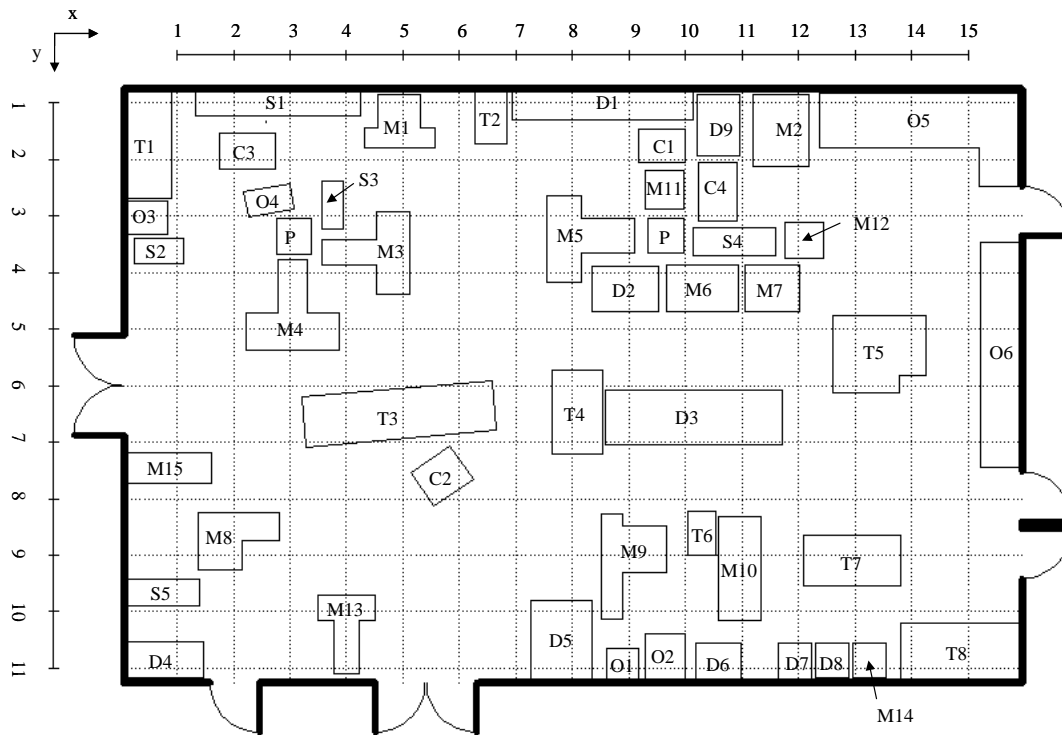
Figure A.1: Layout of machine shop and grid division (T: Table, C: Cart, M: Machine, D: Drawer, cabinet, chest, or roll-away, S: Shelf, P: Pillar, and O: Others)

Table A.1: Machine shop inventory for Figure A.1

Index	Height (cm)	Material	Note
T1	91	Steel	Steel table with a steel vice
T2	79	Wood	
T3	97	Wood	Steel vices, drills, hammers, etc
T4	94	Wood	
T5	89	Steel, wood	*Delta* tilting arbor saw table
T6	102	Wood	Table with different cutting tool sets on the top
T7	94	Wood	
T8	91	Stone, wood	Sink
C1	81	Steel	
C2	114	Plastic, steel	
C3	122	Plastic	
C4	107	Steel	
M1	163	Steel	*Harig* super 612 grinder
M2	157	Steel	*Sears Craftsman* radial saw
M3	201	Steel	*Gorton Mastermil* mill
M4	241	Steel	*Acer/Springwood Industrial* E-Mill mill (Model EVS-3VKH-54)
M5	208	Steel	*Wells-Index* mill (Model 747)
M6	191	Steel	*DoALL* vertical saw
M7	198	Steel	*Wilton Strands* drill
M8	102	Steel	*Ellis* band Saw (Model 1600)
M9	213	Steel	*Mighty Machinery Comet* mill (Model 3VHC)
M10	122	Steel	*Sharp* lathe (Model 1440)
M11	221	Steel	*Buffalo Forge* forge
M12	175	Steel	*Sears Craftsman* drill (Model 113.21371)
M13	203	Steel	*Bridgeport* mill (Model 6340)
M14	163	Steel	*Franklin* heavy duty shop press (Model F-03)
M15	112	Steel	*Sears* and *Black & Decker* bench grinder, *Delta* sander

Table A.1 (Continued)

D1	152	Steel	
D2	135	Steel	
D3	122	Steel	
D4	221	Steel	
D5	130	Steel	
D6	127	Steel	
D7	109	Steel	
D8	155	Steel	
D9	110	Wood	
S1	130	Steel	
S2	163	Steel	
S3	185	Steel	
S4	180	Steel	
S5	183	Steel, wood	
O1	94	Steel	Sink
O2	97	Steel	*Selig* filtration system
O3	142	Steel	Gas cylinder
O4	81	Steel	Miller welding power source/wire feeder
O5	N/A	Wood	Wood stack
O6	N/A	Wood, plastic, steel	Chairs, hanger, refrigerator, etc

A.2   Experiment Design

The experimental system utilized MICAz motes and a MIB510 of *Crossbow*. Mote A was fixed at the center of the machine shop (point (8, 6) in Figure A.1), 3m above the ground while below the HVAC pipes. Mote B was to be placed sequentially at different locations in the site. The machine shop was divided into 15×11 1m-by-1m grids, and Mote B was sequentially placed at each grid point, (x, y), for one measurement. At all grid points with an open ground, Mote B

was placed on top of a vertical 90 cm high wooden stick. At any grid point blocked by machines, tables, cabinets, or drawers, Mote B was to be placed on top of these objects at slightly adjusted heights. To ensure that the experiment results are comparable, the mote placement heights were controlled within the range of 80 cm to 160 cm above the shop floor level. Every link between Mote A and Mote B was bi-directional, denoted as link (x, y). In the following, uplink (x, y) denotes a transmission from Mote B, which is located at (x, y), to Mote A; downlink (x, y) denotes a transmission from Mote A to Mote B.

The first experiment was to capture the spatial radio channel properties due to stationary structures and obstacles. The second experiment was to study the temporal variations in link quality. Link (2, 2) was monitored continuously for 24 hours. The sequence of measurements over 24 hours was examined in 5-minute averages to study the link's temporal variations.

In both experiments, RSSI, link quality indicator (LQI), and CRC status of each received packet were saved. Average RSSI, average LQI, and packet error rate (PER) metrics presented for each link measurement were calculated over 2000 transmitted packets (100-second data with a 50-milliseconds interval) in the spatial experiment, and over 150 transmitted packets (5-minute data with 2 seconds of packet interval) in the temporal experiment.

A.3   Channel Spatial Properties

For the spatial experiment, Figure A.2 show the average RSSI, average LQI, and PER for both uplink and downlink transmissions at each grid. In the upper-left and upper-right areas, the received signal energy exhibited very different decay profile vs. distance, as compared with that observed in other areas. Interestingly, links in these areas also had lesser average LQI (for example, less than 100), e.g., links (12, 1), (14, 1), (11, 4), (3, 5), and (13, 5). Average LQI in other areas were almost identical and were close to 110; 86.7% of uplinks and 92.7% of downlinks had average LQI greater than 105 in these areas.
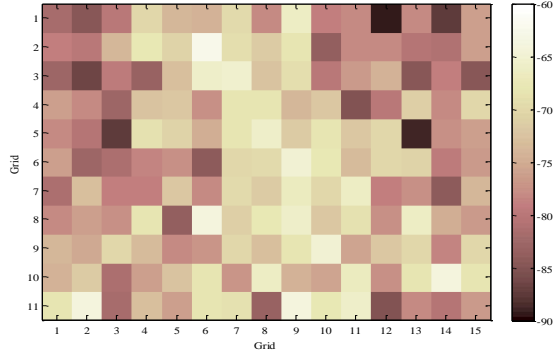
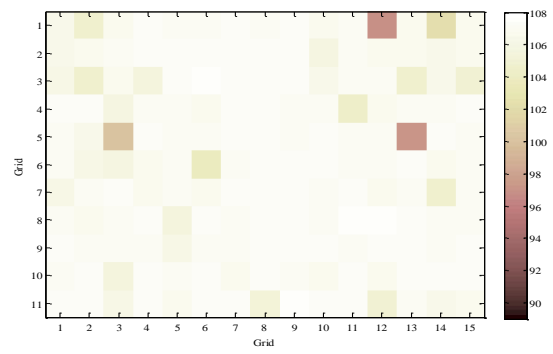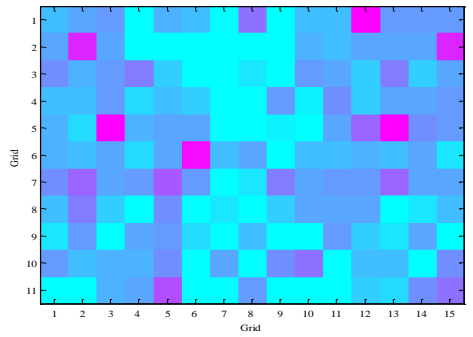(a) Average uplink RSSI (dBm)
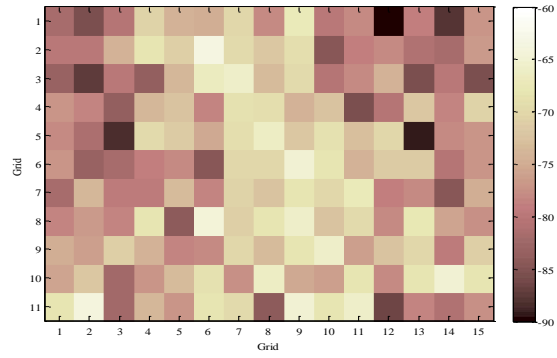
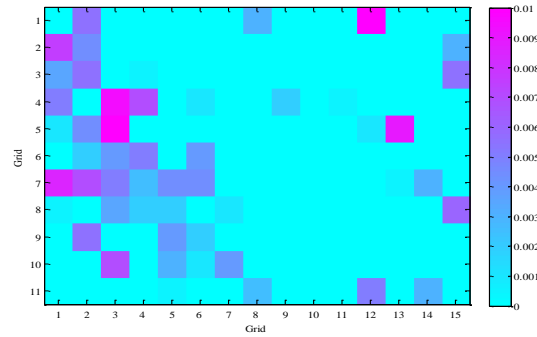(b) Average downlink RSSI (dBm)
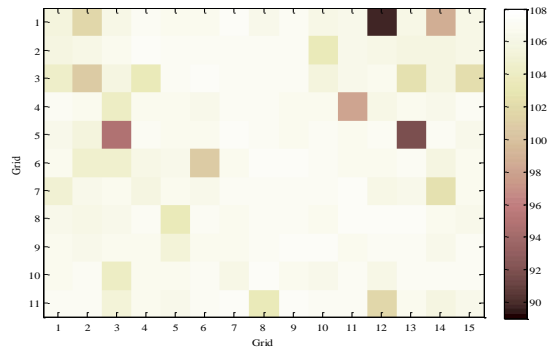
(a) Average uplink LQI

(d) Average downlink LQI

(e) Uplink PER

(f) Downlink PER

Figure A.2: Topographical measurements of average RSSI, average LQI and PER (grid points are not to scale)

Figure A.2 clearly shows the anisotropic nature of all metrics. Specifically, radio links with the same LOS distance did not necessarily have similar average RSSI, average LQI, or PER. For example, downlink (13, 5) had an average RSSI of -89.4 dBm and PER of 0.009, but nearby downlink (13, 7) had an average RSSI of -78.2 dBm and only one packet was not correctly received among the 2000 samples. Grids of steeper average RSSI drops are not necessarily blocked along their line-of-sight paths, e.g. link (7, 10) and (12, 7), suggesting the dominant multipath effects in the cluttered areas. A visual comparison of the three figures does show similarity among all three metrics' profiles. This is intuitively reasonable, as the superposition of multipath components arriving from different paths can often result in higher energy detected by the receiver (RSSI), but the resulting signal can easily be distorted from the original waveform given the phase differences of those components, resulting in errors and drops of those packets. LQI, on the other hand, is a direct measure of the coherence of the received signal, hence serves a better indication of the resulting PER. The correspondence between the factory floor plan and these measurements (lower link qualities matching more cluttered areas) is encouraging, suggesting the potential of exploiting such correlation for systematic prediction of link qualities from given floor plans.

A.4   Channel Temporal Properties

Link (2, 2) from the NLOS-light area was chosen for the 24-hour temporal experiments. Two experimental tests are shown as Figure A.3 based on a 5-minute interval average (150 packets). Figure A.3(a) indicates that the link experienced little time variance and almost no drift. This observation is partially attributed to a well air-conditioned environment with no moving obstacles. In the second experiment as shown in Figure 7(b), a high packet loss rate was observed around noon despite the fact that no changes in average RSSI and downlink average LQI were

113

present during the same period. Other than the 3.5-minute PER spike, the link was stable as in the first experiment. Further measurements suggest that such errors may have been due to unidentified interference or noise.

| (a). Experiment 1 | (b). Experiment 2 |
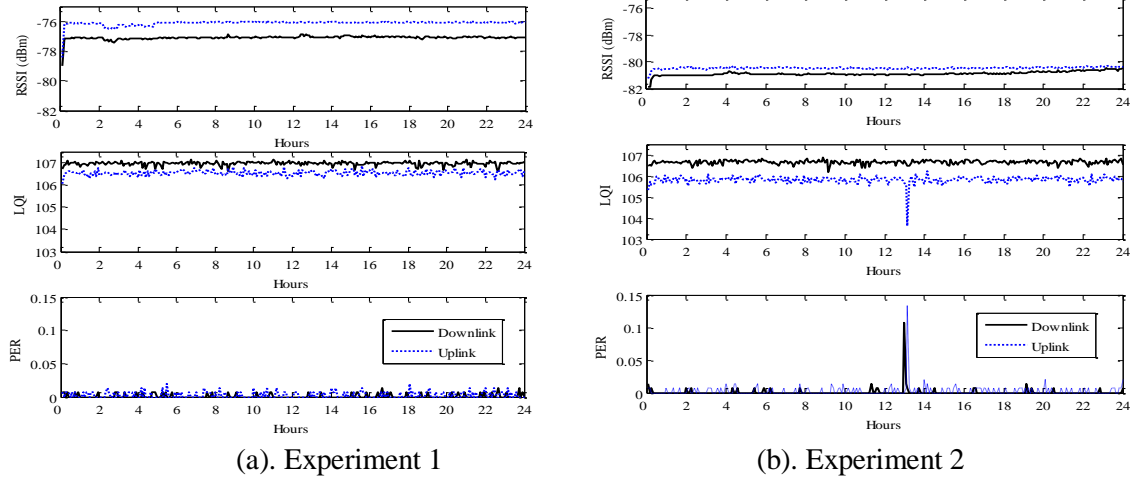
Figure A.3: Link metrics of uplink and downlink in the two temporal experiments

A.5   Link Symmetry

Link symmetry indicates the similarity of link quality in both directions. Specifically, if the link quality differs in uplink and downlink, it is classified as an asymmetric link. All the results presented thus far have shown observable differences between uplinks and downlinks. Nevertheless, within this limited machine shop range, the link qualities are considered "equally well" in both directions given that all PERs were almost below 0.01. This is consistent with the common conclusion of earlier studies that, for higher quality links, links are mostly symmetric.

To examine the degree of link asymmetry, a metric is defined as the absolute difference of downlink and uplink PER.

$$D_{asym} = | PER_{uplink} - PER_{downlink} | \qquad\qquad\qquad (A.1)$$

114

The cumulative distribution of D_{asym} for all links are presented in Figure A.4. Except for links (12, 1) and (3, 5), which had PER differences of 0.043, and 0.026, other differences were less than 0.01. Links (12, 1) and (3, 5) suffered the worst transmission quality among all links. This indicates that as the link quality degrades, its symmetry property deviates as well. The property differences between uplink and downlink may be attributed to sensor radio topology and possible hardware difference.
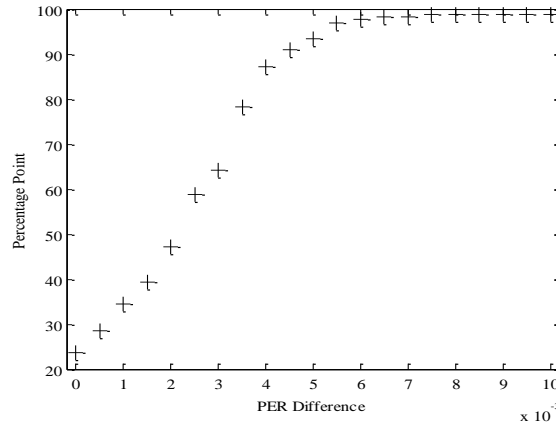
Figure A.4: CDF of PER difference in the spatial experiment

A.6   Metrics of Link Quality

The use of off-the-shelf sensor radios in the link quality assessment methods serves two purposes. Firstly, the assessment accurately portrays the link performance in actual operations. Secondly, the assessment can be done on-line to detect and adapt to temporal link variations. The goal here is to identify the feasibility of the three metrics RSSI, LQI, and PER for real-time link quality assessment. Note that PER has an apparent correspondence with the link performance perceived by a sensing application; hence, PER is considered as the objective metric to be predicted. To compare the effectiveness of RSSI and LQI as predictors for PER, their correlation with PER was analyzed based on measurements from the spatial experiment (165 uplinks and 165 downlinks). Figure A.5 shows PER vs. average RSSI and PER vs. average LQI, respectively. The

correlation coefficient for average RSSI and PER was 0.433, and that for average LQI and PER was 0.731, showing the stronger correlation between PER and average LQI.

(a) Average RSSI vs. PER   (b) Average LQI vs. PER
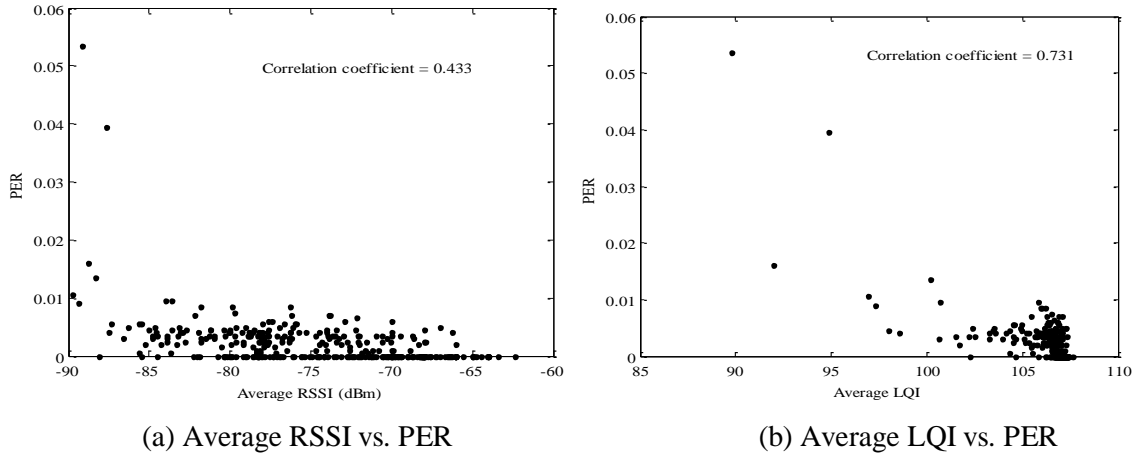
Figure A.5: Correlation between average RSSI, average LQI vs. PER

Despite its higher statistical correlation with PER than average RSSI, average LQI is not a perfect indication as it averages only the first 8 symbols of a received packet. Furthermore, when a radio link suffers from packet loss, average LQI could overestimate the transmission performance by not including LQI of the lost packets, which are expected to be low. As seen from Figure A.3(b), when the downlinks experienced high PERs, the average LQI did not show the same trend.

Bibliography

[Abhay2005] G. Abhay and M. R. Tennefoss, "Radio Frequency Control Networking: Why Poor Reliability Today Hampers What Could be a Viable Technology in the Future," Technology Assessment 005-0171-01B, Echelon Corporation, 2005.

[AbouRaddy1998] A.F. AbouRaddy, S.M. Elnoubi, and A. El-Shafei, "Wideband measurements and modeling of the indoor radio channel at 10 GHz Part II: time domain analysis," in *Proceedings of the 15th National Radio Science Conference (NRSC)*, pp. B14/1 – B14/8, 1998.

[ActiveSet] The MathWorks Inc., *Active Set Algorithm*, http://www.mathworks.com/access/ helpdesk/help/toolbox/optim/ug/brnoxzl.html#brnox01, accessed on 5/16/2010.

[Anritsu] Anristus, VNA Master™ Data Sheet, http://www.us.anritsu.com/downloads/files/ 11410-00501.pdf, accessed on 5/16/2010.

[ATI] Advanced Telemetrics International, *Non-Contact Torque Sensor Systems*, http://www.atitelemetry.com/viewproduct.php?id=6&appid=4, accessed on 02/10/2010.

[Atmel2008] Atmel Corporation, *AVR2014: AT86RF230 Receiver sensitivity measurements*, http://www.atmel.com/dyn/resources/prod_documents/doc8115.pdf, accessed on 5/31/2010.

[Baronti2007] P. Baronti, P. Pillai, V. W. C., Chook, S. Chessa, A. Gotta, and Y. F. Hu, "Wireless sensor networks: A survey on the state of the art and the 802.15.4 and ZigBee standards," *Computer Communications*, vol. 30, no. 7, pp. 1655-1695, 2007.

[Brooks2001] T. Brooks, "Wireless technology for industrial sensor and control networks," *Sensor for Industry Conference (SIcon)*, pp. 73-77, Rosemount, Illinois, Nov. 5-7, 2001.

[CC2420] Texas Instruments Incorporated, *CC2420 Data Sheet*, http://focus.ti.com/lit/ds/symlink /cc2420.pdf, accessed on 5/31/2010.

[Cerpa2003] Cerpa, A., Busek, N., and Estrin, D., September 2003, "SCALE: a Tool for Simple Connectivity Assessment in Lossy Environments," Center for Embedded Networked Sensing, UCLA, Tech. Rep. 0021, pp. 1–16, Sep. 2003.

[Chuang1987] J. Chuang, "The effects of time delay spread on portable radio communications channels with digital modulation," *IEEE Journal on Selected Areas in Communications*, vol. 5, no. 5, pp. 879 – 889, 1987.

[Ciadiello2005] T. Ciardiello, "Wireless communications for industrial control and monitoring," *Computing & Control Engineering Journal*, vol. 16, no. 2, pp. 12 – 13, 2005.

[Crossbow] Crossbow Technology, http://www.xbow.com/Home/wHomePage.aspx, accessed on 02/10/2010.

[DustNetworks] Dust Networks, Inc., http://www.dustnetworks.com, accessed on 02/10/2010.

[Dzapo2004] H. Dzapo, Z. Stare, and N. Bobanac, "Portable Wireless Measuring System for Monitoring Motor Shaft Parameters," *Instrumentation and Measurement Technology Conference*, Como, Italy, May 2004.

[EmbedSense] MicroStrain, EmbedSensor® wireless sensor, http://www.microstrain.com/embed-sense.aspx, accessed on 02/10/2010.

[Ember] Ember Corporation, http://www.ember.com/index.html, accessed on 02/10/2010.

[Eren2005] H. Eren, *Wireless Sensors and Instruments: Networks, Design, and Applications*, CRC Press, 2005.

[ETS-LINDGREN] ETS-Lindgren, *Microwave Absorber Selection Guide*, http://www.ets-lindgren.com/pdf/absorber.pdf, accessed on 5/29/2010.

[Goldsmith2005] A. Goldsmith, *Wireless Communications*, Cambridge University Press, 2005.

[Haber2005] R.E. Haber, J.R. Alique, S. Roa, and R.H. Haber, "Modeling and simulation of high-speed machining processes based on Matlab/Simulation," Lecture Notes in Computer Science, vol. 3516/2005, pp. 627 – 634, 2005.

[Hampicke1999] D. Hampicke, A. Richter, A. Schneider, G. Sommerkorn, R.S. Thoma, and U. Trautwein, "Characterization of the directional mobile radio channel in industrial scenarios, based on wide-band propagation measurements," in *Proceedings of IEEE 50th Vehicular Technology Conference*, vol. 4, pp. 2258 – 2262, 1999.

[Hashemi1993] H. Hashemi, "The indoor radio propagation channel," Proceedings of the IEEE, vol. 81, no. 7, pp. 943 – 968, 1993.

[Honeywell] Honeywell International Inc., *Wireless Torque, Rotary Torque and Reaction Torque Sensing at Honeywell Sensotec*, http://content.honeywell.com/sensing/sensotec/torque.asp, accessed on 02/10/2010.

[Hoppe1999] R. Hoppe, G. Wolfle, and F.M. Landstorfer, "Measurement of building penetration loss and propagation models for radio transmission into buildings," in *IEEE the 50th Vehicular Technology Conference*, vol. 4, pp. 2298 – 2302, 1999.

[HP8714] Agilent Technologies, *Agilent Technologies 8712ES and 8714 ES RF Network Analyzer User's Guide*, 1999.

[IEEE802.15.4] IEEE. *IEEE Standard 802 Part 15.4: Wireless Medium Access Control (MAC) and Physical Layer (PHY) Specifications for Low-Rate Wireless Personal Area Networks*, 2003.

[ISA] The International Society of Automation, ISA-100.11a-2009 Wireless Systems for Industrial Automation: Process Control and Related Applications, http://www.isa.org/ Template.cfm?Section=Standards2&template=/Ecommerce/ProductDisplay.cfm&ProductID =10766, accessed on 02/10/2010.

[Jabbar1989] M. A. Jabbar and M. A. Rahman, "Radio frequency interference of electric motors and controls," *Industry Applications Society Annual Meeting*, vol.1, pp.207-212, 1989.

[Kemp2005] A. H. Kemp and S. K. Barton, "The impact of delay spread on irreducible errors for wideband channels on industrial sites," Wireless Personal Communications, vol. 31, no. 3 – 4, pp. 235 – 248, 2004.

[Koulamas2001] C. Koulamas, A. Lekkas, G. Papandopoulos, G. Kalivas, and S. Koubias, "Delay performance of radio physical layer technologies as candidates for wireless extensions to industrial networks," in *Proceedings of the 8th IEEE International Conference on Emerging Technologies and Factory Automation (ETFA '01)*, vol. 1, pp. 133 – 142, 2001.

[Lal2003] Lal, D., Manjeshwar, A., Herrmann, F., Uysal-Biyikoglu, E., and Keshavarzian, A., 2003, "Measurement and Characterization of Link Quality Metrics in Energy Constrained wireless Sensor Networks," in *Proceedings of the IEEE Global Telecommunications Conference (Globecom'03)*, pp. 446–452, San Francisco, CA, Dec. 2003.

[Lessard1988] A. Lessard and M. Gerla, "Wireless communications in the automated factory environment," *IEEE Network*, vol. 2, no. 3, pp. 64 – 69, 1988.

[MICAz] Crossbow Technology, *MICAz Data Sheet*, http://www.xbow.com/Products/ Product_pdf_files/ Wireless_pdf/MICAz_Datasheet.pdf, accessed on 02/10/2010.

[MicroStrain] MicroStrain, Inc., http://www.microstrain.com/wireless-sensors.aspx, accessed on 02/10/2010.

[Miettien2002] J. Miettien, P. Salemenpera, V. Jarvinen, and M. Hervonen, "Wireless Operation Monitoring System for Polymer Covered Cylinders in Rolling Contact," *ASME Engineering Technology Conference on Energy, Petroleum Division*, vol. 2, pp. 1019-1023, 2002.

[MillenialNet] Millenial Net, http://www.millennial.net/industries, accessed on 02/10/2010.

[Neelakanta2003] P.S. Neelakanta and H. Dighe, "Robust factory wireless communications: a performance appraisal of the Bluetooth and the ZigBee^{TM} collocated on an industrial floor," *the 29th Annual Conference of the IEEE Industrial Electronics Society (IECON'03)*, vol. 3, pp. 2381 – 2386, 2003.

[Okumura1968] T. Okumura, E. Ohmori, and K. Fukuda, "Field strength and its variability in VHF and UHF land mobile service," *Review of the Electrical Communication Laboratory*, pp. 825 – 73, September/October 1968.

[Orhan2006] S. Orhan, N. Akturk, and V. Celik, "Vibration monitoring for defect diagnosis of rolling element bearings as a predictive maintenance tool: Comprehensive case studies," *NDT & E International*, vol. 39, no. 4, pp. 293 – 298, 2006.

[Ota2006] N. Ota and P. Wright, "Trends in wireless sensor networks for manufacturing," *International Journal of Manufacturing Research*, vol. 1, no. 1, pp. 3 – 17, 2006.

[Proakis2000] J.G. Proakis, *Digital Communications*, 4th edition, McGraw-Hill, 2000.

[Radiometrix] Radiometrix Ltd., *EMC-compliant Data Transmitter and Receiver Modules (TX2 & RX2)*, http://www.radiometrix.co.uk/products/txrx2p.htm, accessed on 02/10/2010.

[Rappaport1988] T. S. Rappaport, "Delay spread and time delay jitter for the UHF factory multipath channel," *IEEE 38th Vehicular Technology Conference*, pp. 186 – 189, Philadelphia, PA, 1988.

[Rappaport1989a] T. S. Rappaport, "Indoor radio communications for factories of the future," *IEEE Communications Magazine*, vol. 27, no. 5, pp. 15 – 24, 1989.

[Rappaport1989b] T. S. Rappaport, "UHF fading in factories," *IEEE Journal on Selected Areas in Communications*, vol. 7, no. 1, pp.40 – 48, 1989.

[Rappaport1989c] T. S. Rappaport, "Characterization of UHF multipath radio channels in factory buildings," *IEEE Transactions on Antennas and Propagation*, vol. 37, no. 8, pp. 1058–1069, 1989.

[Rappaport1991] T. S. Rappaport, S. Y. Seidel, and K. Takamizawa, "Statistical channel impulse response models for factory and open plan building radio communication system design," *IEEE Transaction on Communications*, vol. 39, no. 5, pp. 794 – 807, 1991.

[Rappaport1996] T. S. Rappaport, *Wireless Communication-Principles and Practice*, 2nd edition, Englewood Cliffs, NJ: Prentice-Hall, 1996.

[Reijers2004] N. Reijers, G. Halkes, and K. Langendoen, "Link layer measurements in sensor networks," in *Proceedings of the 1st IEEE International Conference on Mobile Ad-hoc and Sensor Systems*, pp. 224 – 234, Fort Lauderdale, FL, 2004.

[Sarkimaki2006] V. Sarkimaki, R. Tiaien, T. Lindh, and J. Ahola, "Applicability of ZigBee Technology to Electric Motor Rotor Measurements", *International Symposium on Power Electronics, Electrical Drives, Automation and Motion*, 2006.

[Seidel1991] S. Y. Seidel, T. S. Rappaport, S. Jain, M. L. Lord, and R. Singh, "Path loss, scattering, and multipath delay statistics in four European cities for digital cellular and microcellular radiotelephone," *IEEE Transactions on Vehicular Technology*, vol. 40, no. 4, pp. 721 - 730, 1991.

[Sklar1997] B. Sklar, "Rayleigh fading channels in mobile digital communication systems Part I: Characterization," *IEEE Communications Magazine*, vol. 35, no. 7, pp. 90 – 100, 1997.

[Sklar2001] B. Sklar, *Digital Communications: Fundamentals and Applications*, 2nd edition, Prentice Hall, 2001.

[Srinivasan2006] K. Srinivasan and P. Levis, "RSSI is under appreciated," in *Proceedings of the 3rd Workshop on Embedded Networked Sensors (EmNets)*, pp. 1 – 5, Cambridge, MA, 2006.

[Staub1997] O. Staub, J.-F. Zurcher, P. Morel, and A. Croisier, "Indoor propagation and electromagnetic pollution in an industrial plant," in *Proceedings of the IEEE International Conference on Industrial Electronics, Control and Instrumentation*, pp. 1198-1203, New Orleans, LA, 1997.

[Sundararjan2005] V. Sundararajan, A. Redfern, M. Schneider, and P. Wright, "Wireless sensor networks for machinery monitoring," in *Proceeding of ASME International Mechanical Engineering Congress and Exposition (IMECE)*, pp. 1 – 9, 2005.

[Tang2006] L. Tang, K. C. Wang, Y. Huang, and F. Gu, "Radio channel characteristics of ZigBee wireless sensors in machine shop for plant floor process monitoring," in *Proceedings of ASME International Manufacturing Science and Engineering Conference (MSEC)*, pp. 1–8, Ypsilanti, MI, Oct. 8–11, 2006.

[Tang2007] L. Tang, K. C. Wang, Y. Huang, and F. Gu, "Channel characterization and link quality assessment of IEEE 802.15.4-compliant radio for factory environment," *IEEE Transactions on Industrial Informatics*, vol. 3, no. 2, pp. 99 – 110, 2007.

[Tang2009] L. Tang, K. C. Wang, and Y. Huang, "Performance evaluation and reliable implementation of data transmission for wireless sensors on rotating mechanical structures," *Structural Health Monitoring*, vol. 9, pp. 113 – 124, 2009.

[Telado1998] A. F. Telado, "Estimating coverage of radio transmission into and within buildings at 900, 1800, and 2300 MHz," *IEEE Personal Communications*, vol. 5, no. 2, pp. 40 – 47, 1998.

[TelosB] Crossbow Technology, *TelosB Data Sheet*, http://www.xbow.com/Products/ Product_pdf_files/Wireless_pdf/TelosB_Datasheet.pdf, accessed on 4/19/2010.

[Tiwari2004] A. Tiwari, F.L. Lewis, and S.S. Ge, "Wireless sensor network for machine condition based maintenance," *Control, Automation, Robotics and Vision Conference*, vol. 1, pp. 461 – 467, 2004.

[VNABasics] Agilent Technologies, *Agilent Network Analyzer Basics*, 2004.

[VNADynamic] Agilent Technologies, *Agilent Understanding and Improving Network Analyzer Dynamic Range*, 2000.

[Walfisch1988] J. Walfisch and H. L. Bertoni, "A theoretical model of UHF propagation in urban environments," *IEEE Transactions on Antennas and Propagation*, vol. 36, no. 12, pp. 1788 - 1796, 1988.

[Wang2007] K.-C. Wang, L. Tang, and Y. Huang, "Wireless sensors on rotating structures: performance evaluation and radio link characterization," in *Proceedings of the WinTECH Workshop at ACM MobiCom*, pp. 3 – 10, 2007.

[Werb2005] J. Werb, M. Newman, V. Berry, S. Lamb, D. Sexton, and M. Lapinski, "Improved quality of service in IEEE 802.15.4 mesh networks," in *Proc. Int. Workshop Wireless and Industrial Automation*, pp. 1–6, San Francisco, CA, Mar. 2005.

[Willig2002] A. Willig, "Measurements of a wireless link in an industrial environment using an IEEE 802.11.-compliant physical layer," *IEEE Transactions on Industrial Electronics*, vol. 49, no. 6, pp. 1265 – 1282, 2002.

[Willig2005] A. Willig, K. Matheus, and A. Wolisz, "Wireless technology in industrial networks," *Proceedings of the IEEE*, vol. 93, no. 6, pp. 1130–1151, 2005.

[WINA] Wireless Industrial Networking, Alliance, http://www.wina.org/, accessed on 02/10/2010.

[WirelessHART] HART Communication Foundation, *Wireless HART Technology*, http://www.hartcomm.org/protocol/wihart/wireless_technology.html, accessed on 02/10/2010.

[Wright2008] P. Wright, D. Dornfeld, and N. Ota, "Condition monitoring in end-milling using wireless sensor networks (WSNs)," *Transactions of NAMRI/SME*, vol. 36, pp. 177 – 183, 2008.

[Yegani1989] P. Yegani and C.D. McGillem, "A statistical model for the line-of-site (LOS) factory radio channels," in *Proceedings of IEEE 39th Vehicular Technology Conference,* vol. 2, pp. 496 – 503, San Francisco, CA, 1989.

[Yegani1991] P. Yegani and C.D. McGillem, "A statistical model for the factory radio channel," *IEEE Transaction on Communications*, vol. 39, no. 10, pp. 1445 – 1454, 1991.

[Zhao2003] J. Zhao and R. Govindan, "Understanding packet delivery performance in dense wireless sensor networks," in *Proceedings of the 1ˢᵗ International Conference on Embedded Network Sensor Systems*, pp. 1 – 13, Los Angeles, CA, 2003.

[ZigBee] ZigBee Alliance, ZigBee Specification, http://www.zigbee.org/Default.aspx, 2005.